Schriftenreihe des
Instituts für Mikrowellentechnik

16

Hasan Iqbal

Synthetic Aperture Radar (SAR) Imaging and Polarimetric Clutter Analysis Using Automotive Radars

Institut für Mikrowellentechnik
Universität Ulm

Synthetic Aperture Radar (SAR) Imaging and Polarimetric Clutter Analysis Using Automotive Radars

Synthetic Aperture Radar (SAR) Imaging and Polarimetric Clutter Analysis Using Automotive Radars

DISSERTATION

zur Erlangung des akademischen Grades eines

DOKTOR-INGENIEURS
(Dr.-Ing.)

der Fakultät für Ingenieurwissenschaften,
Informatik und Psychologie der Universität Ulm

von

Hasan Iqbal

aus Karachi

Gutachter:	Prof. Dr.-Ing. Christian Waldschmidt
	Prof. Dr.-Ing. Hermann Schumacher
Amtierender Dekan:	Prof. Dr. phil. habil. Anke Huckauf

Ulm, 9 March 2023

Bibliografische Information der Deutschen Nationalbibliothek
Die Deutsche Nationalbibliothek verzeichnet diese Publikation in der Deutschen Nationalbibliografie; detaillierte bibliografische Daten sind im Internet über http://dnb.dnb.de abrufbar.

Dissertation, Universität Ulm,
Fakultät für Ingenieurwissenschaften, Informatik und Psychologie, 2023

Impressum
Universität Ulm
Institut für Mikrowellentechnik
Prof. Dr.-Ing. Christian Waldschmidt
Albert-Einstein-Allee 41
89081 Ulm
https://www.uni-ulm.de/mwt

Eine Übersicht über alle Bände der Schriftenreihe finden Sie unter
https://www.uni-ulm.de/mwtschriften

ISBN 978-3-948303-36-5 ISBN 978-3-948303-37-2 (E-Book)

Acknowledgements

The results detailed in this dissertation are the culmination of the work carried out during my employment with the Institute of Microwave Engineering at Ulm University. I would take this opportunity to thank Prof. Dr.-Ing. Christian Waldschmidt for providing me the opportunity at the institute as well as the handy advice and technical insights which he imparted onto me during our numerous technical discussions. My sincerest gratitude also to Prof. Dr.-Ing. Hermann Schumacher for accepting the role of the second examiner for my dissertation and therefore ensuring that my academic stint at Ulm University started with him in 2010 and also ended with him in 2023!

Accomplishing something of the magnitude of a PhD is unthinkable without the ever present help and support of colleagues. Here I would like to sincerely thank Dr.-Ing. Frank Bögelsack for always making time to answer my sometimes very basic questions as well as the numerous long technical discussions we were prone to having. I am also not able to count, how many complicated issues he helped me to solve during the course of the PhD.

I would also like to thank my former colleagues Christina Knill and Markus Schartel for their help in delivering the final presentations for my accepted conference papers, which I was unable to do as I had already left the university. Without their help, the results presented here would not have had the same weight.

The almost 5 years I spent at the Institute in Ulm were my first job experience in Germany, and I would like to thank all of my colleagues for welcoming me and showing me the ropes at the institute. There are a lot of mannerisms and etiquettes which I was able to learn from them and which are still very useful to this day.

My family always supported me in my seemingly unending journey to a PhD. I am very thankful and grateful for their support and understanding. A very special heartfelt appreciation also for my wife who had to sacrifice almost all Sundays and many many weekends and holidays, so that I could work on

writing papers and my dissertation!

It is always the case with scientific works that one builds upon the foundations laid down by one's peers near and far in the scientific community. Therefore, I would like to express my gratitude to everyone who has, is and will contribute to the body of scientific knowledge and make their new insights readily available to the young and curious minds.

Ulm, on 20th July 2023

Abstract

Recent years have been witness to large strides being made towards realising ever more advanced driver assistance systems which ultimately should overlap significantly with driving functions required for autonomous driving vehicles. These driving functions are based on the data and insights gleaned from usually a triad of sensing technologies: cameras, lidars and radars.

The objective of the work contained in this dissertation is to investigate and present algorithms which can be used to derive more information out of an automotive radar than is possible with current techniques. The synthetic aperture radar (SAR) has been used for reconnaissance and remote sensing for more than half a century and is now finding application in the automotive scenario. The motion of the ego-vehicle can be used to accumulate a large number of radar measurements of the surroundings perpendicular to the ego-trajectory. These measurements can then be integrated together to form a high-resolution radar map of the surroundings. This radar map can be used for parking the ego-vehicle or even be passed to the infrastructure over car-to-X.

The use of polarimetry capable radar sensors can enable a multitude of solutions which would make automated driving easier: self-localisation using polarimetric radar cross-section measurements (RCS), polarimetric SAR to win more information of ubiquitous traffic objects and clutter analysis to recognise driving surfaces and loss of traction in adverse weather conditions.

It is shown that with the help of polarimetry, typical traffic objects like light poles and guideposts can be discriminated based on their RCS. This can enable self-localisation by cross referencing a high definition map of the location.

Polarimetric SAR makes the task of orientation estimation of parked cars much easier. Cars have large curved surfaces which depolarise incident polarised waves while other regions of the car are not curved, and hence do not cause depolarisation. This information can be used for orientation estimation.

Polarimetric clutter analysis makes use of the polarisation dependent scattering and reflection of polarised incident waves from the road surface. The

presence of snow and water alters the physical characteristics of the road which may make it smoother and prone to loss of traction of the wheels. Such behaviour can be detected using a forward looking long range radar.

Contents

1 Introduction and Motivation

This chapter serves to deliver a brief overview of the recent developments with respect to the automotive environment perception as well as the direction in which the automotive sector is heading. This provides the rationale behind the research work presented in this dissertation.

Finally, a synopsis of the dissertation is given where each chapter is given a cursory portrayal. This should function as a blueprint of the dissertation, with the aid of which the reader can orientate oneself.

1.1 ADAS: State of the Industry and the Path Forward

In the previous decade the automotive industry has made gigantic investments towards achieving complete autonomous driving platforms. Numerous start-ups, like Uber and Lyft, as well as spin-offs of existing large technological companies for example Waymo, have deployed considerable resources towards achieving level 5 automation as defined by the automotive standards [1] [2]. These companies have reported over 5 million kilometres of autonomous driving on real world roads [3]. Most of them started testing in relatively warm and dry areas. Waymo has apparently fared well and has had success in conditions with reduced visibility during sandstorms [4] and has reportedly started testing in the colder regions to overcome the challenge of snowy and icy roads [5].

The one area of automotive industry which, however, will continue to develop is that of advanced driver assistance systems (ADAS) since they directly affect the safety of the cars which are currently being sold and will come onto the market in the coming years. This is ensured by the star ratings given by the “European New Car Assessment Programme” (Euro NCAP). Euro NCAP prescribes safety standards which all cars need to fulfil in order to receive a particular number of stars as a safety rating [6]. These standards are improved every year, thereby pushing car manufacturers to continuously improve their products. The improvement in ADAS systems will ultimately also help with advancing autonomous driving, since most of the safety systems and the technologies which enable them to perform, overlap with the requirements of autonomous driving systems.

Currently state-of-the-art ADAS systems are dependent on three sensors for environment perception,

1. Cameras
2. Lidar sensors
3. Radar sensors

The camera can arguably deliver information with the greatest density. This is due to the fact that light has a much smaller wavelength and hence higher resolution. The information is also easy to handle, since it is in a format which can easily be understood by humans. On the other hand, cameras are rendered almost blind in the dark, while adverse weather conditions severely limit the camera's functionality.

The lidar sensor is similar to a radar in the sense that it is also an active sensor, which means it transmits its own energy, thus lidar sensors function equally well in darkness. However since they operate at wavelengths close to visible light (905 nm and 1550 nm), the losses are high and the power which can be transmitted is limited in the 905 nm band, since it can penetrate the eye and reach the retina [7]. Lidar sensors are also easily impaired by weather conditions like fog, rain and snowfall, reducing their effective range to a few metres. Additionally, lidar sensors are at the moment prohibitively expensive, such that they are almost exclusively used by complete autonomous platforms and are mostly avoided in mass produced cars.

Out of these three, the radar sensor suffers the least deterioration in adverse weather conditions. Additionally, it is only with the radar sensor that one can acquire not just power levels corresponding to the size (radar cross-section) of the targets, rather one has phase[1] information available as well. This is one of the biggest advantages, a radar has over the other sensors. With phase information, it is possible to create radar images as well as evaluate Doppler frequencies, so that in case of a moving target, trajectory information of the target can be estimated as well.

Therefore, there is an ever increasing amount of interest in novel techniques

[1] Recently some progress has been made with FMCW lidar sensors, though they remain far from ready for deployment [8].

and processes, with the help of which it may be possible to glean more information about the 'world'. In this dissertation therefore, work is outlined where radar sensors are used to investigate how and what new information can be obtained and integrated into ADAS thereby making the car easier to operate and safer for all traffic participants.

1.1.1 Current Challenges for ADAS

Though the ADAS systems of today have made tremendous progress in the last decade, there are some areas where the industry is still on the hunt for possible solutions.

Self-Localisation

One of the problems currently being investigated by the car manufacturers and automotive suppliers is that of self-localisation, where a car being driven along a road attempts to recognise its surroundings independent of a GPS location fix, using only the radar backscatter information available [9]. To make this job easier, it would be helpful to be able to distinguish between the objects found on the sides of the roads like traffic signs, guide posts and street lights. This is possible by classification of objects based on their radar cross-section (RCS) measurements. It will be shown how traffic objects can be recognised based on their RCS later in this dissertation.

Automated and Assisted Parking

Many car manufacturers started offering automatic parking functions in their cars, where a car driving along a street searches for vacant spots and upon finding one, the driver is notified and the car then parks itself into the spot. So far this has been implemented using a combination of ultrasound and short range radar sensors (SRRs) mounted at the corners of the car. There is a very large room for improvement here since the ultrasound sensors can only deliver very poor information about possible targets and they are prone to interference from machines being used in construction zones like pneumatic drills for example. Even wind and rain can deteriorate their performance significantly more than that of radars. However, the SRRs mounted at the corners, though they can detect and resolve moving objects very accurately, they are not so adept at finding vacant spots between stationary parked cars. A possible solution to overcome this problem is the synthetic aperture radar signal processing technique which will be presented later in this dissertation.

Road Surface Recognition

One of the most critical problems which currently no car manufacturer or automotive supplier has been able to address is the issue of decreasing friction on roads under deteriorating weather conditions. For example, in snowy and icy conditions, the roads are considerably slippery and the car as well as the driver most often cannot gauge this until the car encounters such a patch. This is usually too late, and depending on the particular spot on the road, it is possible that the car cannot be controlled and sharp braking in such situations may actually make the situation worse. It is therefore of the utmost interest keeping safety of all traffic participants in mind, to detect such locations of impaired traction before the car actually reaches such a spot. This could be implemented using the long range radar (LRR) mounted in the front of the car which normally has a range of over 200 m [10]. A possible solution for this problem will also be presented later.

1.2 Outline of Dissertation

The research work presented in this dissertation aims to tackle the issues mentioned in Section 1.1.1. The problems are diverse and distributed in nature because of which it is necessary to highlight the objectives of this work:

- Investigation of radar cross-sections (RCS) of various objects found in typical traffic situations. It is also necessary to use a polarimetric sensor to investigate RCS patterns and attempt to find patterns and behaviours which can shed some light on how these objects interact with incident vertically and horizontally polarised waves. Any differences in observed behaviour could theoretically help in distinguishing different objects based on their radar signatures.
- A feasibility analysis of the suitability of synthetic aperture radar (SAR) for automotive applications. The hypothesis is that the forward motion of

a car while it searches for an empty parking space, can be made use of to accumulate hundreds of radar measurements and process them to achieve high resolution images of the scenery.

- Another avenue to be looked into, is use of polarimetric (SAR) to investigate whether the task of contour estimation and orientation of parked cars can be simplified with the use of extra information which is available because of the addition of a couple of polarisation channels.
- Use of radar polarimetry to investigate the clutter from road surfaces in varying weather conditions as well as surfaces other than asphalt. Goal is to recognise behavioural differences between the wave polarisations and to make use of these differences to come to conclusions regarding the driving surface. These can give important information regarding traction offered by the driving surface.

All the research work described here is held together by the points mentioned above and is organised into chapters as described in the following paragraphs.

Chapter 2, after this introduction, describes very briefly the radar fundamentals necessary for the accomplishment of the tasks described in this work.

Chapter 3 discusses the concepts and theorems of wave polarisation and radar polarimetry upon which some of the research carried out is based. Some of these concepts, like reflection from rough surfaces as well as the Pauli decomposition basis, are normally not touched in most radar courses and sometimes not even in textbooks.

Meanwhile *Chapter 4* introduces the synthetic aperture radar (SAR) measurement geometry for the automotive case as well as the significance of SAR. Following this, the SAR processing algorithms are briefly revised.

Chapter 5 presents the first task where the investigation of the radar cross-sections (RCS) of various traffic objects is considered. Here, initially it is discussed why a set of special antennae are needed before the novelty of their design is illustrated. Later, the fabricated antennae are shown along with their measured beam patterns. Afterwards the signal processing basis for the calculation of the RCS is discussed, before the measurement set-up is introduced and calibrated for RCS measurements. Finally the measured radar signatures of the various objects are shown and discussed in depth.

Chapter 6 takes a thorough look at the feasibility of automotive synthetic aperture radar (SAR). First, SAR in the context of automotive scenarios is defined, followed by the first measurement results obtained from a linear rail unit. It is also discussed what improvements need to be done in order to process images from a realistic platform not based on a rail unit. These improvements are shown to correct for accelerations which are inherent in any measurements carried out by a moving car. This is necessary since SAR algorithms are designed to work for platforms with a constant velocity, that is where the acceleration is zero. Next, a realistic SAR demonstrator designed for automotive SAR, is introduced. The signal processing chain is clarified with important aspects highlighted, for example the reconstruction of missing ramps in between blocks of chirps. Towards the end, the measurement results are shown and discussed. The combination of the SAR demonstrator and the ability to reconstruct missing ramps is significantly new in this realm. The results are high resolution radar images of the target scenery, which are much finer in resolution as compared to those obtained from classical radar signal processing.

Chapter 7 is dedicated to building on the work shown in Chapter 6 by considering polarimetric SAR, a novel concept for automotive applications. In the first few pages, the basics of polarimetric SAR in the context of automotive applications are clarified before an in-depth look is taken at the Pauli decomposition basis and whether such a decomposition is useful for automotive targets. Next, the measurement set-up is described and afterwards, the results are presented. In the discussions of the results it is indicated that a cross-polarised power ratio would make for a useful representation of the processed information. During the discussions, it is also argued what new information is available with use of polarimetric SAR and how it could be used.

In *Chapter 8* a detailed polarimetric clutter analysis is presented. This is an avenue which is still new as there have not been any results reported in literature which were acquired in realistic driving conditions on roads. After a brief clarification of clutter in the context of automotive radars and a quick discussion of why a clutter analysis is needed, the fully polarimetric radar sensor is shown and the parameters set for the measurements are discussed. Then a measurement campaign with a linear rail unit is described in the first phase after which the results are shown and discussed in detail. Later the need for realistic measurements with the help of a test vehicle is discussed. For such measurements the azimuth beam-width of the radar sensor needed to be focussed for which a lens was simulated, designed and fabricated. The resulting beam patterns are illustrated before the measurement set-up on the radar test vehicle is examined in great detail. The calibration steps as well as the measurement set-up are also described in fine detail. Finally, the measurement results for clutter from asphalt in inclement weather conditions as well as clutter from cobblestone roads are shown and analysed in depth.

2 Radar Fundamentals

The term radar is an acronym for "**RA**dio **D**etection **A**nd **R**anging" which implies where a radar is deployed and for what purpose [11]. As an instrument radars have been in use for more than 80 years in the military and space industries. As mentioned in Section 1.1, radars have in the recent years found many applications in the automotive sector. The first experiments consisting of attaching radars to cars were carried out in the early seventies [12] until the first adaptive cruise control was offered in the S-Class by Mercedes-Benz in 1998 until it became a common feature in premium cars about 8 years later. Fast forward to the present and the use of radars for automotive applications has innumerable possibilities.

However, before applications are discussed, it is important to take a look at the fundamentals of radars briefly in this chapter. Only the equations and concepts pertinent to the work carried out in the frame of this dissertation are presented in this chapter, however for basics, it is recommended to read the sources mentioned.

2.1 Radar Equation

One of the most useful expressions concerning a radar is the radar equation shown below [13],

$$P_{\mathrm{Rx}} = \frac{P_{\mathrm{Tx}} G_{\mathrm{Rx}} G_{\mathrm{Tx}} \lambda^2 \sigma}{(4\pi)^3 \, r^4}, \tag{2.1}$$

where P_{Tx} is the transmitted power, G_{Tx} the transmitting antenna gain, G_{Rx} the receiving antenna gain, σ the radar cross-section (RCS) of the target reflecting the transmitted waves, r the range to the target and P_{Rx} is the received power. Sometimes the same antenna is used for the transmission and reception of the electromagnetic waves, thus in this case G_{Tx} and G_{Rx} are the same.

For the automotive case however, the antennae are normally different though co-located and hence, (2.1) holds true.

This equation describes the way the power of a transmitted wave from a radar spreads out in a sphere. A portion of this power is then reflected back towards the radar by a target and the amount of reflected power is dependent on the RCS of the target. This reflected power will be spread out spherically on the way to the radar as well. In a nutshell, this describes the spread of the power as well as how much of it is reflected from a target.

This equation and the terms involved in it will play an important role in the discussion and analysis of the research activities described in the later chapters of this dissertation.

2.2 Frequency Modulated Continuous Wave (FMCW) Radar

The radar used predominantly for automotive applications is the frequency modulated continuous wave (FMCW) radar. FMCW radars won out over pulse radars, which are the standard radars used in aerospace applications, due to the cost of the electronics needed in pulse radars to generate high pulse peak powers, among other factors.

FMCW radars make use of a voltage controlled oscillator (VCO) to generate a frequency which is linearly proportional to the voltage applied at its input. This signal is frequency modulated by varying the input voltage over time. The most common frequency modulation used is linear, where the frequency changes linearly with time. Mathematically this is represented as [14]

$$s_{\mathrm{tx}}(t) = \exp\left[\mathrm{j}(2\pi(f_0 + c_r t)t)\right], \tag{2.2}$$

with f_0 denoting the start frequency of the signal, c_r the radar chirp rate and t the time. The change of frequency with time is referred to as a chirp or a ramp [15]. Both these terms are interchangeable. The ramp repetition interval (T_r) is used to refer to the duration of the chirp, and $c_\mathrm{r}T_\mathrm{r}$ gives the bandwidth of the signal. This is depicted visually in Fig. 2.1.

This signal is transmitted by the radar and a delayed version of the same signal is then received by the radar, after it has been reflected back by a target

$$s_{\mathrm{rx}}(t) = \exp\left[\mathrm{j}(2\pi(f_0 + c_r t)(t - \tau)\right], \tag{2.3}$$

where τ represents the time delay for the signal to reach the target and travel back to the radar. This is given as $\tau = \frac{2r}{c}$ where c is the speed of light. The signal in (2.3) is then converted to a lower frequency by applying it to the input of a mixer along with a copy of the signal in (2.2). Once the output has been passed through a low pass filter, the resulting intermediate frequency (if) signal can be expressed as

$$s_{\mathrm{if}}(t) = \exp\left[\mathrm{j}(2\pi(f_0 + c_r t)\tau\right]. \tag{2.4}$$

The signal in (2.4) has a frequency which is directly dependent on the distance to the target

$$f_{\mathrm{b}} = \frac{\mathrm{d}}{\mathrm{d}t}(c_{\mathrm{r}} t\tau) = c_{\mathrm{r}}\frac{2r}{c} \tag{2.5}$$

and is referred to as the beat frequency.

2.3 Resolution

The resolution is an important criterion of any radar. It is the capability of the radar to distinguish between objects that are in close proximity to each other [16]. If the spacing between the objects is less than the resolution, they will not be resolved and therefore will appear as one large object (target) by the radar and thus be placed in the same range or azimuth bin.

Range or azimuth bin is a term used to refer to the ‘space’ where all objects are treated as one single target since the radar cannot discriminate between them.

2.3.1 Range Resolution

The range resolution describes the minimum distance in range where two objects can be resolved. This is directly dependent on the smallest difference in the beat frequencies (Δf) that can be detected which in turn is given by the observation time or the chirp repetition time (T_{r}) as [17]

$$\Delta f > \frac{1}{T_{\mathrm{r}}}. \tag{2.6}$$

Since f_b is known from (2.5), an alternative expression for Δf can be found as

$$\Delta f = c_\mathrm{r} \frac{2\Delta r}{c}, \tag{2.7}$$

with Δr representing the range resolution at the boundary case where $\Delta f = \frac{1}{T_\mathrm{r}}$. By combining (2.6) and (2.7), one can find the range resolution for an FMCW radar as

$$\Delta r = \frac{c}{2 f_\mathrm{BW}}, \tag{2.8}$$

where f_BW is the bandwidth of the transmitted chirp. The range resolution of an FMCW radar is therefore inversely proportional to the bandwidth of the transmitted chirp.

By considering (2.8) one may be led to believe that an ever increasing bandwidth of the transmitted signal will lead to a finer resolution in every case. This is true in theory, however practically this raises a few issues which in the end negatively impact the achievable resolution. One of the issues is that the antennae as well as the radar electronics (in particular the transmission lines or waveguides as the case may be) are optimised for a certain band of frequencies. It is not possible to achieve this optimal performance over a broad frequency region. A common guideline used for design of high resolution radar systems is to keep the relative wavelength of the transmitted signal in mind. For example a bandwidth of 4 GHz between 1 GHz and 5 GHz has a wavelength difference of approximately 0.24 m while the same bandwidth between 77 GHz and 81 GHz has a wavelength difference of 0.192 mm. Therefore it is easier to maintain uniform system characteristics for 77 GHz band than for the lower frequency one [18].

As discussed, it is easier to design a high resolution radar at higher rather than lower frequencies. However there is one blockade which prevents arbitrarily large bandwidths. The IF signal in (2.4) needs to be sampled by an analogue to digital converter (ADC) and the higher the beat frequency (resulting from large bandwidth), the more sophisticated the ADC needs to be.

Additionally, systems operating at THz frequencies have to contend with dispersion effects, where the refractive index of air varies considerably more than in the microwave region [19, 20]. This increases the complexity of the system and hence also the cost. Therefore in the end a trade-off needs to be made such that the requirements of the task at hand are fulfilled.

2.3.2 Azimuth Resolution

The azimuth angle is defined as the angle measured from true north to the bore-sight of the radar antenna main-beam [21]. This angle describes the lateral position of any target. The azimuth direction by extension refers to the direction along this plane. In literature it is sometimes also referred to as the cross-range direction. Similar to the range resolution, the azimuth resolution is defined as the ability of a radar to distinguish between two objects that are separated in azimuth by a distance equal to the azimuth resolution. It is defined as [22],

$$\Delta R_{\mathrm{azi}} = \frac{R\lambda}{D}, \tag{2.9}$$

where D is the diameter or the largest dimension of the antenna, R is the range at which the objects are located and λ is the wavelength. This implies that any objects which are located within the antenna beam-width will be identified as one object. Hence to achieve a fine azimuth resolution, the antenna needs to be physically large which may not always be a feasible solution.

Additionally the azimuth resolution can be improved in digital beam-forming radars as well as synthetic aperture radar (SAR). SAR will be introduced in detail later.

2.3.3 Velocity Resolution

When the radar platform is mobile, the FMCW radar can be used to detect moving objects with the help of Doppler shift of the frequency of the waves transmitted and received by the radar. Through the Doppler shift it is possible to determine the relative radial velocity of the objects. For the sequence of chirps as shown in Fig. 2.1, the velocity resolution can be defined as [23],

$$\Delta v = \frac{c}{2 f_0 T_{\mathrm{r}} N_{\mathrm{rmp}}}, \tag{2.10}$$

where f_0 is the start frequency, T_r is the ramp repetition interval and N_rmp is the number of ramps in a sequence.

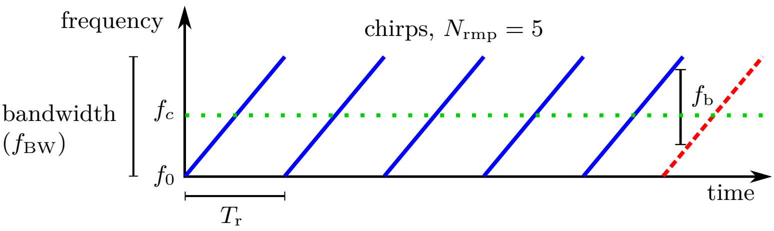

Fig. 2.1: Chirp parameters for an FMCW radar. The blue (solid) ramps represent transmitted signals while the red (dashed) ramp denotes the received signal. f_b denotes the beat frequency which signifies the frequency of the beat-signal, that is the down-converted intermediate frequency (IF) signal where f_b is dependent on the range to target.

Thus it is evident that the overall measurement time, $T_\mathrm{r} \cdot N_\mathrm{rmp}$, is crucial to obtaining a fine velocity resolution. This is however in contrast to the maximum velocity that can be unambiguously detected. The maximum Doppler frequency is given as [23],

$$f_{\mathrm{D,max}} < \frac{1}{2T_\mathrm{r}}. \tag{2.11}$$

Knowing the Doppler frequency,

$$f_\mathrm{D} = \frac{2vf_0}{c} \tag{2.12}$$

by combining (2.11) and (2.12), one can find the maximum velocity that can be unambiguously resolved [23],

$$v_\mathrm{max} = \frac{c}{4f_0T_\mathrm{r}}. \tag{2.13}$$

Thus for a given set of chirp parameters, the maximum velocity can be calculated that can be successfully resolved without ambiguities by the radar. This is an important theoretical result which will lay the foundation for measurements done for the polarimetric clutter analysis, in the scope of this dissertation.

2.4 Radar Cross-Section (RCS)

Radar cross-section (RCS) refers to the signature of a target object measured with a radar from all viewing angles [24]. It is a measure of the amount of incident energy that is reflected by the target. It can be imagined as the fictional area which captures an amount of power, such that when it is radiated isotropically, produces the same amount of received power at the radar [25].

The definition of RCS in terms of mathematical relations can be understood by considering [25]

$$\sigma = \lim_{R\to\infty} 4\pi R^2 \frac{|E_\mathrm{s}|^2}{|E_\mathrm{i}|^2}, \tag{2.14}$$

where R is the range from the radar to the target, E_i is the incident electric field strength at the target, E_s is the scattered field strength at the radar and σ denotes the RCS of the target. This essentially denotes that the RCS is independent of increasing range, given that the range to the target is sufficiently large so that the electromagnetic waves transmitted by the radar seem to be flat or in other words a plane wave when incident on the target. The RCS is an inherent part of the radar equation in (2.1).

To illustrate the factors which dictate the size of an RCS, (2.15) below shows the expression for calculating the radar cross section of a flat plate [26],

$$\sigma_\mathrm{plate} = \frac{4\pi b^2 l^2}{\lambda^2}, \tag{2.15}$$

where b and l are the breadth and length of the plate while λ is the wavelength. (2.15) shows that the RCS is basically dependent on the size of the plate relative to the wavelength of operation of the radar. To explain this point better, consider the RCS of a flat square plate with each side being 3.31 cm long. The RCS at 77 GHz is then 1 m^2 while the RCS of the same plate at 24 GHz is 0.0967 m^2.

The expression for the RCS in (2.14) can also be expressed as [27]

$$\sigma = 4\pi R^2 \frac{S_s}{S_i}, \tag{2.16}$$

where the RCS is defined as the ratio of the scattered power density (S_s) [W/m^2] and the incident power density (S_i) [W/m^2] at a range of R from the radar sensor. It is essentially the same as (2.14) but relates directly to the power measured by the radar.

2.5 Concluding Remarks

Over the previous pages a quick introduction of the basic radar fundamentals was given, as these are necessary for the tasks presented later in this work. It is not in the scope to handle the material here in greater detail, therefore it is recommended to consult the literature cited here, in case more details are required.

3 Wave Polarisation and Polarimetry

Even though the term ‘wave polarisation’ is relatively new in science, the effects of polarisation have been exploited by humans as far back as 1000 AD when the Vikings used crystals, perhaps calcite, to navigate the northern Atlantic ocean in conditions which were often cloudy or foggy [28]. Without a compass, the Vikings used these crystals, often described as ‘sunstones’ in Norse sagas, to expose unique patterns of light in the sky which arise due to polarisation and exist even when the sky is overcast or foggy.

The polarisation properties of electromagnetic waves only received mainstream acceptance (although not without ample controversy) after the presentation of the unifying theory of electricity, magnetism and light (indeed all electromagnetic waves) by James Clerk Maxwell in 1861. He showed that electromagnetic waves have an orientation of the electric field vector, which can be affected when the wave interacts with an interface. Thus the waves carry information about the reflecting object. It is this information which is of interest in radar polarimetry.

The basics needed for the research carried out in this dissertation are briefly explained here. However, to gain a thorough understanding of the concepts it is strongly recommended that the reader peruse the cited books and journals. Additionally, the content of this chapter has been written keeping the objective of clutter investigation using a polarimetric automotive radar in mind. Hence some of the content, irrelevant to this research objective, was skipped even though they may be a staple of most radar polarimetry textbooks.

3.1 Polarimetric Backscattering Descriptor

Polarimetry starts with the basic concept of describing a scatterer which reflects polarised waves back towards the radar. This is done by the 2×2 complex scattering matrix which illustrates how the transmitted electric field ($\boldsymbol{E}^t$) which is incident on a target, is transformed by the said target into the reflected or scattered electric field ($\boldsymbol{E}^r$) as follows [29],

$$\boldsymbol{E}^r = \frac{\mathrm{e}^{-\mathrm{j}\gamma r}}{r}\mathbf{S} \cdot \boldsymbol{E}^t,$$
$$\boldsymbol{E}^r = \frac{\mathrm{e}^{-\mathrm{j}\gamma r}}{r}\begin{pmatrix} S_{\mathrm{HH}} & S_{\mathrm{HV}} \\ S_{\mathrm{VH}} & S_{\mathrm{VV}} \end{pmatrix} \cdot \boldsymbol{E}^t. \tag{3.1}$$

The four parameters of $\mathbf{S}$ are descriptors of the complex scattering process, $S_{\mathrm{ii}} = |S_{\mathrm{ii}}|\,\mathrm{e}^{\mathrm{j}\varphi_{\mathrm{ii}}}$. The subscripts, either horizontal (H) or vertical (V), represent the polarisation of the transmitted or reflected wave. $\gamma = \alpha + \mathrm{j}\beta$ is the propagation constant and together the term $\frac{\mathrm{e}^{-\mathrm{j}\gamma r}}{r}$ denotes the phase shift and attenuation for a wave that is incident on a target after having traversed a distance r. In all subsequent discussions, when the polarimetric scattering parameters are discussed, the same convention is adopted as shown here.

3.2 Scattering of Waves from a Surface

Since one of the objectives of the research work was to investigate the effects of clutter from the ground, the reflection of waves from a surface is the phenomenon which is most relevant in the scope of this dissertation. The scattering from a surface depends on different factors to varying degrees. It can broadly be divided into two cases which depend on the surface roughness and the wavelength of the waves. Since for an application the wavelength of operation is assumed to be constant, the cases can be neatly divided into scattering from smooth and rough surfaces which are discussed on the following pages.

3.2.1 Scattering from Smooth Surfaces

When the radar beam touches the ground, a part of the incident power is reflected back (this is referred to as backscatter [30]), while another part of it penetrates the ground and is absorbed and a third portion of the power is reflected in the forward direction, that is away from the radar. Depending on the application in question, the power reflected back towards the radar contributes power to clutter, raising the noise floor and deteriorating the dynamic range of the system. [31].

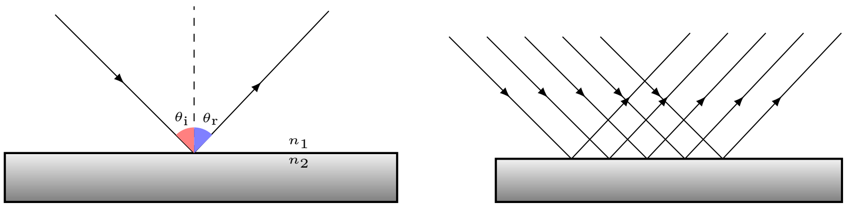

(a) Angle of incidence and reflection.

(b) Reflection at a smooth boundary, orderly coherent scattering.

Fig. 3.1: When a wave interfaces with a smooth surface.

To investigate how clutter behaves, it is important to understand how the incident wave is reflected from a surface. Figure 3.1a shows a single wave incident on an interface where the refractive index of the lower medium is greater than that of the medium above (that is $n_1 < n_2$). For the purpose of the discussion here, it is assumed the medium with the smaller refractive index, n_1, is air ($n_1 = 1$) and that the reflecting surface is smooth and plane. The incoming waves are, therefore, scattered coherently in an ordered manner as illustrated in Fig. 3.1b. Each ray is reflected such that the phase change because of the reflection is the same, no matter at what point the wave interacts with the surface. This results in all of the reflected waves interfering constructively in one direction, such that the angle of incidence equals the angle of reflection ($\theta_\mathrm{r} = \theta_\mathrm{i}$). This is known as *specular* reflection and the direction of reflection is called the *specular* direction [32]. The portion of the power that penetrates into the surface material is of no consequence for the investigation of clutter, thus, it is not considered in the discussion here.

The proportion of the incident wave energy which is reflected from the surface can be described by the reflection coefficient R which describes a relationship between the incident electric field ($\boldsymbol{E}^i$) and the reflected electric field ($\boldsymbol{E}^r$), such that $\boldsymbol{E}^r = R\boldsymbol{E}^i$. Additionally when the incident wave is not incident to the surface at right angles ($\theta_\mathrm{i} = 0°$), the orientation of the electric field vector with respect to the surface plays a significant role in determining how much power is reflected from the surface. That is the polarisation of the wave determines the reflection coefficients, so that two expressions are needed to describe the phenomenon as [32],

$$\rho_{\mathrm{VV}} = \frac{\varepsilon_{r_2} \cos\theta_{\mathrm{i}} - \sqrt{\varepsilon_{r_2} - \sin^2\theta_{\mathrm{i}}}}{\varepsilon_{r_2} \cos\theta_{\mathrm{i}} + \sqrt{\varepsilon_{r_2} - \sin^2\theta_{\mathrm{i}}}}, \tag{3.2}$$

$$\rho_{\mathrm{HH}} = \frac{\cos\theta_{\mathrm{i}} - \sqrt{\varepsilon_{r_2} - \sin^2\theta_{\mathrm{i}}}}{\cos\theta_{\mathrm{i}} + \sqrt{\varepsilon_{r_2} - \sin^2\theta_{\mathrm{i}}}}. \tag{3.3}$$

ε_{r_2} is the relative permittivity of the material comprising the lower medium with refractive index n_2 and $\varepsilon_{r_2} = \sqrt{n_2}$. θ_{i} is the angle of incidence as illustrated in Fig. 3.1a. These equations are known as the Fresnel reflection coefficients. Since ε_{r_2} is a complex number, both ρ_{VV} and ρ_{HH} are complex as well, though their magnitudes lie between the extremes of 0, signifying no reflection, and 1 which denotes complete reflection. When the wave is incident perpendicularly ($\theta_{\mathrm{i}} = 0°$), it can be seen from (3.2) and (3.3) that both ρ_{VV} and ρ_{HH} become identical. This makes sense as in this case, there is no vertical direction, since both planes are aligned with the surface.

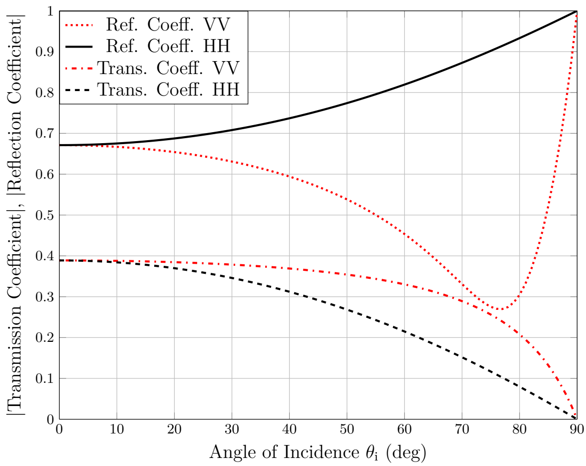

Fig. 3.2: Reflection coefficients of horizontally and vertically polarised waves from water ($\varepsilon_{r_2} = 8.24 - \mathrm{j}16.21$) at 77 GHz and 20 °C.

The curves corresponding to the magnitude of the reflection coefficients described in (3.2) and (3.3) are shown in Fig. 3.2. They have been plotted for a wave at 77 GHz interacting with water at 20 °C. The dielectric constant of water has been calculated from a model, the details of which can be found in Appendix A. The complex valued dielectric constant of water, leads to complex valued Fresnel coefficients calculated from (3.2) and (3.3). However here only the magnitude of the Fresnel coefficients are considered as the angle of the coefficients describes the phase of the reflected and transmitted waves and does not influence the power that is reflected from a surface or is absorbed [33].

The transmission coefficients represent the power that is not reflected from the surface, rather penetrates into the surface and is absorbed by the material. The transmission coefficients have been calculated as, $\tau_{\mathrm{VV}} = 1 - |\rho_{\mathrm{VV}}|$, where τ_{VV} represents the transmission coefficient for the vertical polarisation. The plotted reflection coefficients display contrasting behaviours between the vertical and horizontally polarised signals. The reflection coefficient for the horizontal polarisation simply increases monotonically with the incidence angle reaching a maximum reflectivity of 1.0 at the grazing angle. The vertical reflectivity however decreases with increasing angle of incidence initially, where it reaches a minimum at around 78° angle of incidence. This is known as the pseudo-Brewster angle [32].

The Brewster angle is defined as the angle at which the vertically polarised component of an incident non-polarised wave (usually light in literature but applies to all electromagnetic radiation) has zero reflectivity. That is, the vertically polarised component is completely transmitted into the medium. This was the case for a lossless medium, when the medium is lossy on the other hand, the reflectivity of the vertically polarised component does not reach zero, rather a non-zero minimum as illustrated in Fig. 3.2 [30]. This was first reported by Sir David Brewster in 1815, thereby lending his name to the angle [34].

At this angle the reflected signal will be dominated by horizontally polarised waves as the horizontal reflectivity reaches a value (> 0.9) close to the peak and the difference between the reflection coefficients for the two polarisations is maximum. The reflectivity for the vertical polarisation then also reaches the peak reflectivity at grazing angles.

3.2.2 Scattering from Rough Surfaces

Having gained a handle on the behaviour of electromagnetic waves when interacting with a smooth surface, it is important now to consider the situation in case of a rough surface. Though it is first necessary to discuss what kind of surface can be classified as rough. Keeping the application in mind, road surface clutter investigation, the boundary is considered to be horizontal. Thus, the roughness can be characterised by considering the root mean square (rms) of the deviation of the surface locally from the average surface level. This deviation can be expressed as a height deviation, h from the mean height h_{avg} [32].

If these deviations are in the order of the wavelength of operation, then the scattered waves no longer combine coherently as shown in Fig. 3.1b. Therefore, one cannot expect to have specular reflection as was the case in Section 3.2.1. Rather scattering from a rough surface can be characterised to be 'chaotic' without a preference for either direction of reflection or polarisation [32]. This is illustrated in Fig. 3.3.

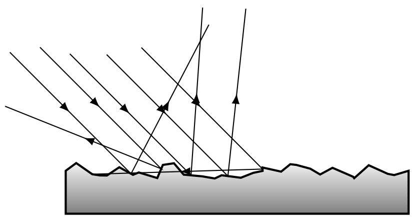

Fig. 3.3: Scattering from a rough surface.

To understand why scattering from a rough surface behaves as shown in Fig. 3.3, it is necessary to consider the phase difference ($\Delta\phi$) between rays which are reflected from various levels of a surface which vary in height. When the difference in height approaches the size of the wavelength, the reflected waves interfere in a less predictable manner thereby leading to incoherent scattering. According to the criteria defined by Rayleigh, a surface can be considered smooth if the phase difference satisfies the condition, $\Delta\phi < \frac{\lambda}{4}$. This leads to the condition for the height difference where a surface is considered rough as [32],

$$h_{\text{rough}} > \frac{\lambda}{8\cos\theta_{\text{i}}}, \tag{3.4}$$

where θ_{i} is the angle of incidence and λ is the wavelength of the incident wave. However, when the wavelength of operation is in the same order of magnitude as the height of the facets, a stricter criterion is needed to define the smoothness of a surface. To this end, the phase difference between the scattered rays is lowered to $\Delta\phi < \frac{\lambda}{8}$, resulting in the following condition [32],

$$h_{\text{rough}} > \frac{\lambda}{32\cos\theta_{\text{i}}}, \tag{3.5}$$

which is referred to as the *Fraunhofer* criterion. If the height of the facets as shown in Fig. 3.4 is higher than (3.5), then the surface is considered to be rough.

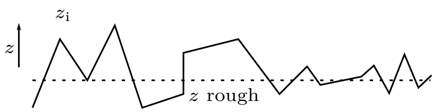

Fig. 3.4: Bragg rough surface definition.

One of the models used for scattering from rough surfaces is the small perturbation model (SPM) [35], also known as the Bragg surface scattering model, which is suitable for applications where the size of the perturbations are not greater than the wavelength. Such a surface is shown in Fig. 3.4. The dotted line indicates a smooth surface without any perturbations while the solid line illustrates the actual surface which has significant deviations from the dotted surface. To ascertain the suitability of the SPM, the root mean square (rms) roughness of the surface is necessary and defined as [30],

$$s = \sqrt{\frac{\sum\limits_{i=1}^{N}(z_i - z)^{-2}}{N-1}}, \tag{3.6}$$

where the surface has been modelled with an N-point discretisation while z

represents the level of the smooth surface and z_i the level (or height) of the facets present on the rough surface as illustrated in Fig. 3.4.

Applications of SPM typically comprise situations where the roughness of the surface in comparison to the wavelength can satisfy the rule of thumb, $\beta s < 0.3$, where $\beta = \frac{2\pi}{\lambda}$ is the phase constant [30]. A suitable application for this model is remote sensing of natural surfaces using the L (1 to 2 GHz) and P (250 to 500 MHz) bands.

This condition cannot be fulfilled however at 77 GHz, where a wavelength of approximately 4 mm is smaller than or of the same size as the surface (for the application here: road surface) perturbations. Therefore the SPM was not pursued further, rather a different criteria was used for the investigation of clutter.

3.3 Depolarisation Due to Scattering from a Rough Surface

It has been shown in literature that when waves are incident on a sloped surface, the reflected waves will have a significant portion of the waves that are cross-polarised with respect to the incident polarisation [30].

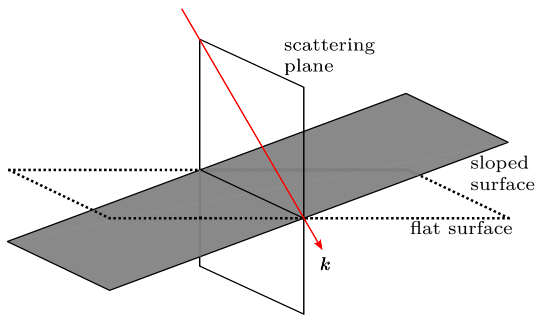

Fig. 3.5: Schematic of a surface with slope. $\boldsymbol{k}$ indicates the propagation direction of the incident wave.

Fig. 3.5 illustrates the concept of reflection from a surface with slope. Here the sloped surface models a single facet of the rough surface which could be composed of many such formations having random orientations with respect to the angles and directions. The multiple reflections from these facets lead to significant depolarisation of the incoming wave hence there is a much lower coherent scattering component available, depending of course on the extent of the surface roughness [30].

In order to develop a metric for gauging the roughness of a surface, an important relation can be found with circularly polarised waves which can be adapted to linear polarised waves. It has been shown that the circular *left left-right right* (or the *right right-left left*, as both are identical) correlation coefficient, defined as [36]

$$\varphi_{\mathrm{RRLL}} = \frac{\left\langle S_{\mathrm{RR}} \cdot S_{\mathrm{LL}}^{*} \right\rangle}{\sqrt{\left\langle |S_{\mathrm{RR}}|^{2} \right\rangle \left\langle |S_{\mathrm{LL}}|^{2} \right\rangle}} \tag{3.7}$$

where S_{RR} is the scattering parameter corresponding to the right circular polarised transmitted and received wave while S_{LL} similarly for the left circular polarised wave, is sensitive to the roughness of a surface. $\langle\ \rangle$ denotes an average taken over the period of observation.

In case of a linearly polarised measurement system, the circular correlation coefficient (φ_{RRLL}) can be written in terms of the linear polarisations using the relations [36],

$$S_{\mathrm{RR}} = \frac{1}{2}(S_{\mathrm{HH}} - S_{\mathrm{VV}} + 2jS_{\mathrm{HV}}), \tag{3.8}$$

$$S_{\mathrm{LL}} = \frac{1}{2}(S_{\mathrm{HH}} - S_{\mathrm{VV}} - 2jS_{\mathrm{HV}}), \tag{3.9}$$

as [30]

$$R = \frac{\left\langle |S_{\mathrm{HH}} - S_{\mathrm{VV}}|^{2} \right\rangle - 4\left\langle |S_{\mathrm{HV}}|^{2} \right\rangle}{\left\langle |S_{\mathrm{HH}} - S_{\mathrm{VV}}|^{2} \right\rangle + 4\left\langle |S_{\mathrm{HV}}|^{2} \right\rangle} \qquad 0 \leq R \leq 1, \tag{3.10}$$

R is a ratio which varies between 0 corresponding to a very rough surface such that the cross-polarised component is as strong as the two co-polarised components and 1 signifying a very smooth surface such that there is negligible depolarisation. R is dependent on the characteristics of the surface from which the wave is reflected and is independent of the variations in the dielectric constant of the surface [30]. Therefore, R is a suitable parameter with which to analyse the driving surface and its roughness.

A second parameter M defined as,

$$M = \frac{\left\langle \left|S_{\mathrm{HH}} - S_{\mathrm{VV}}\right|^2 \right\rangle + 4\left\langle \left|S_{\mathrm{HV}}\right|^2 \right\rangle}{\left\langle \left|S_{\mathrm{HH}} + S_{\mathrm{VV}}\right|^2 \right\rangle} = \tan^2\alpha_{\mathrm{b}}, \tag{3.11}$$

can be further used to study the dielectric constant of the reflecting surface as it is not affected by variations in roughness [37]. It is also related to the angle α_{b} of the Bragg model which is used for extracting material properties of the reflecting material [30]. It is a parameter based on empirical evidence where M was used to discriminate between wet and dry soil for remote sensing applications [37]. M is directly proportional to the angle of incidence, thereby advantageous for the application at hand since for the automotive clutter study, the angles of incidence are rather high (above approximately 80°). Therefore, this parameter can be used to help with the estimation whether the road surface is covered by a material whose dielectric constant is different to that of asphalt, like snow or water for example [30, 37].

3.4 Pauli Decomposition Basis

In polarimetry the scattering matrix $\mathbf{S}$ is often decomposed into the *Pauli* basis, where each matrix denotes an elementary scattering process. $\mathbf{S}$ is decomposed as [38],

$$\begin{aligned} S &= \begin{pmatrix} S_{\mathrm{HH}} & S_{\mathrm{HV}} \\ S_{\mathrm{VH}} & S_{\mathrm{VV}} \end{pmatrix} \\ &= a\begin{pmatrix} 1 & 0 \\ 0 & 1 \end{pmatrix} + b\begin{pmatrix} 1 & 0 \\ 0 & -1 \end{pmatrix} + c\begin{pmatrix} 0 & 1 \\ 1 & 0 \end{pmatrix} + d\begin{pmatrix} 0 & -\mathrm{j} \\ \mathrm{j} & 0 \end{pmatrix}, && (3.12) \\ &= a\,[S]_a + b\,[S]_b + c\,[S]_c + d\,[S]_d && (3.13) \end{aligned}$$

according to the Pauli basis defined in literature [30]. a, b, c and d are all complex valued and defined as,

$$a = \frac{S_{\mathrm{HH}} + S_{\mathrm{VV}}}{\sqrt{2}}, \quad b = \frac{S_{\mathrm{HH}} - S_{\mathrm{VV}}}{\sqrt{2}},$$

$$c = \frac{S_{\mathrm{HV}} + S_{\mathrm{VH}}}{\sqrt{2}}, \quad d = \mathrm{j}\frac{S_{\mathrm{HV}} - S_{\mathrm{VH}}}{\sqrt{2}}. \tag{3.14}$$

The matrix $[S]_a$ corresponds to the scattering matrix of a sphere or a plate. Generally it is described as representing the scattering behaviour from a single or odd number of bounces. $|a|^2$ represents the amount of power that is reflected from such a scattering behaviour. $[S]_b$ is indicative of scattering from a dihedral corner oriented at $0°$ and it is used to denote a scattering caused by a double or even number of bounces. $|b|^2$ gives the power thus reflected with such a scattering mechanism [38–40].

The third matrix, $[S]_c$, shows the scattering resultant from a dihedral corner oriented at $45°$ which causes the reflected wave to be orthogonally polarised when compared to the incident wave. Similarly to the previous two mechanisms, $|c|^2$ is the representation of the power reflected from just such a scattering process. Such scattering is prevalent in remote sensing for example in the form of volume scattering from forest canopies while in the automotive case, it will be seen in Chapter 7 that various regions of a car can rotate the polarisation of the incident waves [39, 40].

Finally the fourth matrix, $[S]_d$ represents the antisymmetric components of a scattering which occur when the transmitting and receiving antenna are not co-located. Normally in the automotive case, even though the transmitting and receiving antennae are separate, they are nonetheless co-located and hence any antisymmetric properties can be neglected. It is shown here merely for the sake of completeness [38].

3.5 Concluding Remarks

In this chapter, the concepts in polarimetry were briefly presented which are necessary in order to follow the work that has been presented in this dissertation. Where necessary, a distinction was also made between aerospace and automotive applications. Even though much of the concepts stay the same, the application of those concepts vary vastly.

4 Synthetic Aperture Radar (SAR) Fundamentals

In 1951, Carl A. Wiley of the then Goodyear Aircraft Corporation (now Lockheed Martin) proposed a novel method of improving the azimuth resolution of imaging radars. Wiley's work showed that a finer azimuth resolution was obtainable by processing multiple radar returns collected by a radar that is moving perpendicular to the area of interest that has to be imaged. He showed that the azimuth resolution that could be gained this way was much finer than the resolution which could be obtained from a real large radar antenna aperture. This concept was later named *Synthetic Aperture Radar* (SAR), however Wiley himself referred to it as *Doppler Radar Beam Sharpening* [41].

SAR found use in widespread applications in both military as well as civilian applications where an aircraft or satellite radar system is used to acquire radar measurements of the Earth's surface for example reconnaissance purposes for military applications or for observing changes in the mountain glaciers or polar ice for civilian remote sensing applications. In the research presented here, SAR has been adapted for applications in the automotive sector in particular for assisted or automated parking. In order to achieve this, it is necessary to first understand the application areas of both aerospace and automotive applications and in particular their differences.

4.1 Measurement Geometry

A comparison of the measurement geometries between the traditional airborne SAR and that for automotive scenarios is shown in Fig. 4.1 [42]. Airborne SAR has a geometry as shown in Fig. 4.1a, where the trajectory of the sensor platform is much higher than the target scenery (Earth surface). The antenna depicted with the aperture dimension L denotes the radar platform which follows the flight path indicated in the illustration. The radar platform can be an aircraft or a satellite as the case may be. The *range direction*, as depicted, is perpendicular to the flight path and tilted down towards the Earth surface, while the *azimuth direction* lies along the direction of the flight path. The beam-width of the antenna, denoted by $\Delta\Psi$, is also the angular resolution of the radar were the SAR technique not utilised. That is all targets within the beam would not be distinguishable from each other if the SAR processing were not carried out on the recorded measurements.

The measurement geometry for the automotive case is illustrated in Fig. 4.1b. The major difference to airborne SAR is that the radar platform is much closer to the target scenery while also having a direct perspective as compared to the airborne case where the radar platform looks down onto the target.

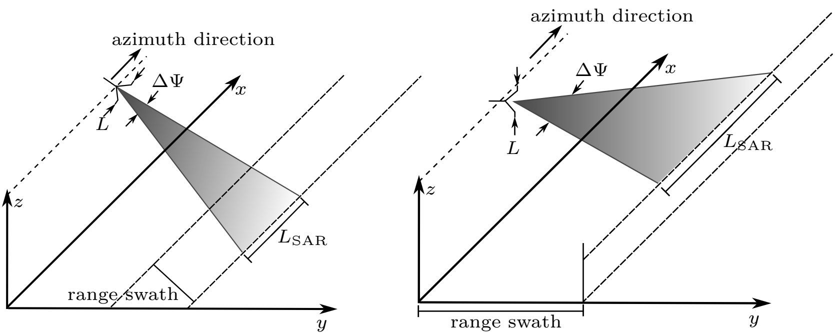

(a) Measurement geometry of airborne SAR.

(b) Measurement geometry of automotive SAR

Fig. 4.1: Comparison of traditional aerospace SAR and the adapted version for automotive applications [42].

The extent of the beam footprint in the azimuth direction, denoted by L_{SAR}, is the length of the virtual (or synthetic) aperture the radar must traverse in order to acquire a single pixel (in the azimuth direction, a line in the range direction) on the ground with the theoretical best resolution possible. To resolve a point in the azimuth direction, it has to lie in the beam footprint beginning from one edge to the opposite. This way the radar acquires a complete perspective of the target from either side [22, 43].

The geometry shown in Fig. 4.1 is that of **stripmap** SAR where the beam simply moves along the azimuth direction and everything in its path is imaged. This is in contrast to the other modes, like the scan mode SAR in reference to the moving beam which scans multiple swaths in range while in the spotlight mode the beam is consistently focussed on a single region of interest as the radar is traversed parallel to the target scenery [22]. Both scan mode and spotlight SAR are ill suited for automotive applications, hence they are not dealt with here. After this point, whenever SAR is mentioned, it is used to refer to stripmap SAR since this is the SAR imaging mode which is suitable for automotive applications.

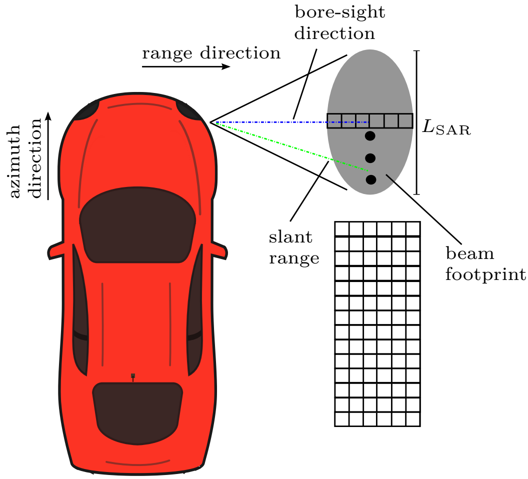

Fig. 4.2: Schematic illustrating the measurement geometry of automotive SAR.

Figure. 4.2[1] clarifies the measurement setup for the automotive SAR case. The *azimuth direction* lies similar to the aerospace case along the track or the driving direction. The square grid denotes the individual pixels which make up a SAR image, with each square in the azimuth direction representing an azimuth bin while in the range direction, the range bin. Also shown in Fig. 4.2 are the two lines representing the bore-sight direction and the slant range, where

[1]Image of car adapted from [44], licensed under CC0 1.0 Universal (CC0 1.0), Public Domain Dedication, https://creativecommons.org/publicdomain/zero/1.0/.

the bore-sight represents the point of closest approach for a target in the beam footprint. The slant range denotes the distance to a point which lies off the bore-sight of the radar but within the beam-width (field of view) of the radar antenna. The slant range is thus larger than the range to target at the point of closest approach which results from the azimuth-range coupling inherent in SAR measurement geometry. This leads to a phenomenon known as range cell migration which will be discussed later in Section 4.3.

These range variations of the target as the sensor moves, create a Doppler effect which can be utilised to achieve a finer resolution using a process often referred to as Doppler beam sharpening. This change in the Doppler frequency as the sensor moves along the track and hence a target point move across the beam is known as a Doppler bandwidth [45].

4.2 Azimuth Resolution

The achievable azimuth resolution is dependent on the length of the virtual (synthetic) aperture denoted by L_{SAR} in Fig. 4.2 and Fig. 4.1. This represents not only the extent of the beam footprint in the azimuth direction but also the distance the radar platform needs to move in order to resolve a single point in azimuth with the finest resolution possible.

The virtual aperture length for SAR can be calculated from the beam spreading in proportion with the range as,

$$L_{\mathrm{SAR}} = \frac{\lambda}{L} R, \tag{4.1}$$

where L is the largest physical dimension of the radar antenna which is being used for SAR measurements as shown in Fig. 4.1b [24]. The azimuth resolution for a SAR system can thus be calculated as

$$\delta_{\mathrm{SAR}} = \frac{\lambda}{2L_{\mathrm{SAR}}} \cdot R = \frac{\lambda R}{2} \cdot \frac{L}{R\lambda} = \frac{L}{2}, \tag{4.2}$$

to arrive at the expression for the theoretically best resolution attainable using SAR [24]. The expression above suggests that a physically smaller antenna results in finer resolution. This seems counter-intuitive in the beginning, especially when considering classical real array radars. Upon reflection however, it becomes clear that a smaller antenna will have a much broader beam-width and therefore all points in the target scenery are ‘seen’ by the radar for a longer duration than if the antenna was larger and hence had a narrower beam-width.

The theoretical resolution given in (4.2) is rarely ever realisable in practice however due to numerous reasons which act together to deteriorate resolution. Some of these reasons are discussed here. Consider Fig. 4.2 and imagine there is a target in the direction of travel along azimuth in the distance and not yet in the beam footprint. This target has a relatively constant (positive or negative dependent on convention) Doppler and as it comes closer, the Doppler component becomes non-linear shortly before becoming linear. Then once the target reaches the point of closest return, the Doppler crosses zero before changing signs (positive or negative) and increasing linearly. The same pattern is then repeated as the target becomes distant. In the derivation of (4.2), it was assumed that the Doppler frequency always changes linearly with time. This is however not entirely true, as the frequency change at the beginning and towards the end of the beam footprint is quadratic with respect to time, while in the middle it is linear. When the thus recorded signal is converted into the frequency domain, the energy is spread over multiple frequencies, thus reducing the resolution [46].

Another potential reason for poor resolution in the SAR image can be a coarser range resolution, resulting from a lower frequency bandwidth signal being transmitted. If the range resolution is much coarser than the azimuth resolution, the azimuth resolution will suffer since the targets have been recorded using low bandwidth. Hence, the energy from two close targets could be placed in the same range bin and hence even with SAR processing, these targets would not be resolvable.

The nature of the target scenery can also present challenges for the attainable resolution as random distributed scatterers produce noise in the SAR image which is referred to as speckle. One example of such a target is an asphalt road surface. The road is composed of stones which vary randomly in size and orientation, which thus scatter the incident energy in a ‘chaotic’ manner as shown in Fig. 3.3. The returns from multiple such targets lying in one resolution cell are summed together and in the processed SAR image, they are present as noise [47].

Finally, errors in the position of the radar platform or even sensor motion can introduce phase errors which increase blurring and deteriorate resolution.

Therefore it is of the utmost importance for SAR systems to have a reliable and accurate trajectory information [48].

4.3 Range Cell Migration

The slant range (described in Section 4.1) changes instantaneously as the car moves along the track. The slant range of a single point target when plotted against the trajectory (azimuth direction) traces a hyperbola with the lowest point coinciding with the point where the target was aligned with the bore-sight direction of the radar and hence had zero Doppler frequency component [45]. The range cell migration inherent in SAR systems needs to be distinguished from traditional radar processing, where range cell migration refers to the phenomenon of a target moving into a different range bin during one radar measurement.

This effect can be better understood by considering Fig. 4.3 which illustrates the slant range to a point target located at 2 m in azimuth and 0.5 m in range. As the radar moves along the track from 0 m azimuth towards the target, the slant range starts from a maximum of 2.06 m and gradually decreases until the target is oriented along the bore-sight direction of the radar. After this point, the slant range steadily increases until it reaches a maximum of 2.06 m again at the radar position of 4 m in azimuth.

This implies that when the trajectory of the target is profiled over the azimuth track, it moves (or migrates) through range cells over the entire duration of exposure of the target. Thus the name of the phenomenon, **range cell migration**. The range cell migration can be described mathematically with the help of a power series expansion as [45],

$$R(t_{\mathrm{azi}}) = R(t_{\mathrm{azi,c}}) - v \sin\theta_{\mathrm{sr,c}}(t_{\mathrm{azi}} - t_{\mathrm{azi,c}}) + \frac{1}{2}\frac{v^2 \cos^2\theta_{\mathrm{sr,c}}}{R(t_{\mathrm{azi,c}})}(t_{\mathrm{azi}} - t_{\mathrm{azi,c}})^2, \quad (4.3)$$

where $R(t_{\mathrm{azi}})$ is the slant range expressed as a function of azimuth time, $t_{\mathrm{azi,c}}$ is the azimuth time at the beam centre point (along bore-sight as shown in Fig. 4.2), $\theta_{\mathrm{sr,c}}$ is the angle between the beam centre and the slant range vector and v is the radar velocity.

The first term on the left hand side is the range to the scene centre along the bore-sight direction. The second term is the linear component and the

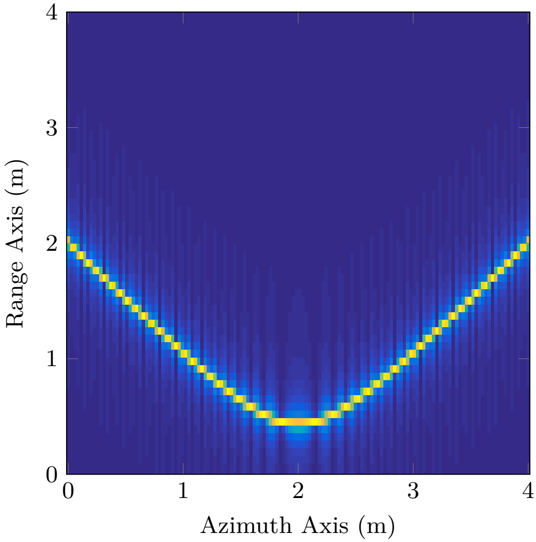

Fig. 4.3: Illustrating range cell migration for a single point target situated at 2 m in azimuth and 0.5 m in range.

third term is the quadratic component of range cell migration. The higher order terms are smaller and are normally ignored. One can also calculate the total range cell migration as well as the contributions from the linear and quadratic components in order to decide whether the quadratic term needs to be corrected or if it can be neglected. Usually for shorter wavelengths the quadratic component is too small to play a significant role [45].

4.4 Processing of Data into SAR Images

Once the measurements have been completed, the data can be expressed in the form of

$$s_{\mathrm{if}}(t_{\mathrm{azi}}, \omega(t)) = A_{\mathrm{if}} e^{-j2\frac{\omega(t)}{c_0}\sqrt{(x_{\mathrm{azi}}-x_{\mathrm{t}})^2+y_{\mathrm{t}}^2)}}, \tag{4.4}$$

with t_{azi} representing the azimuth time (in literature also known as slow-time, it is the time as the radar platform travels along the azimuth trajectory), $f(t)$ the instantaneous frequency of the transmitted signal, x_{azi} the azimuth position of the radar and $(x_{\mathrm{t}}, y_{\mathrm{t}})$ are the target coordinates. The range to the target can be calculated as

$$R(t_{\mathrm{azi}}) = \sqrt{(x_{\mathrm{azi}} - x_{\mathrm{t}})^2 + y_{\mathrm{t}}^2}). \tag{4.5}$$

The signal expressed in (4.4) forms the starting point for the SAR processing chain. Now that the data is ready, it can be processed into images of the target scenery. In order to accomplish this, three different processing algorithms were evaluated during the course of this work. These are briefly discussed on the next pages.

4.4.1 Line-by-Line Processing

This algorithm is the most basic in terms of understanding the underlying principles of SAR. The processing is done in the (azimuth) time domain, that is there is no Fourier transform carried out along the azimuth direction. Hence, the processing is done serially in the azimuth direction which leads to large computational efforts.

The finer details about the line processing algorithm can be found in [22]. Here the essence of the processing algorithm is considered. To this end consider the geometry shown in Fig. 4.4. This shows the distances from a distant point target, T, to the centre (P_0) of the synthetic aperture and to each of the other locations (P_{n}) where a measurement was carried out.

The additional distance which the transmitted and reflected wave must travel each way is denoted by $\Delta\mathrm{R}_{\mathrm{n}}$. And it is this additional distance which causes a phase error that needs to be corrected for each received signal. This phase error can be calculated for each received signal as

$$\Delta R_{\mathrm{n}} \approx \frac{d_{\mathrm{n}}^2}{2R}, \tag{4.6}$$

while assuming that $\Delta\mathrm{R}_{\mathrm{n}} \ll 2\mathrm{R}$ [22]. Once each received signal has been phase corrected, they are all then coherent and can be summed together to form a single range profile, that is one pixel in the azimuth direction and a complete

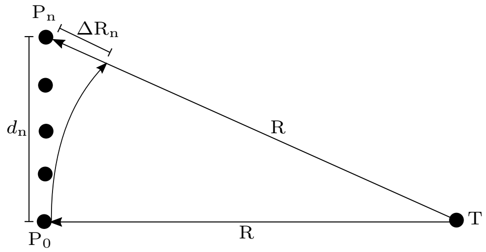

Fig. 4.4: Schematic illustrating the measurement geometry of automotive SAR.

profile in the range direction. Since each azimuth pixel, or line, is processed individually, this algorithm is thus named the line processing algorithm.

Repeating this complete process for all the measurements acquired over the trajectory will result in a complete SAR image of the target scenery. Though this algorithm is well suited as an entry point into SAR imaging, it is ill suited for practical systems because of the gigantic computation load. The next two algorithms though make use of the Doppler frequency where it is possible to process the measurements in parallel, thus offering significant time efficiency advantages.

4.4.2 Range Doppler Algorithm (RDA)

The necessary steps needed to process the acquired measurements into a SAR image, using the RDA, are shown in Fig. 4.5. The first step is a Fourier transform in the range direction, which is sometimes also referred to as "range compression". The raw data is then in the range domain.

The demodulated raw signal after the fast Fourier transform (FFT) in range direction has been carried out, can be written in the form [45],

$$s_{\mathrm{rc}}(r, t_{\mathrm{azi}}) = A_0 w_{\mathrm{r}}(t - \frac{2R(t_{\mathrm{azi}})}{c_0}) w_{\mathrm{a}}(t_{\mathrm{azi}}) \mathrm{e}^{-\mathrm{j}4\pi f_0 \frac{R(t_{\mathrm{azi}})}{c_0}}, \tag{4.7}$$

where r represents the range, A_0 is an arbitrary amplitude, w_{r} the range envelope which is usually a rectangle and is the duration of time between the transmission and reception of the reflected signal, w_{a} the azimuth envelope

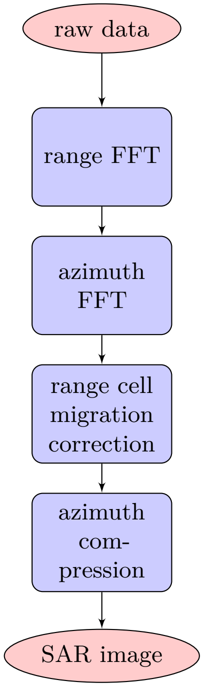

Fig. 4.5: Processing steps for the range Doppler algorithm (RDA) [49].

of the reflected signal that is dependent on the antenna beam pattern, R the range to the target and c_0 is the speed of light in air.

The signal after the azimuth Fourier transform can be expressed as,

$$S_{\mathrm{rd}}(r, f_{\mathrm{azi}}) = A_0 w_{\mathrm{r}}(t - \frac{2R(f_{\mathrm{azi}})}{c_0}) W_{\mathrm{a}}(f_{\mathrm{azi}}) \mathrm{e}^{-\mathrm{j}4\pi f_0 \frac{R(f_{\mathrm{azi}})}{c_0}}, \tag{4.8}$$

where $R(f_{\mathrm{azi}})$ is the range to the target expressed as a function of the azimuth frequency (Doppler). The azimuth frequency is described as,

$$f_{\mathrm{azi}} = K_{\mathrm{a}} t_{\mathrm{azi}}, \tag{4.9}$$

where K_a is the azimuth frequency linear modulation rate (it describes how fast the frequency changes in Hz/s) and is defined as,

$$K_\mathrm{a} = \frac{2v^2}{\lambda R_0}, \tag{4.10}$$

with R_0 being the range of closest approach, that is the range to the scenery at the point with zero Doppler. $R(f_\mathrm{azi})$ is then defined as [45],

$$R(f_\mathrm{azi}) = R_0 + \frac{\lambda^2 R_0 f_\mathrm{azi}^2}{8v^2}. \tag{4.11}$$

It is important to note that the range envelope function in (4.8), which represents the signal in the range-Doppler domain, is dependent on the azimuth frequency (f_azi). This is a result of the range cell migration which will be corrected in the next step. The range cell migration (RCM) in the range-Doppler domain can be expressed as,

$$\begin{aligned} R_\mathrm{rd}(f_\mathrm{azi}) &= \frac{R_0}{\sqrt{1 - \frac{c_0^2 f_\mathrm{azi}^2}{4v^2 f_\mathrm{c}^2}}} \\ &= \frac{R_0}{D(f_\mathrm{azi}, v)}, \end{aligned} \tag{4.12}$$

with f_c being the centre frequency of the transmitted signal (as illustrated in Fig. 2.1) and $D(f_\mathrm{azi}, v)$ representing the range migration factor in the range Doppler domain. The range migration factor is a measure of how much the targets wander through the range cells as the radar traverses along the trajectory and is dependent on the difference between the range (R) to the target and R_0. The range cell migration can then be corrected by carrying out an interpolation from the azimuth coupled range to the range which has been compensated using the migration factor as represented in (4.12) [45]. The signal after the range cell migration correction then becomes,

$$S_\mathrm{rcmc}(r, f_\mathrm{azi}) = A_0 w_\mathrm{r}(t - \frac{2R_0}{c_0}) W_\mathrm{a}(f_\mathrm{azi}) \mathrm{e}^{-\mathrm{j}\frac{4\pi R_0}{\lambda D}}, \tag{4.13}$$

where it can be seen that the range envelope is now independent of azimuth frequency, thus the range cell migration has been corrected. The energy also is now focussed in the range direction at $r = R_0$, the point of closest approach.

Though the energy in the range direction has been focussed, there is still a need to compress the signal in the azimuth direction so that a focussed image can be acquired. The azimuth focussing can be done with the help of an azimuth matched filter designed to be used in the range-Doppler domain, defined as [45]

$$H_{\mathrm{azi}}(f_{\mathrm{azi}}) = \mathrm{e}^{\mathrm{j}\frac{4\pi R_0 D f_0}{c_0}}. \tag{4.14}$$

After the matched filtering, an inverse Fourier transform is done in the azimuth domain, to acquire the processed SAR image data,

$$s_{\mathrm{ac}}(r, t_{\mathrm{azi}}) = A_0 w_{\mathrm{r}}(t - \frac{2R_0}{c_0}) w(t_{\mathrm{azi}}) \mathrm{e}^{-\mathrm{j}\frac{4\pi R_0}{\lambda}}. \tag{4.15}$$

4.4.3 Range Migration Algorithm (RMA)

The final processing algorithm to be discussed within the scope of this work, is the range migration algorithm which was initially used in seismic applications [50]. The range Doppler algorithm discussed previously has some shortcomings, for example it is assumed that the energy reflected from a target are plane waves when they arrive at the radar sensor. This assumption may hold true when the range to the target is large and the frequency of operation low, however for near-range applications it would lead to phase errors which will deteriorate the resolution in the processed SAR image. This is where the RMA works well, as here it is not assumed that the waves are plane, rather the curvature of the waves is corrected and the range-azimuth coupling is removed with the Stolt interpolation [48].

The steps necessary for the processing of the data are mentioned in Fig. 4.6. Each of the steps are also described briefly below.

The first step towards processing the measurements using RMA is to take the Fourier transform in the azimuth domain. This step transforms the measurement data (raw data or beat-signal) which is in the $(x_{\mathrm{azi}}, k_{\mathrm{r}})$ domain, where x_{azi} represents the azimuth (time domain) trajectory of the radar and k_{r} is the wavenumber, to the $(k_{\mathrm{x}}, k_{\mathrm{r}})$ domain so that k_{x} denotes the azimuth spatial frequency which varies linearly between $\frac{-\pi}{\delta x}$ and $\frac{\pi}{\delta x}$ [48]. The term δx here denotes the distance between two consecutive measurements, that is the spacing between two synthetic (or virtual) array elements.

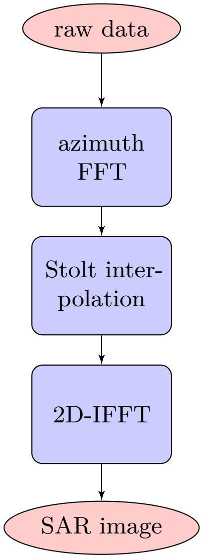

Fig. 4.6: Processing steps for the range migration algorithm (RMA) [48].

The signal can then be expressed as,

$$S_{\mathrm{if}}(k_{\mathrm{x}}, k_{\mathrm{r}}) = A_{\mathrm{if}} w_{\mathrm{r}}(k_{\mathrm{r}}) W_{\mathrm{a}}(k_{\mathrm{x}}, k_{\mathrm{r}}) \mathrm{e}^{-j(k_{\mathrm{x}} x_{\mathrm{t}} - y_{\mathrm{t}} \sqrt{k_{\mathrm{r}}^2 - k_{\mathrm{x}}^2})}, \tag{4.16}$$

with A_{if} denoting the amplitude of the signal and x_{t} and y_{t} are the coordinates of a target point in the respective Cartesian axes. k_{r} denotes the range spatial frequency, that is the RF frequency scaled by $\frac{4\pi}{c_0}$ and is therefore defined as $k_{\mathrm{r}} = \frac{2 \cdot \omega(t)}{c_0}$. w_{r} and $W_{\mathrm{a}}(k_{\mathrm{x}}, k_{\mathrm{r}})$ are the range and azimuth envelopes respectively, analogous to those introduced in (4.8) but adapted for RMA in terms of k_{r} and k_{x} [48].

Now that the data is in the $(k_{\mathrm{x}}, k_{\mathrm{r}})$ domain, the next step is to remove the range-azimuth coupling as evidenced by the azimuth envelope in (4.16). This effect can be better understood with the help of Fig. 4.7 which visually shows the energy spread for a simulated point target in the Range-k_{x} domain. At this stage the signal energy traces a curve over the azimuth direction, owing to

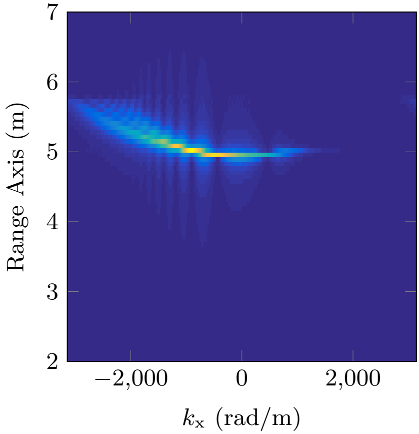

Fig. 4.7: Range-azimuth coupling in the (k_x, k_r) domain before Stolt interpolation [51].

the wavefront curvature of the received energy. If this range-azimuth coupling is not corrected and azimuth compression (inverse Fourier transform in the azimuth direction) is carried out, the energy would not be focussed to a point as it is spread over several range cells.

On close inspection of (4.16), it is possible to see that the phase of the signal is dependent on the term $y_t\sqrt{k_r^2 - k_x^2}$ where the y-axis coordinate of the target is dependent on the slant range vector (range spatial frequency, k_r) as well as the azimuth spatial frequency k_x. To correctly focus the energy on the target points, this coupling between the range and azimuth has to be removed. This is done using the *Stolt interpolation*. The Stolt interpolation is a k_x dependent non-linear interpolation which decouples the azimuth and range dimensions by mapping data from k_r to a new dimension k_y which aligns with the range direction. This mapping is given by [14],

$$k_y = \sqrt{k_r - k_x}. \tag{4.17}$$

The physical orientation of the dimensions of k_r, k_x and k_y is shown in Fig. 4.8. k_r is the slant range vector, which is how the wave travelling from

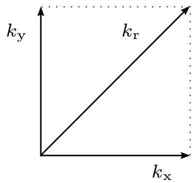

Fig. 4.8: Schematic explaining the physical orientation of the dimensions from (4.17).

the target back to the radar propagates. k_x and k_y are the azimuth and range vectors respectively, which need to be decoupled in order to acquire a focussed SAR image.

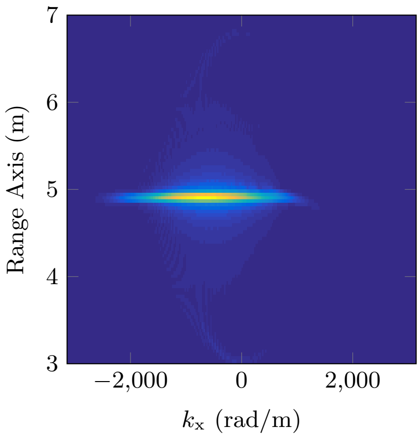

Fig. 4.9: Range-azimuth coupling in the (k_x, k_r) domain after Stolt interpolation [51].

Once the Stolt interpolation has been carried out, the reflected energy from the target is now residing in a single range line. This can be seen from Fig. 4.9, which is the plot of the signal energy after Stolt interpolation. It can be clearly seen here that compared to the curve in Fig. 4.7, in Fig. 4.9 the curvature has been corrected and it is now a straight line along the azimuth direction.

The final step in the RMA involves taking a two-dimensional inverse Fourier transform (2D-IFFT) which compresses the matrix in both the range and azimuth dimensions. Since the signal matrix after the Stolt interpolation is uniform in terms of k_x and k_y, the 2D-IFFT simply squeezes the energy reflected from each pixel point to its corresponding location of $(x_\mathrm{t}, y_\mathrm{t})$.

4.4.4 Time-Domain Back-Projection SAR Algorithm

In order to have a measure of the focussed SAR images obtained from RMA, another popular algorithm namely the time-domain back-projection algorithm (BP) was used for benchmarking [52]. As the name implies this is a time domain algorithm where the azimuth domain is not converted into the Doppler (spatial frequency) domain. This presents numerous advantages as compared to the frequency domain based processing algorithms such as RDA and RMA. Among them is the capability of handling non-linear trajectories as well as non-equidistant spaced measurements [53]. These advantages come at the cost of higher computational complexity and thus longer processing times.

Nevertheless BP is often used as a reference algorithm against which other algorithms are compared [53]. In a comparison between RMA and BP, it was found that in difficult conditions (uncorrected motion error and non-linear trajectories) the resolution of images focussed with RMA deteriorates sharply, while the images delivered by BP are mostly unaffected [54].

As the BP algorithm is used in this work for benchmarking purposes and is not a central part of the work, a detailed handling is not presented. For a more in-depth discussion of the algorithm, it is suggested to refer to [52, 55–57].

4.5 Concluding Remarks

Over the previous pages, it was discussed how automotive SAR applications differ from aerospace ones before the processing of acquired measurements was presented. Only the processing algorithms used in this work were discussed in a very condensed form, therefore a thorough literature study is recommended to gain a better understanding of the involved concepts.

Now that the fundamentals have been covered, the next chapters will present the measurements and results which were accomplished during this work.

5 Polarimetric Radar Cross-Section (RCS) Measurements of Traffic Objects

Ever since radars were first used extensively, the identification of targets based on their radar signatures has been important for aerospace radar systems and is always a topic of research interest [22].

Similarly in the automotive scenario, the importance of radar signatures of various traffic participants cannot be ignored. One important example of this is the issue of debris on the roads. This can be especially dangerous if the debris were lying on a major motorway where cars are expected to be driving at well over 100 km/h. It is then crucial for the car to make a decision whether the object in front of the car can safely be traversed over or whether an emergency braking manoeuvre is necessary [58].

5.1 Previous Research and Objectives

In the recent years there have been some efforts to investigate the radar cross-sections of various objects commonly found in typical traffic scenarios. Some of them have attempted to characterise vulnerable road users such as pedestrians at the communication frequencies as such signals are becoming ubiquitous in urban environments [59]. Meanwhile RCS measurements of humans in the 77 GHz band are reported in [60].

There are also some results published for the RCS signatures of various automobiles where the results have been simulated as well as measured [61, 62]. Additionally a polarimetric RCS characterisation of a passenger car (sedan) is also reported [63]. However, there have been no published results for the RCS measurements of traffic signs, guide and metal posts characterised in the co as well as cross-polarised channels.

The objective of the research presented in this chapter was to investigate whether typical traffic objects behave differently when they are illuminated by

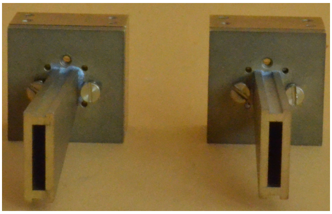

(a) Horns with identical beam patterns.

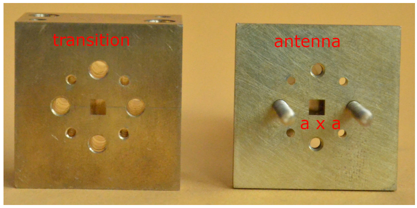

(b) Square feed of horns.

Fig. 5.1: The fabricated horn antennae. Image taken from [64].

horizontal or vertically polarised waves. Also of interest is the behaviour of the cross-polarised channel with respect to the different traffic objects and viewing angle.

Though before the measurements can start, it is first necessary to consider the antennae with which such polarimetric RCS measurements can be carried out. This will be done in the next section. Once this is accomplished, the RCS measurements can be tackled.

5.2 Design of Polarimetry Capable Antennae

For the successful polarimetric characterisation of traffic objects, it was first necessary to design and fabricate antennae which are orthogonally polarised, yet have identical beam patterns.

The additional requirement which too had to be met was that the fabricated antennae have strong polarisation decoupling which would allow the objects to be characterised.

Keeping in mind these requirements, it was decided to design horn antennae since they have the capability to provide strong polarisation decoupling as well as the larger gain associated with these antennae types.

Figure 5.1a shows the two horn antennae that have been designed and fabricated having identical patterns. Since the aperture has a larger dimension in elevation, the beam is narrow in elevation but in azimuth, the beam is much broader. This is necessary for the RCS measurements to ensure that the traffic signs which are characterised lie completely in the main beam to avoid multiple reflections between regions of the object that lie in the main beam and those that do not. The other advantage is for polarimetric SAR which also made use of the same antennae. It is an advantage to have a broad beam-width in azimuth to achieve fine resolution SAR images.

The requirement of identical patterns for the horn antennae led to another issue, which required an innovative solution. A pair of orthogonally polarised horn antennae, usually have their feeds rotated by 90° with respect to each other. This would imply that the apertures are rotated by 90° as well, which would defeat the purpose of having identical apertures in the first place. This puzzle was solved by designing a square shaped feed for both the horns, which provided rotational symmetry and hence the apertures would not have to be rotated with respect to each other but still be orthogonally polarised. A separate transition block was thus designed which would gradually taper from the rectangular E-band (WR-12) waveguide feed into the horn compatible square feed. The square feed and the transition are shown in Fig. 5.1b. On the right hand side in the image is the horn with its side where the transition is fixed, while on the left is the designed transition block with its horn compatible side shown.

The transition block gradually tapers the waveguide from a square (a x a dimensions) to a rectangular shape corresponding to the E-band (3.1 mm x 1.5 mm) waveguide. Thus by rotating the transition by 90°, the antenna polarisation is changed as well.

Figure 5.2 shows a plot of the measured gains of the pair of fabricated antennae between 77 GHz and 81 GHz. Below about 80 GHz, the difference in gain between the two antennae is approximately 1 dB. However, above 81 GHz the difference between the gains is at most 0.5 dB. This difference cannot be avoided in reality since there are tolerances in the fabrication process where some minor deviations can occur in the sub-mm range.

The azimuth beam patterns of the fabricated horn antennae are shown in Fig. 5.3. Shown is the co-polarised as well as the cross-polarised pattern.

As can be seen, the designed horn antennae have a strong polarisation decoupling capability of 27 dB at a minimum. Both horn antennae also have a measured gain of 17 dB.

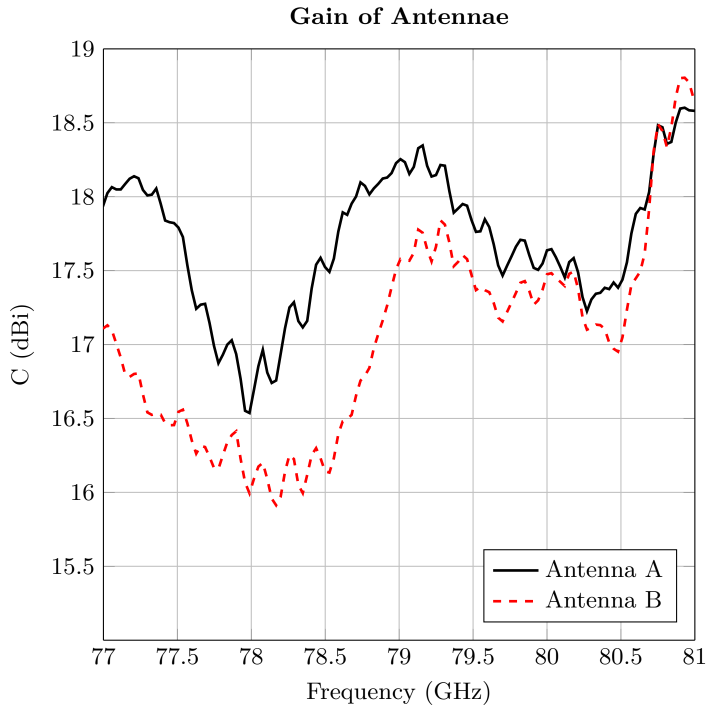

Fig. 5.2: Measured co-polarised gains of the fabricated horns.

5.3 Measurement Setup and Calibration

The radar cross-section (RCS) measurements were carried out in an anechoic chamber to reduce reflections from random objects as well as to minimise multi-path reflections. The target was fixed on a rotary stand which was programmed to rotate in steps of 1° starting from 0° and ending at 359°. In between two steps, the radar would make a measurement, so that the RCS could be calculated from every point of view in azimuth. The measurement setup is illustrated in Fig. 5.4a where the positions of the target and the sensor are shown. Fig. 5.4b shows one of the target traffic signs placed on the rotary

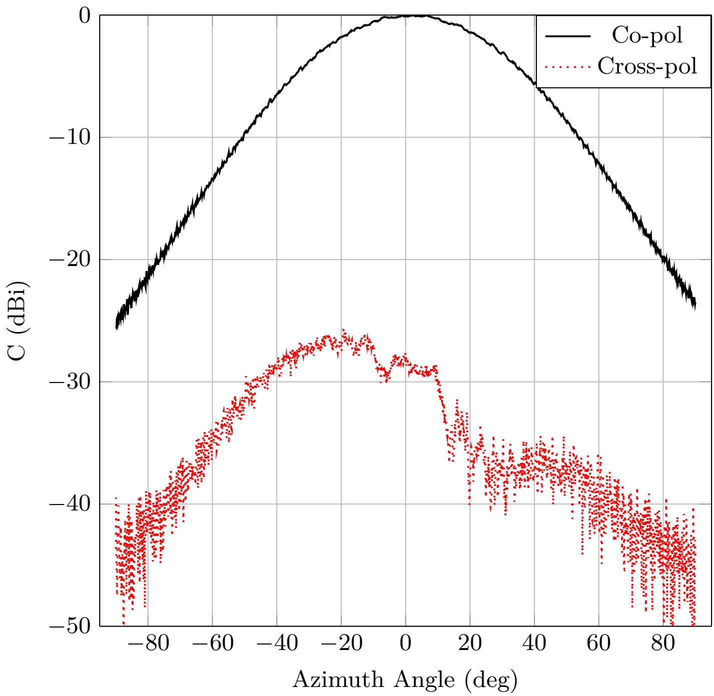

Fig. 5.3: Measured co-polarised (solid) and cross-polarised (dotted) beam patterns of the fabricated horns. Image adapted from [64] ©2017 IEEE.

stand for RCS measurements. The range to the targets placed on the rotary stand was measured to be 5.8 m.

However, before the radar cross-section measurements could be done, the measurement setup including the radar and the signal processing chain first had to be validated. In order to calibrate the sensor three simple targets were employed: a metallic sphere and two metal plates. The actual calibration was accomplished using the sphere, exploiting the polarisation neutral properties of spheres. The calibration sphere was placed at the same range as the actual targets and the reflected power measured. Then using the theoretical RCS

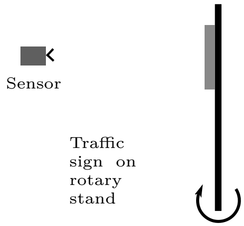

(a) Schematic of measurement setup.

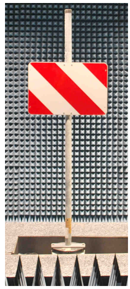

(b) Warning sign placed on rotary stand (shown here at the 180° position, see Fig. 5.5).

Fig. 5.4: RCS measurements setup. Image taken from [64].

of a sphere (RCS: $\sigma_{\text{sph}} = \pi r^2$ in the optical region where $\lambda \ll r$), the radar cross-sections of the metal plates are calculated as described below.

Using (2.16), the ratio of the scattering power from the calibration sphere can be expressed as [65],

$$|S_{21}^{\text{sph}}| = \frac{P_{\text{Rx}}^{\text{sph}}}{P_{\text{Tx}}}, \tag{5.1}$$

$$= \frac{G^2\lambda^2}{(4\pi)^3 r^4}\sigma_{\text{sph}},$$

$$= k_s\sigma_{\text{sph}}, \tag{5.2}$$

where P_{Tx} is the transmitted power, $P_{\text{Rx}}^{\text{sph}}$ is the power received after reflection from the calibration sphere, G is the antenna gain, r is the range to the sphere and k_s is a measurement setup constant which does not change as long as the measurement conditions and the set-up remain consistent.

Repeating the measurement now for a different target object, for example a metal plate,

$$|S_{21}^{\text{t}}| = \frac{P_{\text{Rx}}^{t}}{P_{\text{Tx}}},$$

$$= k_{\text{s}}\sigma_{\text{t}}, \tag{5.3}$$

with σ_t representing the RCS of the target object analogous to σ_sph of the sphere and k_s is the constant representing the measurement setup, both of which were introduced in (5.2) earlier. The radar cross-section of the target object (σ_t) can then be calculated by dividing (5.3) by (5.2) and multiplying by the theoretical RCS of the sphere [65]. Rearranging the equation and expressing it in logarithmic form gives

$$\sigma_\mathrm{t}\big|_\mathrm{dBsm} = \left|S_{21}^\mathrm{t}\right|_\mathrm{dB} - \left|S_{21}^\mathrm{sph}\right|_\mathrm{dB} + \sigma_\mathrm{sph}\big|_\mathrm{dBsm}. \tag{5.4}$$

The results of the calibration process are described in Table 5.1. Once the RCS of the sphere was measured, the measurement was repeated for two metal plates and the measured RCS of the sphere used to calculate the RCS of the metal plates. As the difference between the theoretical and the measured RCS of the plates is small, the measurement setup and the subsequent signal processing chain has been verified as valid.

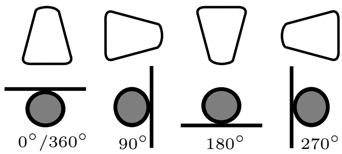

Fig. 5.5: Orientation of guide post (top) and traffic signs (bottom). Image taken from [64].

Fig. 5.5 serves to illustrate the orientation of the target traffic signs and objects when they were fixed to the rotary stand. The orientation scheme shown in Fig. 5.5 has been kept consistent throughout the measurements and hence the results discussed in the next section have all been obtained by use of

Tab. 5.1: RCS calibration values.

Calibration Object	Dimensions (cm)	Theoretical RCS (dBsm)	Measured RCS (arb. u. (dB))
Sphere	$\varnothing$ 30	-11.5	-97.1
Test Object	Dimensions (cm)	Theoretical RCS (dBsm)	Measured RCS (dBsm)
Plate	9.1×7.1	15.4	13.3
Plate	8×8	15.3	11.0

this orientation scheme. At 180°, the traffic sign is positioned such that the flat surface is aligned perfectly to the radar sensor, hence, the strongest specular reflection can be expected at this position.

The parameters of the radar sensor used for measurements within the scope of this work are summarised in Table 5.2. The finer range resolution, thanks to the high bandwidth allowed easy detection of behaviour patterns of the targets as they were rotated through.

Tab. 5.2: Radar parameters

Parameter	**Quantity**
Centre frequency	79 GHz
Bandwidth	4 GHz
Sampling frequency	6.25 MHz
Range resolution	3.75 cm

It is pertinent to mention here that the RCS measurements described in this chapter were all carried out in the near field region. This is logical since the traffic signs are almost always in the near field region as far as automotive radars are concerned. This is because even the smallest traffic signs have at least one dimension with a size of approximately 50 cm, which would place the far field region at more than 128 m. This distance is already at the boundary of the operational range of an automotive radar and the far field distance for larger signs would lie even further away [64].

5.4 Discussion of the Results

The results of the radar cross-section measurements are presented in the following sections. The behaviour of VH and HV was identical in all the measurements, hence only VH has been plotted in all the results for this chapter.

Guide and Metal Post

One of the most ubiquitous objects found in traffic are the black and white guide posts along the sides of the country roads and autobahns. The first measurement result is the comparison of the radar cross-section of one such guide post and that of a cylindrical metal post which is most often used to affix traffic signs. However for the purposes of this comparison, the measurement was carried out without any traffic signs fixed to the metal post, that is just the bare metal post was used as a target. The height of the guide post is 173 cm while the height of the metal post is 210 cm.

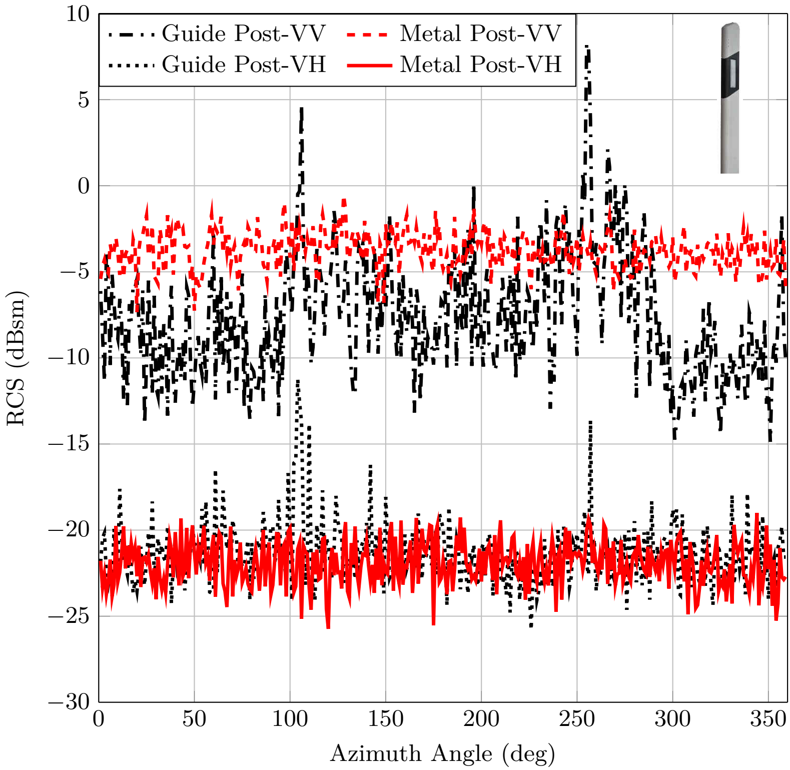

Fig. 5.6: RCS of metal and guide post (height of guide post is 173 cm, height of metal post is 210 cm). Image taken from [64].

Figure 5.6 displays the comparison of the RCS of both the guide and metal posts. The black lines represent the guide post, while the red lines the metal post. The metal post has a uniform co and cross-polarised RCS signature which can be understood when the symmetric structural form is taken into account. Since it has a smooth cylindrical surface, strong specular reflection is expected only from the small portion of the surface which is oriented at a right angle to the radar sensor. Any incident waves on the curved surface are deflected away. Therefore almost all of the incident waves experiencing a depolarisation are deflected away from the radar leading thus to a much lower cross-polarised RCS signature as compared to the co-polarised RCS.

The guide post on the other hand, reflects back much less incident energy, which is understandable considering the fact that the guide post is manufactured from a dielectric material. However, due to the shape of the guide post, as shown in Fig. 5.5, the RCS signature has some unique characteristics which can be understood once the shape is taken into account. The guide post has two distinct sharp peaks at 105° and 255° in both the co and cross-polarised pattern. These couple of angles correspond to the points where the two broad sides of the guide post are oriented such that the specular reflection from the surface of the guide post are aligned with the radar, resulting in a larger amount of received power in this particular orientation.

At all other angles, the incident energy is deflected away from the radar sensor by the curved sides of the guide post which leads to a lower RCS signature. Armed with this knowledge it is possible to differentiate between a guide and metal post. It is not a necessity that the metal post be the post used to hold up traffic signs, rather it could also be the bottom half of a traffic or street light for example. The bottom half because this effect is most useful at close ranges when the traffic sign is too high to lie in the main beam of the automotive radar sensor, which usually finds its place low in the front bumper. Therefore, if the received power demonstrates sharp peaks in the co-polarised as well as cross-polarised patterns, one can deduce that the object is a guide post. On the other hand, if the received power does not fluctuate but maintains a uniform profile, the target must be a cylindrical object [64].

Traffic Signs

The results of the measurements carried out with the traffic signs are shown in Figs. 5.7-5.10. Here the RCS patterns for four traffic signs of gradually increasing size are shown.

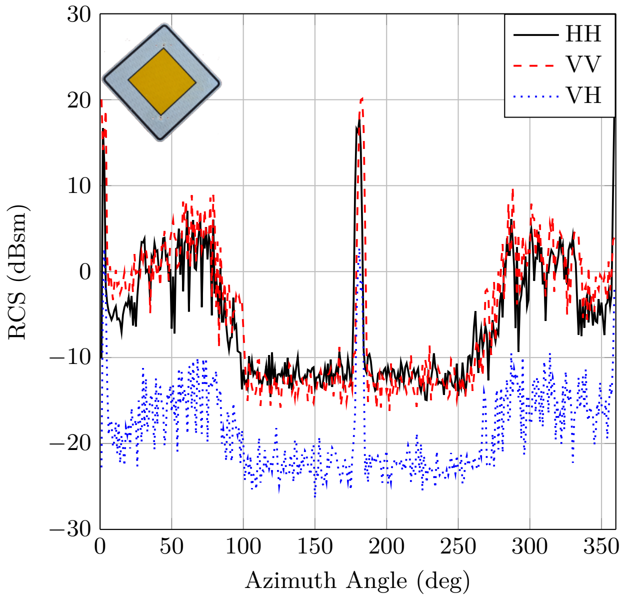

Fig. 5.7: RCS of priority sign (57 × 57cm). Image adapted from [64] ©2017 IEEE.

Figure 5.7 shows the RCS pattern for the priority sign, which is also the smallest of the traffic signs used for measurements. Shown are the two co-polarised patterns HH and VV as well as the cross-polarised pattern VH. At first glance, the behaviour of all three patterns seems to be very similar other than the obvious amplitude offsets between the co and cross-polarised returns (≈15 dB) corresponding to the polarisation decoupling and between HH and VV (≈3 dB) which is due to the difference in gain as discussed in Section 5.2 and shown visually in Fig. 5.2. Upon closer scrutiny it is possible to see that in the vicinity of 180°, the co and cross-polarised patterns differ significantly. This will be discussed in detail later.

At 180° the traffic signs are aligned perpendicularly to the radar sensor and hence a maximum of the incident energy is reflected back towards the radar. However, as the sign is rotated, the traffic sign deflects the incident energy away from the radar, thereby reflecting minimum energy towards the radar [27]. This effect is explained graphically by Fig. 5.11a.

In the region between approximately 270° and just before 360° as well as between just after 360° and 90°, the back of the traffic sign and the metal post used to hold up the traffic sign form a simple dihedral corner as illustrated in Fig. 5.11b. This effect reflects a significant portion of the incident energy back towards the radar. This phenomenon has been reported previously in literature [66].

In Figs. 5.8 to 5.10 are shown the same RCS signatures (HH, VV, VH) for the speed limit, warning and location signs. Each of these signs are progressively

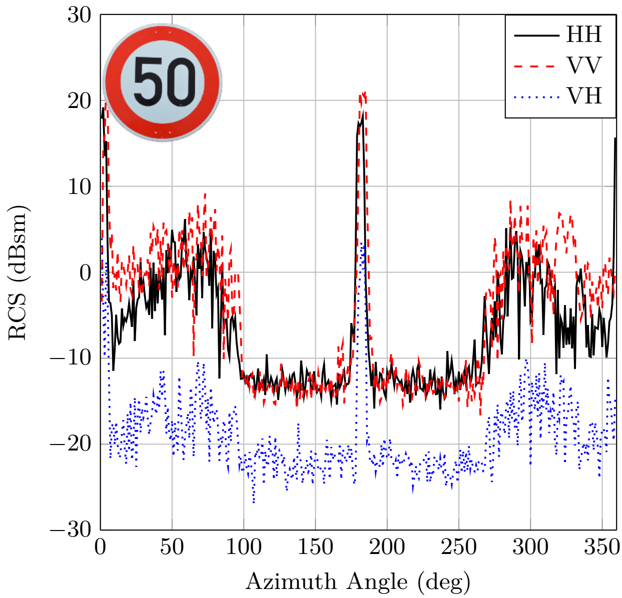

Fig. 5.8: RCS of speed limit sign (⌀ = 60 cm). Image adapted from [64] ©2017 IEEE.

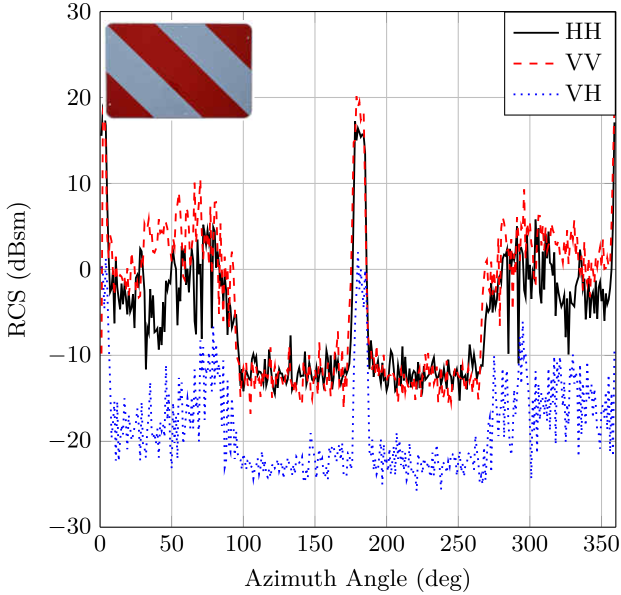

Fig. 5.9: RCS of warning sign (75 × 50cm). Image adapted from [64] ©2017 IEEE.

larger and in particular for the warning and location sign, wider than the previous ones. This fact is crucial for the analysis which follows. Upon examining the plots, it becomes evident that the peak at 180° is not sharp, rather there is some peak splitting. The peak splitting is even more pronounced for the cross-polarised pattern. For the co-polarised pattern, a plateau is formed and the width of this plateau is dependent on the width of the traffic sign; the wider the traffic sign, the wider is the plateau formed in the vicinity of 180°. The smallest traffic sign, the priority sign, in Fig. 5.7 has the slimmest peak while the location sign in Fig. 5.10 the broadest. This is contrary to expectations as literature shows that large metal plates have narrower RCS patterns when aligned with the radar and the traffic signs are metal plates. This phenomena is discussed in detail on the following pages.

Influence of the Near Field on RCS Measurements

To permit studying the effects described in the previous section, where the broader a traffic sign was the wider was the peak in the RCS signature when the traffic sign is oriented at bore-sight (at 180°) to the radar sensor, the previous RCS measurements were repeated. However, this time the goal was to gain a closer view of the peak at 180°, to enable greater scrutiny of the described behaviour. This was accomplished by firstly limiting the rotation of the traffic signs between 170° and 190° and secondly by reducing the step size from 1° to 0.1°.

Initially, the measurement was carried out for the warning sign and its zoomed RCS signature thus obtained is shown in Fig. 5.12. Here it is pos-

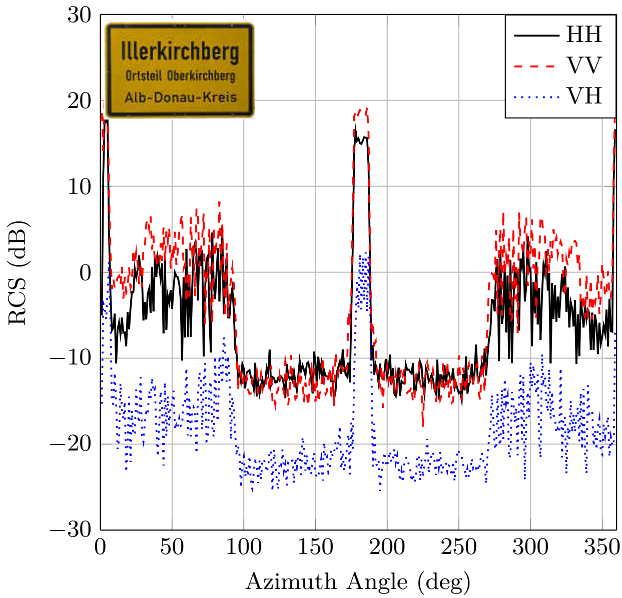

Fig. 5.10: RCS of location sign (100 × 65cm). Image adapted from [64] ©2017 IEEE.

(a) Sign deflecting incident energy. **(b)** Corner formed by sign and pole.

Fig. 5.11: Behaviour of traffic sign dependent on orientation. Image taken from [64].

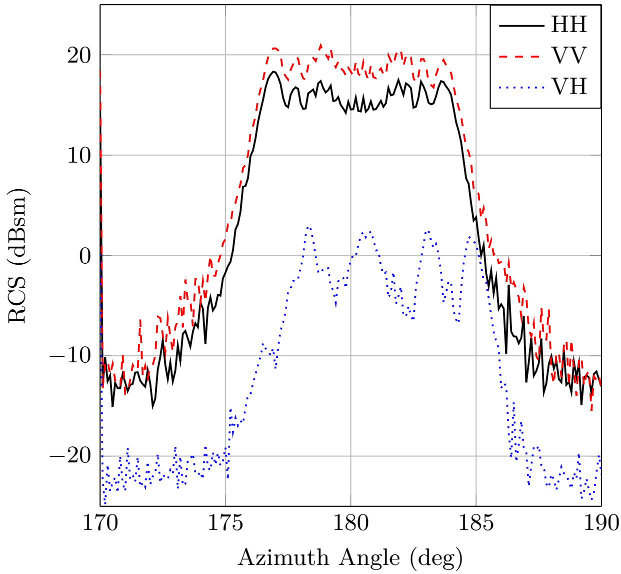

Fig. 5.12: RCS of warning sign zoomed in between 170° and 190°. Image adapted from [64] ©2017 IEEE.

sible to observe in more detail the profile of the RCS pattern as the traffic sign is rotated through the angle at which it is aligned to the bore-sight (180°) of the radar sensor. At first glance it becomes clear that the HH and VV patterns are very similar except for the 3 dB difference in amplitudes, which was discussed earlier in Section 5.4.

The HH and VV patterns form a plateau between approximately 177° and 184° which runs counter to what has been observed when the RCS pattern of a large metal plate has been measured [27]. However, for all such studies, it was ensured that the metal plate whose RCS is being measured was placed with such a separation from the radar sensor being used, to ensure that the metal plate is in the far field region of the radar and vice versa.

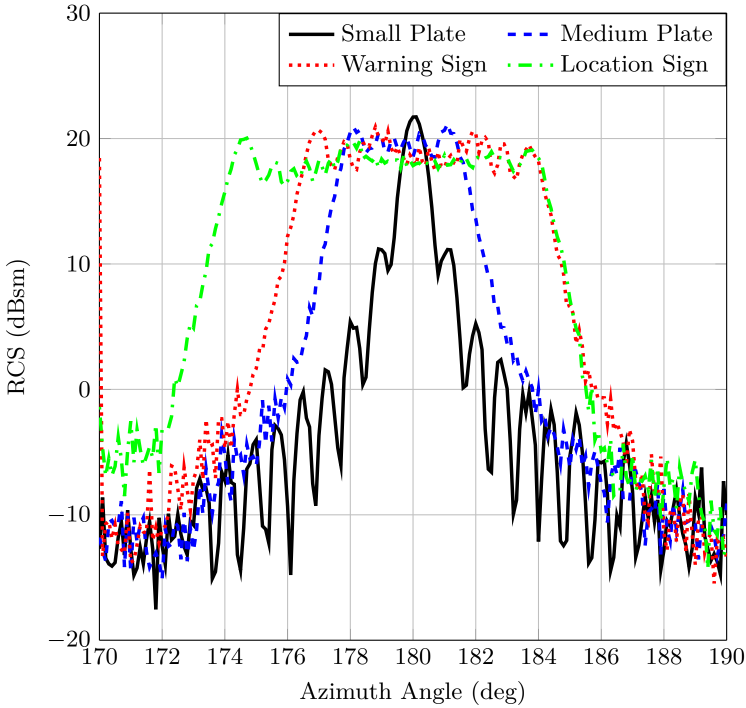

Fig. 5.13: Zoomed RCS of metal plates of varying sizes (co-polarised: VV). Image taken from [64].

The RCS signatures presented in this chapter have all been measured in the near field region however, for reasons discussed in Section 5.3. Therefore there

Tab. 5.3: Far field region of metal plates (& Traffic Signs).

Object	Dimensions (cm)	Fraunhofer Distance (m)
Small Plate	13.5×12.5	9.4
Medium Plate	50×30	129
Warning Sign	75×50	281
Large Plate (Location Sign)	100×65	500

is a significant departure from the RCS patterns of metal plates reported in literature. Similar RCS patterns have previously been reported in scientific publications [67–69]. The measurement with the zoomed in RCS signature was repeated with additional three metal plates (including the location size, the largest metal plate) and the results plotted together in Fig. 5.13.

Here the plot displays the RCS signatures starting from a small plate plotted in black to the largest plate plotted in green. It can readily be seen that the breadth of the plateau is successively wider for each step in size. The dimensions and the Fraunhofer distance for each metal plate used in the measurements are summarised in Table 5.3.

From Fig. 5.13 it is possible to see that the RCS of the three largest plates are very similar in characteristic, except for the width of the plateau. The RCS signature of the small plate though resembles that of a metal plate placed in the far field. From Table 5.3, it is possible to see that the far field region of the small plate begins from 9 m away. The effects though can already be seen at 6 m range where the metal plates were placed. Thus, there is a narrow peak at 180°, and the side-lobes are approximately 11 dB below.

The results presented are in harmony with the theoretical knowledge as in the near field the waves are spherical and cannot be approximated as plane waves. This holds specially true, the larger the target object becomes. Therefore, the tips of the wave reflected from the target cover a distance which is different from the distance the middle part of the wave travels. This causes a phase difference which in turn leads to stronger interference effects at the radar. On the other hand, the waves in the far field region are no longer spherical but plane which ensures that a narrow lobe corresponding to the direction of specular reflection is formed as there is a negligible phase difference between the tips and the crest of the wave [64].

Effects of Plate Edges on Cross-Polarised Returns

Thus far only the co-polarised RCS patterns had been discussed, but now the behaviour of the cross-polarised RCS pattern shall be examined. It is possible to see the cross-polarised RCS pattern of the warning sign in Fig. 5.12. One can clearly recognise a pattern here of sharp peaks and troughs occurring periodically.

In order to analyse this effect it is important to understand that the cross-polarised RCS signature in Fig. 5.12 shows the depolarised return from the target. That is, the incident polarised waves, which were horizontally polarised in the present case, had their state of polarisation rotated, so that they were vertically polarised instead. Between 170° and 190° the edges of the traffic sign cause the rotation of the polarisation [70]. The metal plate (warning sign) is only capable of reflecting the co-polarised waves back. The peaks in Fig. 5.12 occurs at locations where the waves interfere constructively, while at the troughs destructive interference takes place.

Taking into consideration the fact that the edges of the traffic signs (or metal plates) are responsible for the depolarisation of the incident waves, it is possible to hypothesise that wider traffic signs will produce a larger number of peaks and troughs, since even a small rotation of a large plate, causes large changes in the path differences of reflected waves and therefore presents greater chances or locations where the conditions for interference are fulfilled.

The cross-polarised patterns of the same set of plates whose details are discussed in Table 5.3, are illustrated in Fig. 5.14. Here the smallest metal plate (plotted in black) produces only one peak analogous to the one shown in Fig. 5.13. The medium sized plate has three distinct peaks and is roughly four times wider than the small plate. The next step in width is presented by the warning sign which is 25 cm wider than the medium plate. This corresponds to four peaks in the cross-polarised pattern in Fig. 5.14. The periodical increase of the peaks holds for the largest plate (the location sign) as well where another step of 25 cm in the width of the sign corresponds to five peaks in the RCS pattern.

It can be readily inferred with the help of Table 5.3 and Fig. 5.14 that the interference of the waves follows a periodic pattern, as each 25 cm step in width

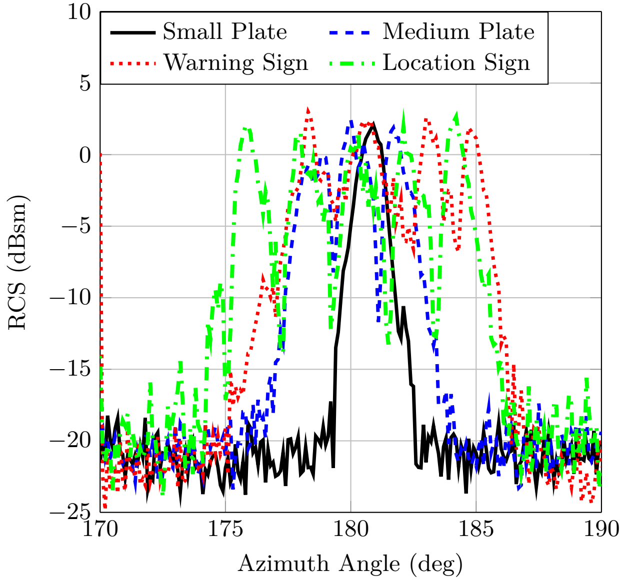

Fig. 5.14: Cross-polarised (VH) RCS patterns of the metal plates and the warning sign. Image taken from [64].

resulted in one more peak in the RCS pattern.

It has therefore been shown that the number of peaks in the cross-polarised RCS pattern are directly dependent on the breadth of the traffic signs as the larger signs present more opportunities where interference could occur.

5.5 Concluding Remarks

Over the previous pages, the results of the radar cross-section (RCS) measurements were presented and thoroughly discussed. Keeping the mentioned points in mind, it is necessary to briefly discuss how these results could be useful for automotive radars.

Some of the results presented could be helpful for some of the topics which are currently being dealt with in research, for example self localisation and creation of grid maps. Here it may be useful to differentiate between the different objects which may be found in the automotive environment. The ability to distinguish between a metallic post and a dielectric guide post as discussed in Section 5.4 would make the task of localisation easier. Additionally, it could also help in pre-crash sensing to ascertain in advance whether the imminent crash is with a hard metal object, where the change in momentum will be abrupt or with a softer plastic object which will not deliver such a sharp change in momentum. This information will definitely help in the pre-crash preparations carried out in the premium segment cars [71].

Judging whether placing a polarimetric radar sensor in cars is advantageous cannot be decided purely on the basis of the results presented on the previous pages. Though there was hardly any difference to see between the horizontally and vertically polarised RCS signatures, having an additional polarisation channel might offer a useful advantage in other avenues. This should become evident once the results obtained from clutter analysis are presented in Chapter 8.

6 Automotive Synthetic Aperture Radar (SAR)

Synthetic aperture radar has been used widely in the space and aerospace industry for decades as discussed in Chapter 4, however in this chapter, a new application, namely for the automotive sector, will be discussed.

The application of SAR to the automotive scenario is promising, since with conventional methods it is not possible to acquire information of stationary objects with a fine resolution. Moving targets separated by only a small distance (for example one car overtaking another) can still be discriminated as they would not have the same Doppler signature [23]. Indeed this can help in detecting and classifying the moving objects as cars, pedestrians or even inline skaters who can be classified based on their unique micro-Doppler signatures [72].

Closely spaced stationary targets are much more difficult to resolve accurately with the use of conventional radar signal processing. However with SAR it is possible to resolve stationary targets with a very high resolution such that the contours of parked cars, for example, can be accurately resolved. An additional advantage with SAR is that weak targets which would normally be hidden by the noise floor, can most often be rendered visible by SAR. This is due to the fact that with SAR, a large number of measurements are coherently integrated, which sinks the noise floor (since noise is random) while the weak target is made stronger since it is deterministic.

Therefore from the resulting images, it is possible to distinguish between the different stationary targets. The high resolution images provided by SAR can also be used for generating grid maps of the area surrounding the streets along which a car travels [73].

6.1 Why is Automotive SAR Needed?

To clarify what has been described in the previous paragraphs, consider the diagram in Fig. 6.1[1].

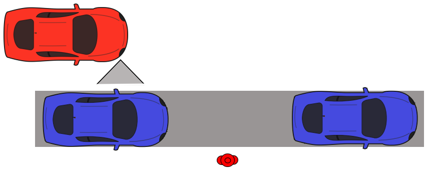

Fig. 6.1: Measurement geometry for automotive SAR. Scenario where the red car drives by the parked blue cars, looking for a spot to park.

Shown here is a situation which is ubiquitous in traffic situations in practically every city of the world. Though the exact situation may be vary, the principle is the same. There is a line of cars parked, lengthwise with some gaps in between. To accomplish a robust automated parking facility, it is necessary to first find these gaps existing in the line of parked cars and then, secondly, to arrive at a decision whether this gap is large enough to accommodate the vehicle being driven.

To accomplish this chain of decisions, the parking system needs inputs of the scenario which deliver quality information, on the basis of which, it could make a decision which fulfils the requirements of the situation, whether or not the gap is large enough and also if there are potentially any obstacles blocking the space or perhaps adjacent to it.

So far automated parking systems have been implemented with a combination of ultrasound parking sensors and short range radar sensors which can deliver images of the scenery. Unfortunately, both of these methods do not deliver high resolution information of the environment, due to which these systems face a situation where a skilled driver may be able to park the car into tight spaces himself, while the system judges the gap to be too small. To complicate the matters further, consider the situation shown in Fig. 6.1 again. There is a fire hydrant placed next to the parking space. Using conventional

[1]Image of car adapted from [44], licensed under CC0 1.0 Universal (CC0 1.0), Public Domain Dedication, https://creativecommons.org/publicdomain/zero/1.0/.

methods, it would not be possible for the automated parking vehicle to recognise that the fire hydrant is not blocking the parking space, rather it is placed well to the side.

This is the type of situation which is ideally suited for the deployment of synthetic aperture radar (SAR) as it can deliver high resolution images of the scenario using the same short range radar sensor. As it will be shown later in the chapter, with SAR it is possible to make out the contours of the parked cars as well other objects which may be found in traffic situations.

6.1.1 Previous Research and Objectives

The previous years have seen numerous implementations of automotive SAR being published [74–80]. In the beginning it was required to adapt the existing SAR algorithms from aerospace to automotive scenarios as well as to investigate the effects of sensor motion on the processed SAR images [74]. Based on the lessons learned here, it was possible to image a typical parking scenario by building a SAR demonstrator [75]. A gyroscope and an acceleration sensor were used to provide motion compensation information.

To support the ever increasing applications of neural networks based algorithms for camera systems in the cars, today the graphics processing unit (GPU) is gradually becoming commonplace in cars. Hence, the GPU could also be used for speeding up the processing for SAR [77, 78, 80]. This represents significant progress from 'offline' processing, where the measurement data processed after collection on a computer which itself may not be part of the measurement set-up, to 'online' processing. Here the data is processed as soon as it is available while new data is being acquired in the background.

All of the previously published implementations of automotive SAR have been accomplished with the help of expensive GNSS and IMU based dead-reckoning systems for gathering the trajectory information. These systems though useful for research efforts, do not translate well into commercial use. For automotive SAR to have a realistic chance of making its way into cars of the future, it is necessary to prove that it can be implemented at a lower cost. If SAR is indeed brought onto the automotive market, it would be implemented using the short range radars placed in the front corners of the car. The short range radar is usually a much more economically priced sensor when compared to the long range radar and it is therefore important to keep the complete cost to a minimum.

The central goals of the work presented here are

1. to adapt existing SAR algorithms from their original aerospace and space applications to automotive applications,
2. to identify the most suitable processing algorithm for the automotive scenario,
3. and to develop and present a low cost implementation of automotive SAR which demonstrates that SAR can indeed function without the use of cost intensive sensors for gathering trajectory information.

6.2 Automotive Synthetic Aperture Radar (SAR) Measurements

The implementation of automotive SAR can be cleanly divided into two phases. In the first phase, the goal was to investigate the feasibility of applying SAR algorithms for automotive applications. As such, the tasks involved identifying and adapting suitable existing SAR algorithms to the automotive requirements. Among other things, it concerned carrying out measurements with a 77 GHz radar sensor where the wavelength of operation is in the vicinity of 4 mm as opposed to a metre or more in aerospace and space SAR applications. Hence, in this phase, the motion of the car was simulated by using a linear rail unit which carried out stop and go measurements.

In the second phase, once the correct algorithms and processing techniques had been identified, the goal was to develop a realistic demonstrator as a proof of concept. These two phases each presented their unique challenges and opportunities which are handled on the next few pages.

6.2.1 Rail-SAR Measurements and Results

The first SAR processor to be implemented was the line-processing algorithm which is based in the time domain and hence lying on the far end of the spectrum with respect to the computational efficiency as discussed in Section 4.4.1. The line-processing algorithm was chosen since it is a good entry point into the topic and the concept of SAR can be effectively grasped through the understanding of the processor.

The radar parameters corresponding to the sensor used for the measurements carried out in the scope of automotive SAR are given in Table 6.1.

Tab. 6.1: Radar parameters

Parameter	**Quantity**
Centre frequency	79 GHz
Bandwidth	4 GHz
Sampling frequency	6.25 MHz
Ramp length	1024 Samples
Ramp repetition interval	850 µs

The radar sensor used for SAR measurements was a prototype designed at the institute for imaging purposes and was not capable of providing a sharp chirp rate. This was not particularly an issue for measurements with the rail unit, but did lead to restrictions in the implementation of a realistic demonstrator as will be discussed later in Section 6.2.2.

Fig. 6.2: Measurement set-up, front view of car. Length of rail unit trajectory is 4 m and closest range to the car is 1.6 m.

The measurement setup consisting of the linear rail unit is depicted in Fig. 6.2. The rail unit can be seen with a radar sensor fixed to it. The rail unit and the radar sensor were controlled by the same computer, hence the movements and measurements done by the sensor were always in sync. The step size of the rail unit was fixed to 0.5 mm. This ensured that the Nyquist sampling criterion was easily fulfilled, since according to the strictest conditions, a new range profile of the target scenery is required every 1 mm, since this is the $\frac{\lambda}{4}$ criterion to avoid azimuth target ambiguities [22].

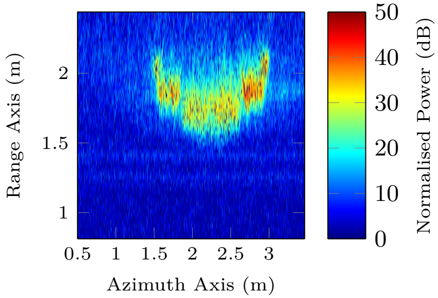

(a) SAR image obtained through line processing algorithm.

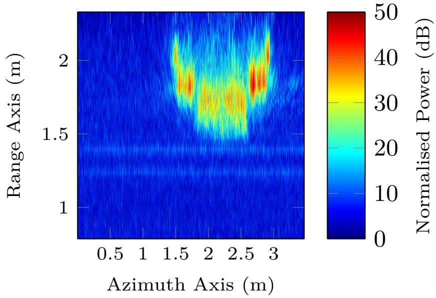

(b) SAR image obtained by range Doppler algorithm.

Fig. 6.3: Processed SAR images of the measurement scenario from Fig. 6.2.

The processed SAR images corresponding to the measurement setup from Fig. 6.2 are illustrated in Fig. 6.3. Figure 6.3a has been obtained from the line processing algorithm. Since the processing here is done in the time domain, without assuming that the received waves are plane (see Section 4.4.3), the SAR image thus obtained is the most accurate representation of the scene being imaged [22]. This however comes at a much higher computational cost (see Section 4.4.1). Figure 6.3b depicts the same scene in a SAR image which has been obtained by the range Doppler algorithm (RDA). As discussed in Section 4.4.2, RDA processes the measurements in the Range-Doppler domain, that is the azimuth frequency domain. Hence the processing is much more efficient (approximately 80% to 90%), compared to the line processing algorithm. The trade-off though is that the the curvature of the waves is not compensated completely as the received energy is assumed to be from plane waves [45]. This can lead to inaccurate images of the scene, though in the typical applications, the error is too small to be of serious concern.

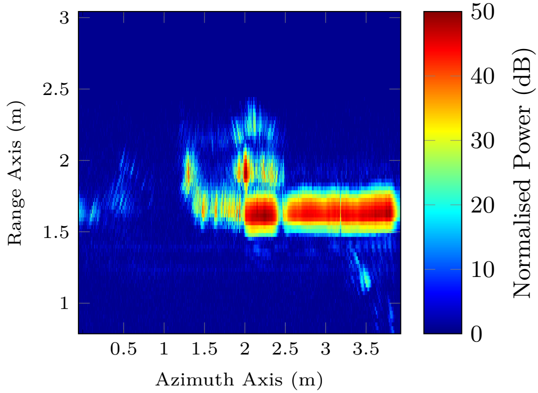

Fig. 6.4: Measurement result of rear right side of car from Fig. 6.2 obtained from RDA.

For the next measurement scenario, the rear right side of the same car shown in Fig. 6.2 was the target. The SAR image for this is shown in Fig. 6.4 which has been obtained from RDA. Here it is possible to see the reflections from the rear bumper of the car between approximately 1.25 m and 2 m in azimuth. Since this is made of plastic, the amplitude of the reflected signal is not as great as that from a sheet of metal, like the door starting from 2.5 m. In between, around 2.1 m in azimuth, is the wheel housing of the car. The wheel itself reflects strongly, due to the numerous layers (rim, brake pads, and wheel mounting for example) of metal which comprise the wheel itself. However, it is also possible to see reflections from behind the wheel, which are due to the wheel housing, that is also composed of metal. The range figure is spread due to the multiple bounces within the curved space of the housing before the signal arrives back at the radar sensor.

For all subsequent SAR processing, the line processing algorithm was gradually phased out owing to its computational expenses and little advantage presented by time domain processing as compared to RDA.

In order to investigate the ability of the SAR algorithms to resolve even small details of the target scene, a measurement of the scenario depicted in Fig. 6.5

was carried out. Here it is possible to see the rail unit based measurement setup in better detail. The two cars were parked close together to mimic an ubiquitous scene in parking garages, particularly in inner cities where cars are very often squeezed together. The gap between the cars was measured to be 62 cm.

Fig. 6.5: Measurement setup simulating a parking scenario. Image taken from [81].

The processed image of the measurement scenario from Fig. 6.5 is shown in Fig. 6.6. It is immediately clear that the two parked cars have been distinctly resolved. The gap between the two cars can also be made out to be approximately 60 cm.

An interesting observation that can be made from Fig. 6.5 is that the car on the right has a stronger reflection than the car on the left. This is explained by the fact that the car on the right has a bumper which is smaller, that is, it protrudes less from the body of the car. The difference in the depth of the bumper of the two cars was measured to be 5 cm. This explains why the reflection for the car on the left, which has a thicker bumper, the power reflected is less. For the car on the right, more of the transmitted energy was able to penetrate the bumper and be reflected from the metal underneath. While for the car on the left, more of the energy was attenuated by the thicker sheet of plastic in the bumper.

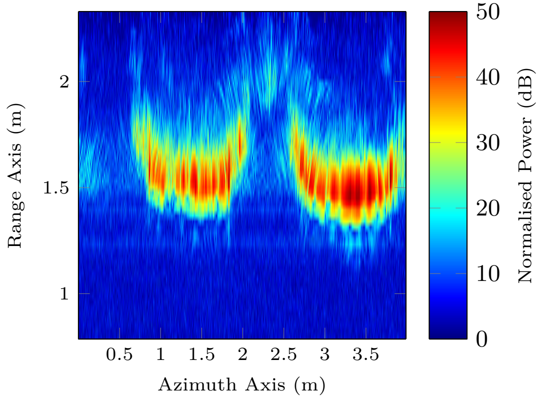

Fig. 6.6: Measurement result of two cars rear view from Fig. 6.5. Image taken from [81].

The results of this measurement are the proof of concept which prove the feasibility of the application of automotive SAR for parking applications [81].

Achievable Azimuth Resolution

Now that the first SAR measurements have been processed and presented, it is useful to investigate what azimuth resolution can be achieved using this measurement set-up. In Chapter 4 the theoretical azimuth resolution was introduced as $\frac{L}{2}$ according to (4.2). As discussed in Section 4.2 this theoretical azimuth resolution cannot be achieved in practice due to numerous reasons, some of which were discussed in that section.

In order to gauge the achievable azimuth resolution, an impulse response function (IRF) of the system is needed. For this a point target is used, usually a corner reflector and its processed SAR image is analysed. To do this the intensity response of the image is plotted for the range bin which has the point target over the complete azimuth trajectory. Just such a plot is shown in Fig. 6.7 for the linear rail based measurement set-up and RDA processor.

To estimate the achieved resolution, one reads the azimuth spread at the point which is 3 dB weaker than the maximum of the point target. This spread

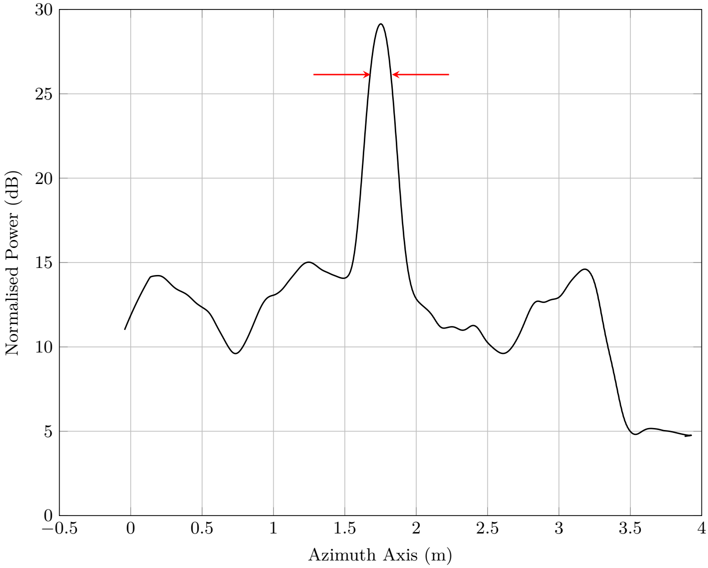

Fig. 6.7: Impulse response function plotted for the range-Doppler algorithm using the linear rail.

is shown by the red arrows in Fig. 6.7. The complete spread indicated by the red arrows is 150 mm. The best achieved resolution is then half of this, that is 75 mm since if another point target was placed next to the current one with a spacing of 75 mm, it would be possible to just about differentiate between the two targets. In the case of larger targets however, the reasonable expected resolution would be closer to 150 mm.

The theoretical azimuth resolution is 2 mm which is very different from the achievable resolution of 150 mm. Some possible reasons for this in addition to those discussed in Section 4.2 are the position inaccuracies resulting from the rail unit. The rail unit is driven by a stepper motor which turns and pulls a rubber belt which in turn moves the radar fixed to the movable platform. Any small errors in the step size would thereby contribute to minor degradations in the achievable resolution. At the frequency of 77 GHz, the wavelength is roughly 4 mm, thus even small position errors are in proportion to the wavelength larger.

A mathematical description of the tolerance limit for along track position errors can be obtained using (4.6) [22]

$$\phi_{\mathrm{e}} = \frac{2\pi}{\lambda}(2\Delta R_{\mathrm{e}}) = \frac{2\pi}{\lambda}\left(\frac{d_{\mathrm{e}}^2}{R}\right), \tag{6.1}$$

where ϕ_{e} represents the phase error, d_{e} the along track error distance, R the range to the target and ΔR_{e} the difference between the expected and actual paths to and from the target. Setting the maximum tolerable phase error to $\frac{\lambda}{4}$, one can solve for d_{e}

$$d_{\mathrm{e}} = \sqrt{\frac{R\lambda^2}{8\pi}}. \tag{6.2}$$

This results in an error term which is directly proportional to the root of the range to the target. This is due to the fact that targets at large ranges have a longer exposure time than for targets at closer range and therefore any position errors influence the phase term for closer targets more severely.

Additionally the RDA assumes that the waves reflected from the target and arriving at the sensor are plane as discussed in Section 4.4.2. This does not hold true for shorter ranges and therefore the range migration algorithm should be able to provide a finer azimuth resolution.

In the next step, the processing chain needs to be adapted such that measurements done by a realistic setup could be processed as well.

Adaptation of Algorithm to Accelerated Platform Motion

To enable the processing of radar measurements gathered from a sensor fixed on a platform which moves continuously without stopping, as opposed to the rail unit which paused after each step, certain changes needed to be made to the signal processing chain. This was necessary for a realistic implementation for automotive applications.

Using the linear rail unit, the step size was always constant, hence the radar measurements were equidistant from the beginning. This is however not possible in a realistic application where a radar sensor is fixed on a car. The car

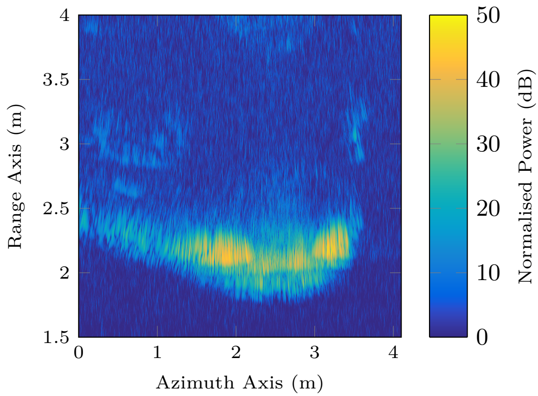

Fig. 6.8: SAR image (from RMA) obtained without acceleration compensation.

may accelerate, decelerate or move at a constant velocity which implies that the measurements will not be equidistant since the radar cycle time is usually fixed. The automotive SAR system thus needs to be able to adapt. This is however an issue when using any synthetic aperture radar (SAR) algorithm which employs a Fourier transform in the azimuth direction. This is because, it is inherently assumed that the measurements available are equidistant/periodic. This is a requirement of the Fourier transform [43].

It is assumed that the acceleration of the sensor is constant between two consecutive measurements and the distance thus moved is given by

$$s = uT_r + \frac{1}{2}aT_r^2, \tag{6.3}$$

with s representing the distance moved in the time T_r which is the chirp repetition time, u the initial velocity of the platform and a the acceleration experienced by the platform.

Substitution of (6.3) in (4.4) results in the signal representation acquired by a platform undergoing acceleration as

$$s_\mathrm{if}(t_\mathrm{azi}, f(t)) = A_\mathrm{if}e^{-jf(t)\sqrt{(uT_r+\frac{1}{2}aT_r^2-x_\mathrm{t})^2+y_\mathrm{t}^2)}}. \tag{6.4}$$

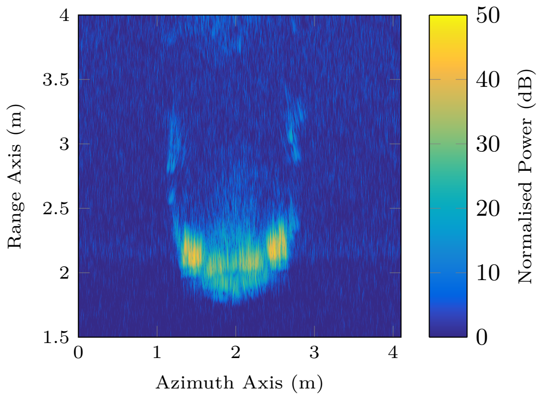

Fig. 6.9: SAR image (from RMA) obtained after acceleration compensation through interpolation.

The non-uniformity of measurements in the azimuth direction introduces sub-optimal azimuth compression of targets. Hence, before the radar measurements are passed to the SAR algorithm for processing, they need to be pre-processed so that they are made equidistant. This is done by re-sampling the measurements in the azimuth direction through interpolation such that the measurements are uniformly spaced and satisfy the Nyquist sampling criterion [82]. A cubic spine interpolation is employed for this purpose since it offers high accuracy for this purpose [83].

To simulate radar measurements taken by a car undergoing acceleration, the measurement from Fig. 6.2 was repeated, however this time the radar measurements were done at points which were not equidistant, rather step sizes were calculated for a car accelerating at $5\,\mathrm{ms}^{-2}$. This value was deliberately chosen to be so high, since if the interpolation can function for an exaggerated amount of acceleration, it should be able to handle realistic values of acceleration.

To process the measurements into SAR images, the range migration algorithm (RMA) was used since it is better suited for applications where the range to the targets of interest is smaller, as RMA does not approximate the curvature of the wave [45]. This leads to better and more accurate results. RMA was discussed in detail in Section 4.4.3.

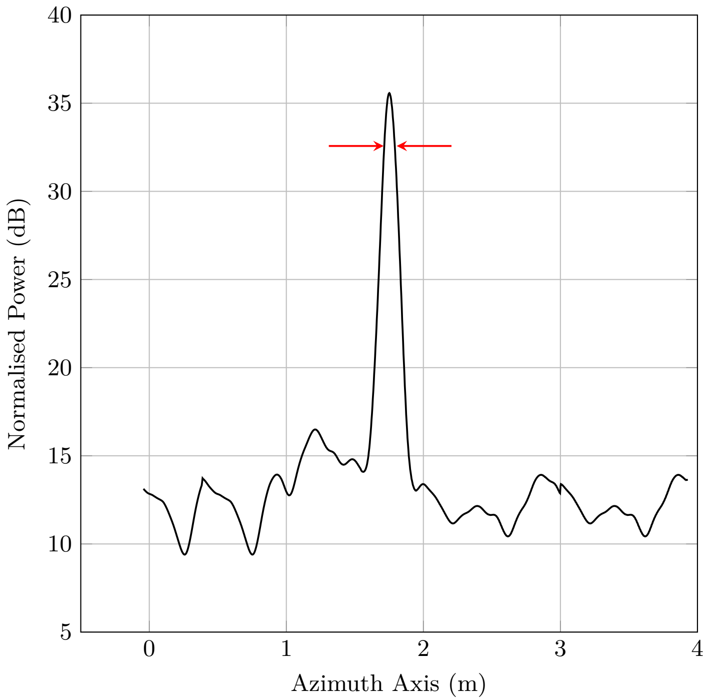

Fig. 6.10: Impulse response function plotted for the range migration algorithm using the linear rail.

From Fig. 6.8, it is possible to see the effects when the radar measurements are not corrected for the acceleration of the platform. The car was positioned in azimuth between the 1 and 3 m mark. However, in the image the car has been shifted as well as being blurred and suffering from broadening.

Although for this particular measurement scenario, most of the car is discernible, the situation would be much worse if for example instead of one car, there were a row of parked cars similar to the two cars parked in the scenario from Fig. 6.5. In this case, the blurring would render it unable to distinguish the gap between the parked cars. In the case where there was hypothetically an empty parking space next to a car, it would lead to false results regarding the breadth of the space due to the blurring of the image.

The effects of acceleration were compensated and the SAR image obtained through processing the corrected measurements is shown in Fig. 6.9. Here none of the blurring evident in Fig. 6.8 is found. The car is correctly focused and placed in the correct position in azimuth and range.

The impulse response function (IRF) for the range migration algorithm is displayed in Fig. 6.10. The spread at the 3 dB mark, indicated by the red arrows, is 95 mm. Therefore the achievable resolution for targets larger than a corner (point target) reflector would thus also be 95 mm as discussed briefly in Section 6.2.1. This is an improvement over the achieved resolution (150 mm) with RDA. The reasons for this have been discussed previously, chief among them the fact that RDA assumes the waves received are plane while RMA does not.

It has been therefore shown that the signal processing chain can accommodate radar measurements which are not equidistant and obtain SAR images from them, which depict the targeted scenario accurately.

6.2.2 Implementation of a SAR Demonstrator

Since the signal processing portion of the tool-chain is ready, the focus can now be turned to the task of developing the hardware which can acquire the radar measurements in sync with odometry data which can be processed into SAR images. The most challenging task for the implementation of a SAR demonstrator is the gathering of odometry data so that the position of each radar measurement can be accurately calculated. This is a critical requirement for the correct processing of images.

An ideal approach would be to employ multiple acceleration sensors and an inertial measurement unit (IMU) along with at least one rotary encoder, much like has been reported in [75]. The data from these multiple sensors is usually weighted which represents the reliability of the values. For example the data from an acceleration sensor is usually strongly affected by noise and hence has lower weighting, while the data from a rotary encoder is reliable and is given higher weighting. The acceleration sensor though can deliver data at a higher rate than the rotary encoder, hence a Kalman filter is employed to calculate a trajectory from these data streams [84]. When a navigation solution from a GNSS receiver is additionally input to the Kalman filter, reliable dead reckoning can be accomplished with the help of which precise trajectory information can be gleaned.

This task in itself however, requires enormous efforts to deploy, which would lead away from the actual scope of the intended research, to demonstrate the feasibility of synthetic aperture radar (SAR) in delivering high resolution images for automotive applications. Thus it was decided to concentrate on restricting the targeted application to single dimension trajectories, without any motion compensation in the lateral dimension. The goal was thus to present a low-cost SAR demonstrator operating at 77 GHz using minimal hardware. For this requirement, a single rotary encoder should suffice. The demonstrator was implemented using a hand-pushed cart.

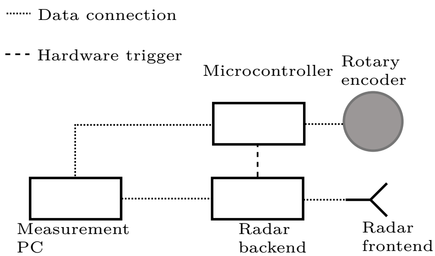

Fig. 6.11: Block diagram illustrating the architecture of the SAR demonstrator.

The architecture of the SAR demonstrator can be understood from Fig. 6.11. The rotary encoder was fixed to a wheel on the non-steering axis of a push-cart which functioned as the SAR demonstrator. This ensured the trajectory could be correctly calculated without the deterioration from the inaccuracies introduced by the small steering corrections necessary to maintain the straight track of the cart. The solid lines show a data connection between the various blocks, while the dotted line depicts a hardware trigger signal sent from the radar backend to the microcontroller at every instant when an FMCW ramp would be transmitted. This ensured that the microcontroller could save the number of ticks at the time when the FMCW ramp was transmitted as well as attach a timestamp (time from start maintained by the microcontroller, accurate to 4 µs) to the value. Additionally, it also guaranteed that the two timelines of the radar and the microcontroller interfacing with the rotary encoder would be tightly coupled.

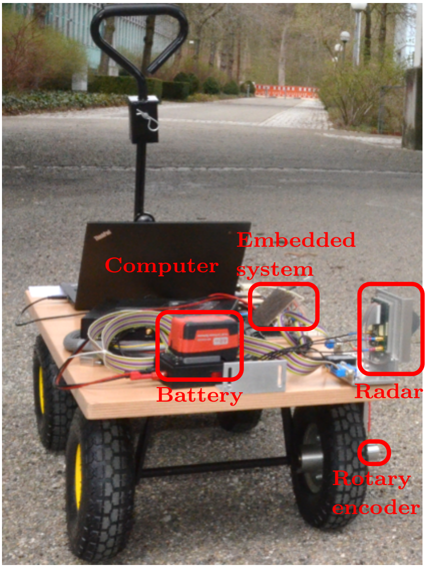

Fig. 6.12: Trolley based SAR demonstrator. Image adapted from [82] ©2018 IEEE.

The measurement setup described above can be seen in Fig. 6.12 with the important components highlighted and labelled. Thanks to the battery supply, the SAR demonstrator is self-sustained and portable. Hence it can be deployed easily anywhere since no electric outlets are needed.

Azimuth Sampling Rate

Now that the measurement setup has been coarsely described, it will be discussed how the task of acquiring one (FMCW) ramp roughly every mm was accomplished. To prevent ambiguities, the radar had to transmit enough chirps that the Nyquist sampling criterion was fulfilled. Thus a step size has to be calculated where a radar measurement (azimuth sample) needs to be captured. The theoretical background of this shall now be discussed.

The received signal after down-conversion shown in (4.4) can also be represented as [14],

$$s_{\mathrm{IF}}(X_{\mathrm{azi}}, K_{\mathrm{r}}) = A_{\mathrm{IF}} \mathrm{e}^{-\mathrm{j} K_{\mathrm{r}} \sqrt{(X_{\mathrm{azi}} - X_{\mathrm{t}})^2 + Y_{\mathrm{t}}^2}}, \tag{6.5}$$

where A_{IF} represents the amplitude of the signal, X_{t} and Y_{t} are the coordinates of the pixel being imaged, X_{azi} is the azimuth position of the radar along the track and

$$K_{\mathrm{r}} = \frac{4\pi}{c_0} \left(f_{\mathrm{start}} + \gamma \hat{t} \right) \tag{6.6}$$

with f_{start} being the start frequency of the chirp, γ the chirp rate and $\hat{t}$ the fast time. The instantaneous frequency of the received signal from the target at $(X_{\mathrm{t}}, Y_{\mathrm{t}})$ can be found by taking the partial derivative with respect to the azimuth domain [82],

$$\begin{aligned} k_{\mathrm{x}}(X_{\mathrm{azi}}) &= \frac{\partial}{\partial X_{\mathrm{azi}}} \left(-\mathrm{j} K_{\mathrm{r}} \sqrt{(X_{\mathrm{azi}} - X_{\mathrm{t}})^2 + Y_{\mathrm{t}}^2} \right) & (6.7) \\ &= \frac{K_{\mathrm{r}} (X_{\mathrm{t}} - X_{\mathrm{azi}})}{\sqrt{(X_{\mathrm{azi}} - X_{\mathrm{t}})^2 + Y_{\mathrm{t}}^2}} \\ k_{\mathrm{x}} &= K_{\mathrm{r}} \sin \left(\theta_{\mathrm{t}}(X_{\mathrm{azi}}) \right), & (6.8) \\ \text{where} \quad \theta_{\mathrm{t}}(X_{\mathrm{azi}}) &= \tan^{-1} \left(\frac{X_{\mathrm{t}} - X_{\mathrm{azi}}}{Y_{\mathrm{t}}} \right) & (6.9) \end{aligned}$$

is the aspect angle when the radar is located at $(X_{\mathrm{azi}}, 0)$ and the target pixel is located at $(X_{\mathrm{t}}, Y_{\mathrm{t}})$ [43].

The concept of aspect angle is explained visually with the help of Fig. 6.13. The radar is shown at the beginning position of its track at position $\left(-\frac{\mathrm{L}}{2}, 0\right)$, while the blue coloured target at $(\frac{\mathrm{L}}{2}, Y_{\mathrm{max}})$ is the farthest target in this scenario, thus creating the largest aspect angle [82].

Application of the Fourier transform along the azimuth direction on (6.5),

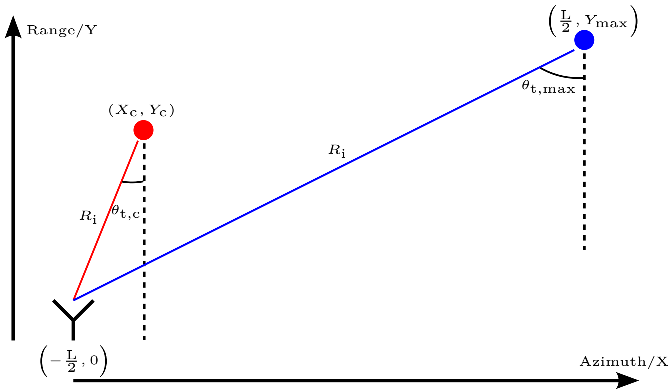

Fig. 6.13: Illustration of measurement geometry. $\theta_{t,max}$ is the maximum aspect angle and R_i is the slant range to each target or pixel. Image taken from [82].

results in the following form of the received signal

$$S_{IF}(K_x, K_r) = A_{IF} e^{-jY_t\sqrt{K_r^2 - K_x^2} - jK_x X_{azi}}, \tag{6.10}$$

where K_x denotes the spatial frequency (Doppler) domain with the corner points at $K_x \in \left[k_x(-\frac{L}{2}), k_x(\frac{L}{2})\right]$ [43]. The Doppler bandwidth thus becomes [43],

$$\Omega_t = \left(-K_r \cdot \sin\left(\theta_t(\frac{L}{2})\right), K_r \cdot \sin\left(\theta_t(\frac{L}{2})\right)\right). \tag{6.11}$$

The complete Doppler bandwidth for the entire scene is therefore the *union* of the support bands of each receive signal (S_{IF}),

$$\begin{aligned} \Omega_s &= \cup\Omega_t \\ &= \cup\left(-K_r \cdot \sin\left(\theta_t(\frac{L}{2})\right), K_r \cdot \sin\left(\theta_t(\frac{L}{2})\right)\right) \\ &= \left(-K_r \cdot \sin\theta_{t,max}, K_r \cdot \sin\theta_{t,max}\right), \end{aligned} \tag{6.12}$$

where $\theta_{t,max} = \tan^{-1}(\frac{L}{Y_{max}})$ is the largest aspect angle as illustrated in Fig. 6.13.

Based on the above calculated Doppler bandwidth for $S_{\mathrm{IF}}(K_\mathrm{r}, K_\mathrm{r})$, the maximum step size in azimuth which satisfies the Nyquist criterion can be calculated as

$$\Delta x \leq \frac{\pi}{K_\mathrm{r} \cdot \sin\theta_{\mathrm{t,max}}}. \tag{6.13}$$

To sum up the importance of the preceding paragraphs, the greatest azimuth sampling needed for ambiguity free processing of SAR images is given by (6.13). This value depends strongly on the position of the furthest target in a measurement scenario. For a range of 6 m, a Δx of 1.5 mm was calculated. This represents the measurement scenarios which are covered here.

A detailed description of the measurement control software can be found in Appendix B.

6.2.3 Processing Algorithm: The Sub-Aperture Approach

Now that the measurement setup for acquiring automotive SAR data has been developed and tested, it is necessary to delve into the signal processing chain needed to process the measurements into SAR images.

In order to devise a realistic SAR implementation, the measurements were processed such that, as if they were being recorded in real time [82]. The measurements were acquired in blocks with a pause in between, which was necessary due to hardware restrictions.

This is shown schematically in Fig. 6.14, where the blue chirps represent the block of FMCW ramps which precede the red chirps in time. Thus all measurements can be broken down into blocks and processed block-wise. The first block (blue chirps) are placed into a two dimensional matrix and padded with zeros. This is represented in Fig. 6.14 by blue space for the signal data from the block of blue chirps and white space for the zeros.

Next, a second 2-D matrix is created and the red chirps are copied into it as shown in Fig. 6.14, with zeros filling in the space where the blue chirps were copied in the first matrix. This creates a cascade of 2-D matrices which can be processed independently. This is repeated for all the blocks until all the chirps have been copied into their respective 2-D matrices.

In an actual automotive implementation, the signal data from the radar would only be available block-wise, hence this algorithm can be implemented

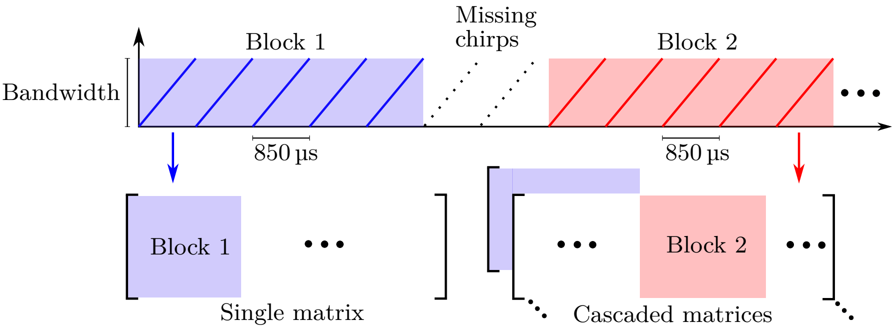

Fig. 6.14: Realistic implementation of the processing algorithm. Image taken from [82].

smoothly by copying each new available block of chirps into a new 2-D matrix and processing it directly. This would enable real-time processing and display of processed SAR images.

Now that the signal data has been copied into the respective matrices, the matter of the missing chirps can be dealt with the goal of minimising their impact. To this end a compressed sensing approach is presented after a brief introduction of the topic in the next few paragraphs.

Compressed Sensing for Recovering Missing Information

The utility of compressed sensing (CS), to glean more information even at the cost of not fulfilling the Nyquist criterion, has increased manifold since it was first introduced in 2006 [85]. This ultimately relaxes the requirements on communication systems and makes possible the recovery of corrupted data in signals. The effectiveness of compressed sensing for radars has also been reported [86], while the most interesting aspect is the feasibility of CS for synthetic aperture radar imaging [87]. It has been shown that by employing CS, the number of transmitted and received radar signals required for the processing of SAR images can be significantly reduced.

An *iterative method with adaptive threshold* (IMAT) based compressed sensing approach is used here [88]. This is where a threshold is set at the start and in each consecutive iteration, the threshold level is sunk. Thus in each next iteration, a greater number of data points are used for the reconstruction of the missing information. This is explained in greater detail in the next paragraphs for the SAR application.

The data in the cascaded matrices are the inputs to the CS algorithm. Initially the missing chirps are set equal to zero after which a two-dimensional fast Fourier transform is carried out. The data is thus now in the range-Doppler domain. Initially the threshold is set to be the maximum peak power (β). Every peak that is higher than this threshold is used to estimate the missing samples in an initial approximation. In subsequent iterations a new lower threshold is selected according to

$$T_{\mathrm{n}} = \beta \mathrm{e}^{-\alpha n}, \tag{6.14}$$

with T_{n} representing the threshold for iteration n and α is a parameter which determines how quickly the threshold is reduced with each iteration [89]. The stopping criteria is set such that the limit for the threshold level is always at least 10 dB higher than the noise floor. This ensures that the noise power is not used for estimation.

Use of CS to recover the missing data improves the dynamic range as well as the sharpness of the processed SAR images since without the recovery of the missing chirps, the data is processed with the gaps and this significantly reduces the amount of available information of the target scenery. This leads to a reduction of the dynamic range available in the SAR images which is thus avoided with this approach.

Since the radar measurements are now sorted, each cascaded matrix is individually processed as described in Section 6.2.1, just the way it would be for a real time implementation in a car. Therefore, all the motion compensation steps along with the correction for non-uniform azimuth sampling is carried out on each matrix before it is input into the range migration algorithm (RMA) to be processed into one SAR image corresponding to one sorted matrix. Finally all the SAR images are summed together to produce one complete SAR image of the target scenery.

This approach has been dubbed the sub-aperture approach, since it involves dividing the aperture into smaller sub-apertures which speeds up the processing time and enables real-time processing.

6.2.4 Measurement Results

Though the developed SAR demonstrator was used to evaluate various measurement scenarios, only two of them are discussed below since they are a representative set. The scenarios are depicted in Fig. 6.15, where in Fig. 6.15a the rear end of a car is seen as well as the demonstrator. Meanwhile Fig. 6.15b displays a parking scenario similar to the one shown in Fig. 6.5.

(a) Back view of car with the SAR demonstrator visible as well.

(b) Two cars parked next to each other with a gap of 60 cm. A common parking lot scenario.

Fig. 6.15: Outdoor measurement scenarios. Images taken from [82].

The processed SAR images corresponding to Fig. 6.15a are shown in Fig. 6.16. The first image, Fig. 6.16a shows the SAR image obtained through the subaperture algorithm using RMA without the reconstruction of the missing chirps as discussed previously. Comparing this image to Fig. 6.16b, for which the missing chirps have been re-constructed using compressed sensing, one can see that thanks to reconstruction of the missing signals, the image of the car is a bit sharper and better focussed. There is slightly less blurring around the edges of the car which is an indication of improved dynamic range within the image.

Figure 6.16c shows the SAR image obtained from the backprojection algorithm which was discussed shortly in Section 4.4.4 and is used here as a comparison for the SAR images processed using RMA. The data for this image were not enhanced with compressed sensing, since it is used here purely for benchmarking purposes and not presented as a core processing algorithm. Comparing Fig. 6.16c to Fig. 6.16a, one can see that the two SAR images are very similar with neither of the two algorithms presenting a difference with respect to the quality of the image.

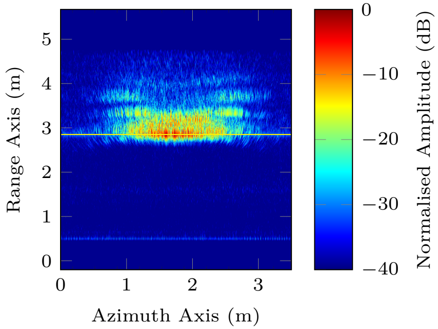

(a) SAR image obtained from subaperture algorithm without compressed sensing.

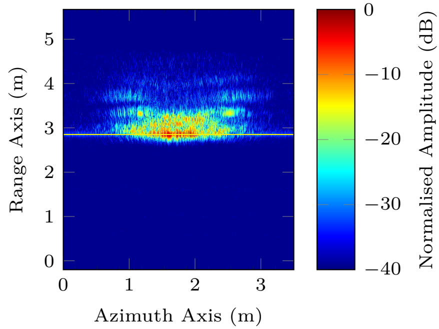

(b) SAR image obtained from subaperture algorithm with compressed sensing.

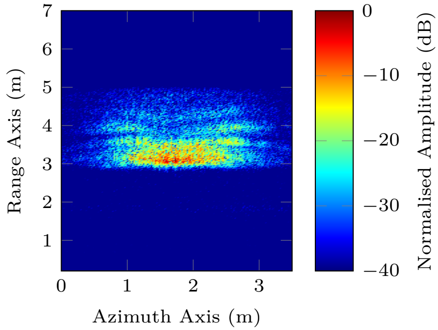

(c) SAR image obtained from the backprojection algorithm.

Fig. 6.16: Processed SAR images of scenario from Fig. 6.15a. Images taken from [82].

In order to evaluate the the improvement in the processed SAR image by the use of CS, the same azimuth stripe was taken from Fig. 6.16a and Fig. 6.16b and plotted in Fig. 6.17. Plotted here is a single azimuth stripe across the image, at a range such that the envelope of the car is covered with the point which reflects the maximum amount of incident energy. The location of the

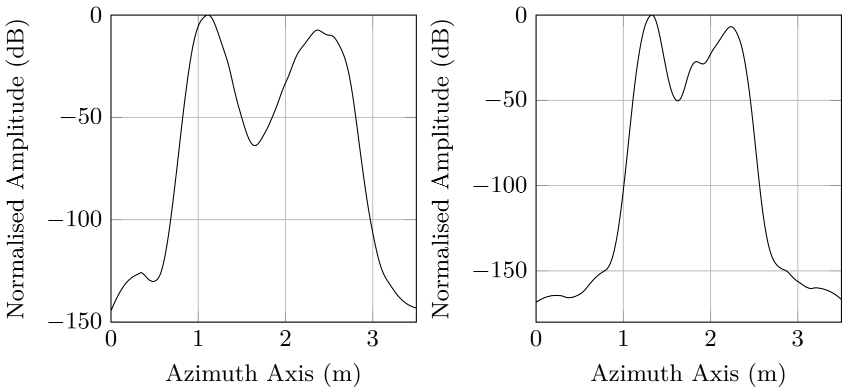

(a) Stripe of SAR image from Fig. 6.16a without CS.

(b) Stripe of SAR image from Fig. 6.16b with CS.

Fig. 6.17: Plot of stripes across azimuth of the SAR images in Fig 6.16.

stripes are indicated by the yellow lines in Fig. 6.16a and Fig. 6.16b.

Shown in Fig. 6.17a is the azimuth stripe corresponding to Fig. 6.16a, that is the image without CS. Here it is possible to see the ambient noise floor in the image at 0 m in azimuth before the response from the car starts and the amplitude increases sharply. This pattern is repeated on the other side of the car where the amplitude drops down to the approximately 150 dB noise floor.

The improvement brought by CS can be seen when Fig. 6.17a is compared to Fig. 6.17b which shows the same stripe taken from Fig. 6.16b, that is the SAR image with reconstructed chirps. Upon comparison it becomes immediately clear that the transition between noise and the response from the car are sharper, the car itself is slimmer while in Fig. 6.17a the car is broader. This is evidence that the car is more sharply focussed in the SAR image where the chirps have been reconstructed by using CS. Finally the noise floor in Fig. 6.17b is approximately 20 dB lower than that in Fig. 6.17a. This shows that there is much less image blurring around the car, that is in the region of transition between the noise floor and the car itself.

The effect of reconstruction through compressed sensing is not pronounced due to the fact, that the number of chirps missing from in between two blocks of chirps is not very large. This is because the trolley was pushed at a slow speed, from which it logically follows, that the track moved by the trolley during the time when no chirps were transmitted remains small. Hence the target information missing, which is reconstructed by compressed sensing, is inherently small. The improvement in Fig. 6.16b would be greater for a platform which moves at a higher speed, for example a car.

There are two reasons why the demonstrator trolley had to be moved at a slow pace:

1. As mentioned previously in Section 6.2.1, the prototype sensor was able to only transmit slow, long ramps. Hence it was necessary to have the trolley move slow, so that the Nyquist criterion for azimuth sampling is not violated. The maximum speed where the Nyquist criterion is fulfilled is 4 km/h. This corresponds to an average walking speed of a person [90].
2. Since the trolley did not have any means of absorbing shocks, it was important to push it at a slower pace to avoid damage to any hardware components.

The processed SAR images from the scenario depicted in Fig. 6.15b are shown in Fig. 6.18. Fig. 6.18a and Fig. 6.18c show images without reconstruction obtained from RMA and backprojection respectively. The two images are again very similar, however, the backprojection algorithm offers a slightly better dynamic range, especially for the second car on the right.

The advantage of compressed sensing is much more pronounced for this scenario as illustrated by Fig. 6.18b. The contours of the two cars are much clearer and there is much less noise in the image. This is particularly true for the region between the two cars, where there is significant blurring due to missing chirps.

The improvement available by the use of CS can again be gauged from the plots of the azimuth stripes in Fig. 6.19 and the locations of the stripes are once more indicated by the thin yellow lines in Fig. 6.18a and Fig. 6.18b. Comparing the azimuth stripe taken from the image without chirp reconstruction (Fig. 6.19a) with the azimuth stripe taken from the image with reconstruction (Fig. 6.19b), it is possible to see once again that the cars in the image without reconstruction are broader. Additionally the noise floor in the image with CS based chirp reconstruction is an estimated 50 dB lower. This is espe-

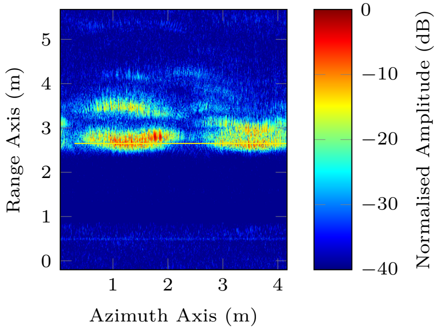

(a) SAR image obtained from subaperture algorithm without compressed sensing.

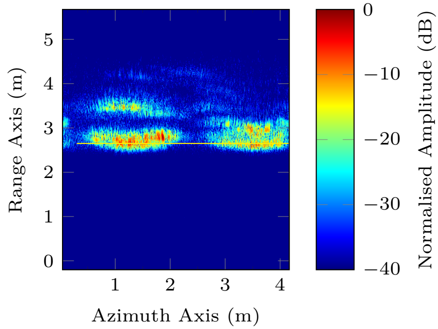

(b) SAR image obtained from subaperture algorithm with compressed sensing.

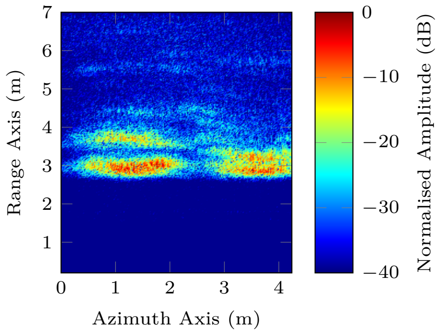

(c) SAR image obtained from the backprojection algorithm.

Fig. 6.18: Processed SAR images of scenario from Fig. 6.15b. Images taken from [82].

cially true for the region between the two cars where the amplitude drops off to the ambient noise floor. This region has a much higher amplitude in Fig. 6.19a than in Fig. 6.19b. This is indicative of more blurring prevalent in the image without CS based reconstruction.

The impulse response function (IRF) for the set-up described in Section 6.2.2 is displayed in Fig. 6.20. Using this IRF it is possible to arrive at the achiev-

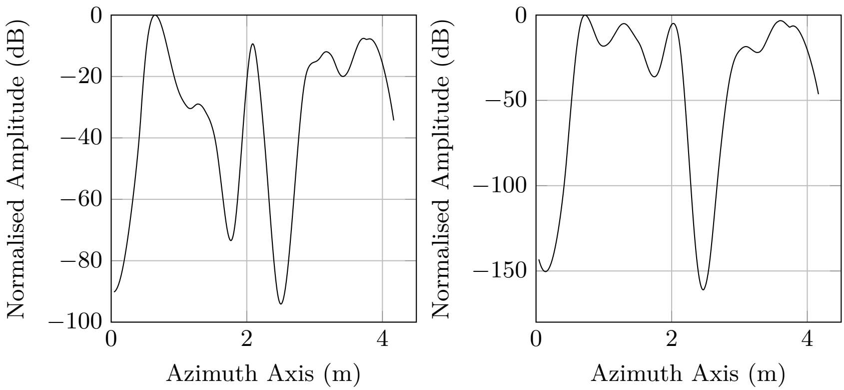

(a) Stripe of SAR image from Fig. 6.18a without CS. **(b)** Stripe of SAR image from Fig. 6.18b with CS.

Fig. 6.19: Plot of stripe across azimuth of the SAR images in Fig 6.18.

able azimuth resolution of 320 mm. Comparing the IRF obtained from the SAR demonstrator with that obtained (Fig. 6.10) from the rail based set-up, it becomes clear that the resolution has considerably deteriorated in moving from the linear rail based set-up to the trolley set-up. This is however hardly surprising as SAR with a linear rail unit is almost an ideal measurement environment since the sources of errors are low.

The trolley based measurement set-up though suffers from larger position uncertainties as the accuracy of the position from the rotary encoder is in the region of 1 mm. Additionally the trolley does not have wheels fitted with suspension, hence when it is pushed, the radar sensor is displaced vertically whenever the wheels encounter a bump on the road. This movement of the radar was not measured and therefore also not compensated. Another factor which played a role in the deterioration of the achievable resolution is the fact that the wheels of the trolley were not perfectly round, therefore while pushing the trolley, the radar sensor itself would also move vertically owing to uneven rolling form of the wheels.

These problems though should play less of a role in an actual car as the cars

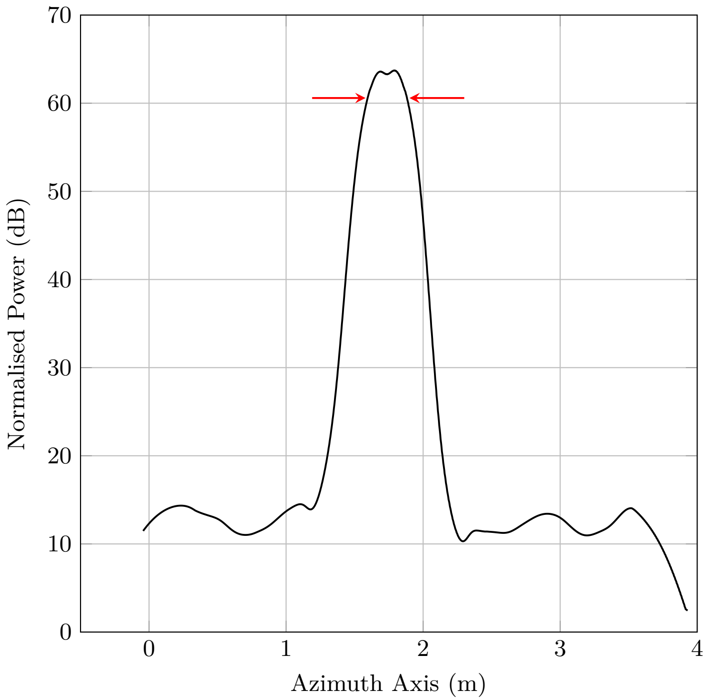

Fig. 6.20: Impulse response function plotted for the range migration algorithm using the trolley.

have wheels with suspension systems built around them and the shape of the car tyres are closer to a perfect round.

6.3 Concluding Remarks

In this chapter it has been shown that synthetic aperture radar (SAR) has tremendous potential. On the basis of the work presented here, it has been made clear that an implementation of SAR for automotive applications is definitely feasible. In fact there have already been efforts made to implement SAR in real time in a car [78] [77]. These approaches make use of the fact that the backprojection algorithm can be calculated in parallel. However, this can result in an advantage when using a graphical processing unit (GPU) only.

7 Polarimetric Synthetic Aperture Radar for Automotive Applications

Another dimension can be added to the already potent synthetic aperture radar (SAR) imaging technique, by using a fully polarimetric radar sensor. Indeed it has been shown that with the use of polarimetric SAR, it is possible to estimate the biophysical properties of forests and hence to acquire an estimate of how much carbon is sequestered in the forestlands on Earth [91]. This is made possible by polarimetric SAR, where the scattering of polarised waves by the canopies of the trees or bushes, gives important clues regarding the species of the vegetation [92].

Just as the forests provide ample features which can depolarise the incident waves, there are plenty of facets, curved surfaces and edges which are interesting points of target for a polarimetric automotive SAR imaging system. In this chapter after an introduction and a summary of existing literature, the various shapes and sides of a car will be examined using different linearly polarised radiation. Places like the wheel housing and the underside of the car have numerous curved surfaces which should depolarise the incident waves significantly and make the contour of the car easier to see than with single polarised waves as presented in Chapter 6.

7.1 Introduction to Automotive Polarimetric SAR

When evaluating polarimetric SAR data for Earth remote sensing applications, the data is normally processed to separate the radar returns from the different scatterers found on the planet's surface. Fields, meadows, roads and oceans all scatter the radar waves in a similar fashion, single bounce back towards the radar [38].

The majority of man-made structures however reflect the waves with a double bounce back towards the radar. In essence buildings and houses combined with the ground that they are raised on, make rudimentary dihedral corners which reflect the incident energy back [38]. It is possible to distinguish these scattering mechanisms through decomposition of the received signals by using an algorithm, into the components which correspond to the scattering mechanisms (single or double bounce) experienced by the reflected signals [29].

7.1.1 Suitability of Pauli Basis Vectors

One of the more common methods used for the decomposition of the received signals are the Pauli basis vectors as discussed in detail in Section 3.4.

Shown in Fig. 7.1 are two waves incident on and being reflected from a flat horizontal surface. Both the waves are linearly polarised, however in Fig. 7.1a the electric field vector does not coincide with the vertical or horizontal plane as the direction of propagation is at an oblique angle. The electric field vector can however be decomposed into its vertical and horizontal components with respect to the reflection interface. Here it is possible to see that the vertical component does not change upon reflection, however the horizontal component is flipped. [32, 93].

The same applies when another linearly polarised wave is incident on the same surface. This can be seen in Fig. 7.1b. Here a vertically polarised component does not exist but the horizontally polarised electric field vector is again flipped. It can thus be inferred that the vertically polarised wave does not experience a phase change on reflection but that the horizontally polarised wave undergoes a phase shift of 180° [32, 93].

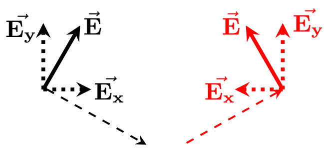

(a) Vertically polarised wave.

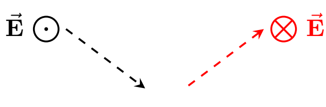

(b) Horizontally polarised wave.

Fig. 7.1: Waves incident at angles greater than 0°.

This behaviour can be understood by considering the reflection coefficients for the vertically and horizontally polarised waves shown in Fig. 7.2 [94]. As can be seen from the plot, the horizontally polarised wave always has a phase change of 180° irrespective of the angle of incidence. As for the vertically polarised wave, the phase remains unchanged with increasing angle of incidence until the Brewster angle is reached. At this angle, the reflected energy for the vertically polarised waves drops to zero and afterwards increases again, however with a phase change of 180° [30].

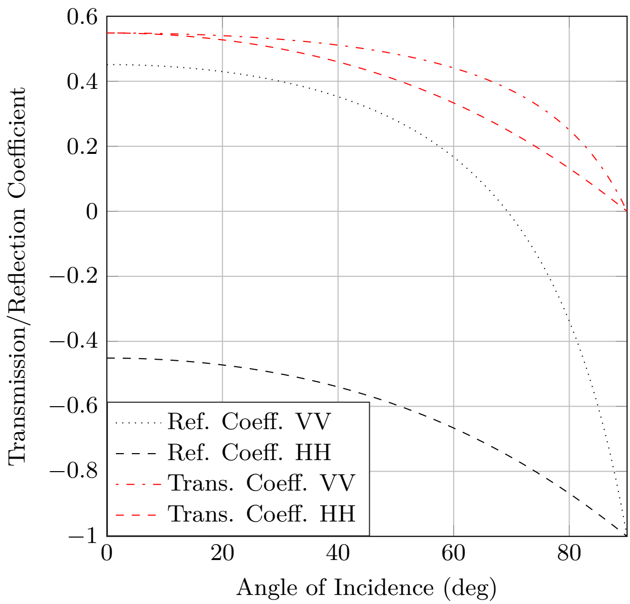

Fig. 7.2: Transmission and reflection co-efficients for a material with $\epsilon_r = 7$.

The scenarios in Fig. 7.1 however represent the aerospace applications, where the radar is at a high altitude above Earth and the angle of incidence is greater than 0°. This is however not true for automotive applications, which shall now be considered.

The scenario depicted in Fig. 7.3 represent the typical angles of incidence for automotive applications. When the waves are incident normally onto a surface, there is no distinction between the horizontally and vertically polarised

(a) Vertically polarised wave. **(b)** Horizontally polarised wave.

Fig. 7.3: Waves incident at 0°.

waves, as with respect to the surface, both electric field vectors lie in the plane of the surface [32]. Therefore, the behaviour of both waves at the reflecting surface is identical as illustrated in Fig. 7.3a and Fig. 7.3b for the vertically and horizontally polarised waves respectively. Consider again the reflection co-efficient for the horizontally polarised wave plotted in Fig. 7.2. At normal incidence, the vertically polarised wave is actually horizontally polarised, since it is perpendicular to the plane of incidence. Therefore at normal incidence, there is no difference between the behaviour of the horizontally and vertically polarised waves.

This implies, that for the automotive case, Pauli vectors would not give cogent results. This is however not a huge loss, as in the automotive scenario, there are hardly any targets which would cause diplane scattering. Due to this reason, alternative methods are needed to evaluate the imaged scenery.

7.1.2 Previous Research and Objectives

Up to the current point in time, there have been no efforts to investigate the feasibility of polarimetric SAR for automotive applications. However considering some of the applications from aerospace SAR mentioned at the beginning of this chapter and those discussed in [95, 96], one can see that polarimetric SAR can be utilised to extract target information which is not accessible with single polarisation SAR images. This is possible due to the nature of the objects which are imaged: forests, man made structures, glaciers and ocean surfaces. These targets differ in their compositions as well as their structures in that they offer a plethora of curved and sloped surfaces to the incident waves from a radar.

It was discussed in Section 3.3 that curved and sloped surfaces introduce cross-polarised components to the incident radiation which can be detected by a polarimetry capable radar sensor. The same principles will apply to targets in the automotive scenario as well because cars have plenty of sloped and curved surfaces which cause depolarisation and thus could deliver more information about their scattering centre.

The objective of the work presented in this chapter is therefore,

1. to investigate whether typical automotive targets are able to significantly depolarise incident waves,
2. to examine if polarimetric SAR for automotive targets is able to deliver any new information not available with conventional automotive SAR,
3. and to ascertain whether the sloped surfaces of cars aid in their contour estimation which can help with orientation estimation.

On the following pages the measurement set-up and scenarios will be discussed with the goal of achieving the above mentioned objectives.

7.2 Measurement Setup

The antennae and radar sensor used to carry out the polarimetric SAR measurements are the same as described in Sections 5.2 and 5.3. The height of the sensor was 35 cm. The radar parameters used for the measurements are hence also identical and are reproduced in Table 7.1.

Tab. 7.1: Radar parameters

Parameter	**Quantity**
Centre frequency	79 GHz
Bandwidth	4 GHz
Sampling frequency	6.25 MHz

The measurement scenario for the polarimetric SAR measurements was the same as described previously in Section 6.2.1. The radar was fixed onto the linear rail unit and moved in steps so that a new radar measurement was acquired every 1 mm. The difference this time though, was that the radar was polarimetric capable. Each received polarisation was handled as a unique channel, hence a separate SAR image was calculated for HH, VV and HV. However, only the HH co-polarised and HV cross-polarised returns were considered since the two co-polarised and the two cross-polarised channels are identical. There are no differences in behaviour between VV and HH and between VH and HV.

The goal of the first measurement carried out was to test the setup and validate the signal processing chain. Hence this measurement was done in an indoor garage hall. The measurement setup is shown in Fig. 7.4. The length of the virtual aperture, the distance the radar sensor moved is 4 m.

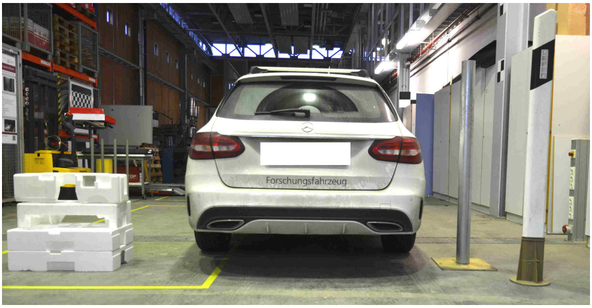

Fig. 7.4: Indoor measurement setup in a car garage. Height of sensor: 35 cm. Image taken from [97].

The target scenery included along with the rear view of the car, a metal cylinder, a guide post found alongside major roads (see Section 5.4) and a small metal plate fixed to a polystyrene board. The metal plate was used for calibration purposes. The guide post and metal cylinder were placed as targets so that their signature in polarimetric SAR images could be observed.

7.3 Measurement Results

The processed PolSAR images corresponding to the setup from Fig. 7.4 are shown in Fig. 7.5. In both the SAR images, the azimuth axis is longer than 4 m, the reason for which is azimuth zero-padding. Every antenna has a specific beam-width and thus receives reflections from objects which lie on either side of the antenna and within the beam-width. By extending the aperture in azimuth (through azimuth zero-padding) one can prevent targets, which lie beyond the extreme points of the synthetic aperture, from folding back into the image by offering them room to populate in their actual locations.

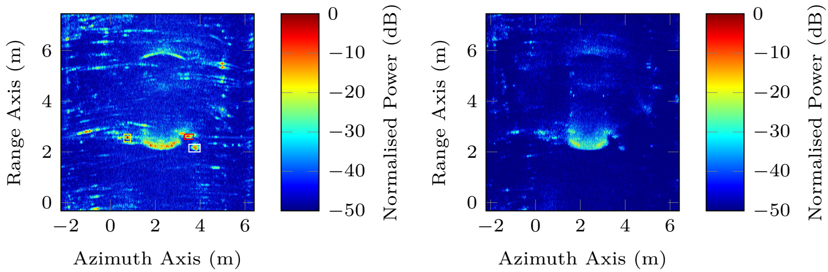

(a) Co-polarised image (HH) with clutter from various objects. **(b)** Cross-polarised image (HV) with much less clutter.

Fig. 7.5: PolSAR images of the car garage measurement scenario from Fig. 7.4. Images taken from [97].

Figure 7.5a displays the co-polarised image, where one of the first observation are the relatively large number of reflections from objects other than those visible in Fig. 7.4. This can be understood by taking into account the fact that this measurement was carried out in an indoor garage where a lot of random objects were lying around. The erratic reflections from these objects and the walls of the garage resulted in waves finding their way back to the radar after numerous reflections. The received energy from the erratic reflections is much lower in the cross-polarised image in Fig. 7.5b. This is because most of the objects present in the garage had flat surfaces which do not constitute depolarising targets and therefore the reflected waves had the same polarisation as the incident waves.

One concern here is whether the PolSAR measurement setup has any implicit errors where the attenuation or a mismatch in the cross-polarised channel with respect to the co-polarised channel for example, leads to sharp differences in received signal levels. To eliminate such effects, all the measured channels (both co and cross-polarised) were normalised to the global maximum for the measurement scenario which was determined from all the measured channels (HH, VV, HV). Thus it was assured that any differences in received signal amplitudes are due to the behaviour of the target under the differently polarised incident waves. This was implemented for all the SAR images presented in this chapter.

To gather a sense of the signal to noise ratio, the returns belonging to the car and the targets were cropped out and the remaining image was processed to estimate the clutter level from the many 'unintended' targets in the hall which clutter the SAR image in Fig 7.5a. The average noise level was thus found to be $-38\,\mathrm{dB}$ while repeating the process for the cropped part of the image with the car and targets gave the average signal level of $-22\,\mathrm{dB}$. Thereby for the measurement scenario from Fig. 7.4 a signal-to-clutter level of approximately $16\,\mathrm{dB}$ was achieved for the co-polarised channel. The same figure for the cross-polarised channel is $20\,\mathrm{dB}$ as the drop in clutter is much more than the drop in signal power from the targets.

The metal (marked by a red rectangle) and guide (marked by a white rectangle) post are both clearly visible in the images, though the guide post does not have a uniform profile owing to its shape. The metal plate (marked by a yellow rectangle) is clearly visible as well. The metal and guide post have weak profiles in the cross-polarised image since they both are not depolarising. The metal plate has an even weaker profile in the cross-polarised image since it does not have any curvature which can depolarise the incident waves.

Additionally, in the co-polarised image in Fig. 7.5a, it is possible to see the far end (front) of the car. This occurs due to the tunnelling effect, where the waves propagate in a zigzag manner, reflecting between the ground and the underside of the car.

Finally, in the cross-polarised image in Fig. 7.5b it is possible to just barely make out the sides of the car, while in the co-polarised image, this is simply not possible. This property of the cross-polarised image is important and needs to be further tested to see if the outline of the car can be seen consistently in other measurements.

In Fig. 7.6 are shown the different measurement scenarios which were investigated in the scope of this dissertation. The same car was used for the measurements to attain PolSAR images of the car from all unique sides which would enable a characterisation of the car.

The first measurement to be considered is that of the rear view of the car

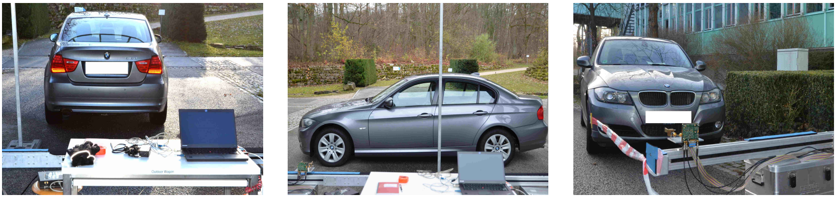

(a) Back view with a pole. **(b)** Side view with a pole. **(c)** Front view with a bush.

Fig. 7.6: The outdoor measurements were carried out with the same car to have its PolSAR images from all unique sides. Height of sensor: 35 cm. Images taken from [97].

shown in Fig. 7.6a. The target, other than the car, is the metallic pole. This metallic pole though does not have a cylindrical shape, rather it is irregularly shaped. This pole is frequently used in construction areas to affix traffic signs.

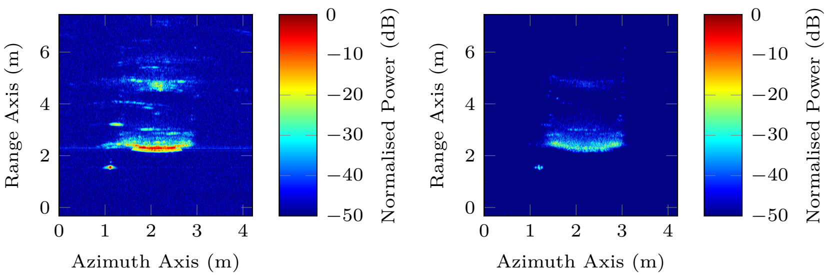

(a) Co-polarised image (HH). **(b)** Cross-polarised image (HV).

Fig. 7.7: PolSAR images of the rear view of car scenario from Fig. 7.6a.

The processed SAR images of the scenario from Fig. 7.6a are shown in Fig. 7.7. It is immediately clear from looking at the images, that level of erratic reflections has dropped significantly. This is since the measurement was carried out outdoors with very few objects lying around and no walls to reflect stray waves back towards the radar. This has a direct influence on the signal to noise level, as it increased to 20 dB for the co-polarised channel while for the cross-polarised channel it increased to 22 dB. This is explained by the fact that the clutter level in the co-polarised channel has been reduced dramatically since there are no more random objects present in the target scenery. The change in the cross-polarised channel is smaller as this channel was not affected by the presence of clutter as it was not depolarising. These figures remain consistent for all of the measurements carried out outdoors and presented in the rest of the chapter.

The metallic pole exhibits a strong response in both the co and cross-polarised returns. This is due to the irregular shape of the pole where it has both a flat surface (strong polarising target) as well as surfaces which are sharply curved creating a strong depolarising target.

Compared to the image in Fig. 7.5a, the far end of the car is not visible in Fig. 7.7a. This can be explained by the fact that the measurement setup shown in Fig. 7.6a had a ground surface consisting of asphalt whereas the surface for the setup from Fig. 7.4 is cement. The cement floor is much smoother than asphalt, hence the waves can easily bounce between the underside of the car and ground and be directed back towards the radar. With asphalt on the other hand though, the waves are scattered randomly by the rough nature of the surface and only a very small proportion of the energy is directed back towards the radar.

Considering the cross-polarised image shown in Fig. 7.7b, the sides of the car can be clearly made out. This is particularly helpful for contour estimation as will be seen with following measurement scenarios later. Comparing the co and cross-polarised SAR images, it is seen that the part of the car bumper which reflects strongest in the co-polarised channel differs from that in the cross-polarised channel. The majority of the reflected energy in the cross-polarised image results from diffuse scattering. This is possible to see since the reflected energy is not constant over the distance, rather there are peaks and troughs. In the co-polarised channel, the strongest reflection is from specular reflection as the reflected energy is relatively constant along the narrow azimuth region. Specular reflection occurs from smooth and regular surfaces whereas the diffuse scattering happens when the reflecting surface is rough and irregular [98]. Therefore one can conclude that the strongest reflection in the cross-polarised channel stems from irregularly shaped metallic body next to a regularly shaped part with the strongest reflection in the co-polarised channel.

Hence one is able to glean more information about the car by studying both the co and cross-polarised channels instead of just the co-polarised channel.

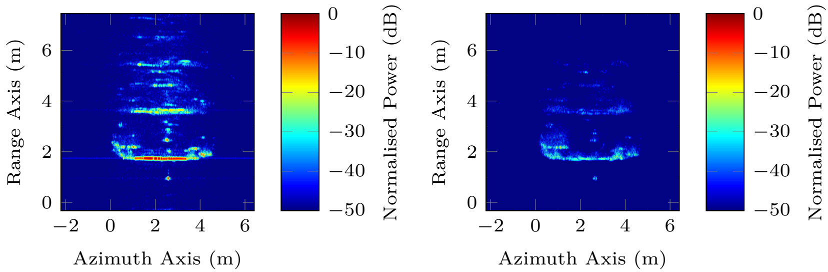

(a) Co-polarised image (HH). **(b)** Cross-polarised image (HV).

Fig. 7.8: PolSAR images of the side view of car scenario from Fig. 7.6b.

For the second outdoor measurement from Fig. 7.6b the car was parked parallel to the SAR trajectory vector and the metallic pole from the previous measurement was placed in front. The processed SAR images corresponding to this setup are shown in Fig. 7.8.

Looking at Fig. 7.8a, it is possible to see that the sides of the car are metal walls which reflect incident waves strongly without depolarisation. Hence the corresponding locations in the co-polarised image shows strong reflection while the same locations in the cross-polarised image (Fig. 7.8b) show relatively weaker reflections.

However, there are significant returns in the cross-polarised channel from the underside of the car. Looking at Fig. 7.8b closely, one can see that there are stronger returns from the left side of the car. This is explained by the fact that the parked car has the front end on the left, where the engine is placed. The underside of the engine consists of many curved surfaces in the form of tubes and containers. These are all depolarising targets which cause stronger returns in the cross-polarised channel. This makes it possible to infer the orientation of the parked cars. However, this may not be successful for newer cars whose engine room is sealed off, thereby not exposing the underside of the engine where the curved surfaces mentioned earlier are to be found. This would then reduce the amount of cross-polarised waves received by the radar.

Additionally the wheel housings of the car are also strongly depolarising targets as can be seen from Fig. 7.8b. The depolarising evident here is similar to the volume scattering prevalent in aerospace PolSAR, where the waves are incident on forest canopies where they are reflected between the branches and individual leaves multiple times before being reflected back towards the radar, thereby losing their original polarisation. In the present case however, the incident waves are not reflected between branches, rather from the enclosing, curved surfaces of the wheel housing. This is an important feature of wave scattering which can be used to gain an advantage in recognising the different regions of the car. An analysis of the cross-polarised channel can make the task of orientation estimation and even target classification much easier.

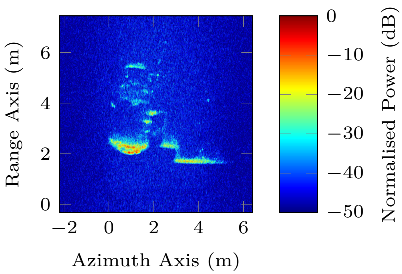

(a) Co-polarised image (HH).

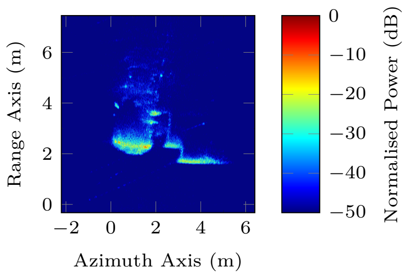

(b) Cross-polarised image (HV).

Fig. 7.9: PolSAR images of the front view of car with a bush from Fig. 7.6c.

The processed co and cross-polarised SAR images of the next measurement scenario from Fig. 7.6c are depicted in Fig. 7.9. In this scenario, the same car has been parked next to a bush which has a step in its profile. This step is difficult to make out in the camera picture, however it is easy to see in the processed SAR images. The bush is clearly visible in both the co and cross-polarised images, where it provides the volume scattering component to the cross-polarised channel. The penetration depth of the waves is however not so great at 77 GHz.

The car has been parked at a slanted angle deliberately to asses the ability of PolSAR to simplify contour estimation of parked cars. This is an important metric which has to be assessed while examining the feasibility of PolSAR for automotive applications, since the car is parked slanted and hence, most of the incident radiation would be deflected away by the large metal walls (sides of car) thereby rendering the task of contour estimation, on the basis of a co-polarised channel only, nearly impossible.

Looking closely at the cross-polarised image in Fig. 7.9b, one can see that the side of the parked car which is facing the bush is visible and an outline of the car can easily be made out. This is in spite of the fact that the bush is blocking the radar sensor from 'seeing' most of the car. The side of the car facing away from the bush is not as well resolved, since the SAR trajectory was such that it started just opposite the far side of the car and continued away to the right towards the bush, thereby the side of the car facing away from the bush received very little radar exposure.

The side view mirrors of the car can also be clearly made out since their curved surface is a strong depolarising target. To consolidate the observations derived from the measurement shown in Fig. 7.6c, the measurement was repeated with the same car parked this time without a bush and the front of the car was imaged. The SAR images from this measurement are illustrated in Fig. 7.10.

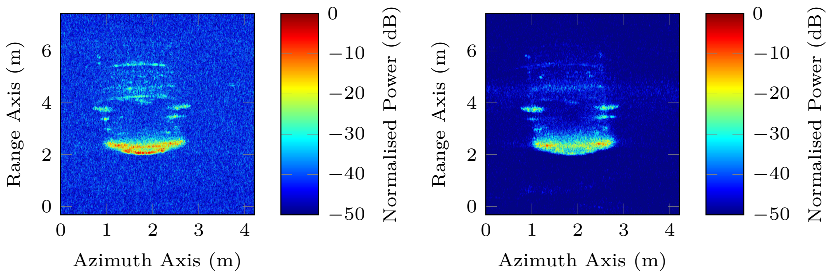

(a) Co-polarised image (HH).

(b) Cross-polarised image (HV).

Fig. 7.10: PolSAR images of the front view of car with the bush now absent.

Comparing the co-polarised image in Fig. 7.10a with the cross-polarised image in Fig. 7.10b, one can easily see that the contour of the car can be traced from the cross-polarised image. If one only had the co-polarised channel, the task of contour estimation would not be impossible but significantly more challenging as there is very little co-polarised radar returns from the sides of the car. This can be explained by considering the curvature and angular orientation of the car sides. Thus, the shape outline of the car can be readily ascertained from the cross-polarised channel. This is a salient feature of automotive PolSAR which can be put to good use in urban automotive scenarios where cars can often be found parked slanted at an angle on the street.

Additionally, comparing the two sets of the cross-polarised images (Figs. 7.9b and 7.10b) with the co-polarised images (Figs. 7.9a and 7.10a) of the front of the car, it can be seen that the regions of the car which have stronger co-polarised returns are different from those which have stronger cross-polarised returns. These regions are also consistent between the two measurements. This is a further testament to the potential of new information which can be gleaned by the use of automotive PolSAR.

7.3.1 Cross-Polarised Power Ratio

Thus far the processed SAR images were presented as a visual result. This fulfils the need for human understanding, however in order to evaluate the behaviour of the co and cross-polarised channels in an automated manner (that is programmatically by a script), a quantitative measure is required. This can be achieved by calculating the cross-polarised power ratio ($\mathrm{PR_X}$) defined as $\mathrm{PR_X} = \frac{\mathrm{P_{HV}}}{\mathrm{P_{HH}}}$ [32]. This ratio provides a contrast between the cross ($\mathrm{P_{HV}}$) and co-polarised power ($\mathrm{P_{HH}}$). This ratio can also be displayed in the form of an image, where it would be possible to judge from a single glance which regions of the image are dominated by specular reflection and which are depolarising in nature. These images will be discussed shortly. Perhaps an even more important application of the ratio, though, is to enable automation through an algorithm which can detect regions of interest.

For comparison, the cross-polarised power ratio ($\mathrm{PR_X}$) image of the first measurement, carried out inside the garage is illustrated in Fig. 7.11. From this one $\mathrm{PR_X}$, it is possible to gain the same information as from the two co and cross-polarised images shown in Fig. 7.5. Regions of the car which dominate the co-polarised channel have been mapped to the black colour which indicates a trough (low ratio). They are also encircled in red to make it easier to spot them. The depolarising regions of the car are on the other hand amplified. Thus, it

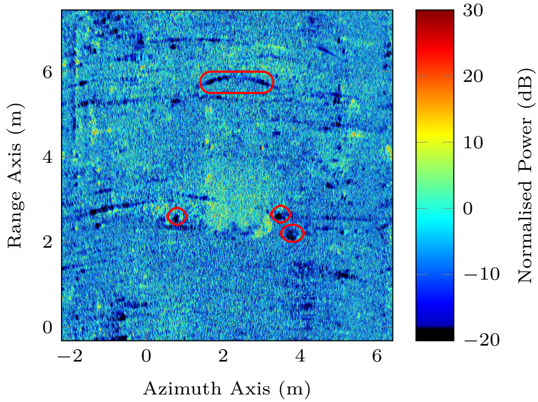

Fig. 7.11: Cross to co-polarised power ratio (PR_X) image of the measurement scenario from Fig. 7.4. Image taken from [97].

is relatively easy to identify the different sections of the car, depending on whether they cause specular reflection or depolarisation of the incident waves.

The calibrating metal plate, metal cylinder and the guide post made of dielectric material are all clearly observable. As discussed they cause specular reflection, hence they are coloured in black. The far end of the car is also a specular reflector, thus it is coloured black. The underside of the car presents depolarising targets in the form of various tubes and curved surfaces, due to which they are coloured green and yellow. The clutter present in the garage are a mix of co and cross-polarised targets.

The PR_X image of the side view of the car (Fig. 7.6b) is displayed in Fig. 7.12. The sides of the car are as seen previously strong specular reflectors. The wheel and wheel housing can also be made out, since they cause significant depolarisation of incident waves. Additionally, as discussed it can be inferred that the front of the car is to the left in the image, since the engine assembly is a strong depolariser.

The irregularly shaped metallic pole has a rather unusual response, where the left side is a strong specular reflector since it has a flat surface oriented towards the radar. The right side of the pole, though is a depolarising target

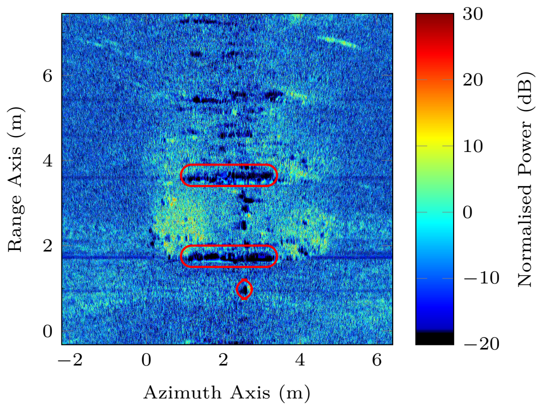

Fig. 7.12: Cross to co-polarised power ratio (PR_X) image of the side view of car with a metallic pole from Fig. 7.6b. Image taken from [97].

since it is strongly curved with edges. Although it was possible to ascertain this from the co and cross-polarised images, this effect is made visible appropriately in the PR_X image simultaneously in one image.

Figure 7.13 shows the PR_X image of the front view of the car and the bush from Fig. 7.6c. The only part of the car which has an overwhelmingly co-polarised response is the front bumper. The rest of the car has either mixed reflections or is dominated by cross-polarised power.

The contour estimation property of the cross-polarised channel deserve to be repeated here as even with the bush blocking the view of the side of the car, the outline of the car is very clearly highlighted. This observation is reinforced by orders of magnitude when Fig. 7.14 is considered. Here the outline of the car is immediately visible from the outset. Even though the right side of the car (left side in the image) received less exposure by the radar, the side of the car is very prominent, enough to make contour estimation a rather elementary task.

Also, as was discussed, the side view mirrors of the car are strongly depolarising targets since they are coloured red. The combination of these properties makes the task of contour estimation much simpler.

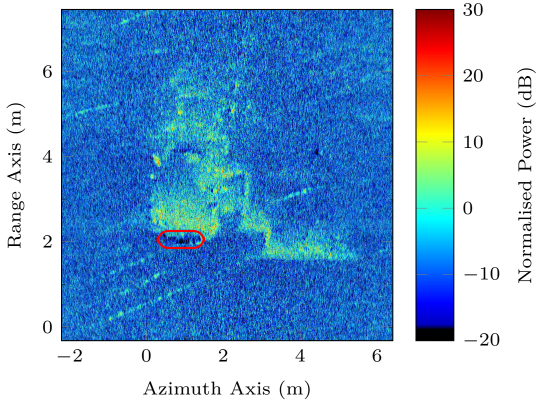

Fig. 7.13: Cross to co-polarised power ratio (PR_X) image of the front of the car and a bush scenario from Fig. 7.6c. Image taken from [97].

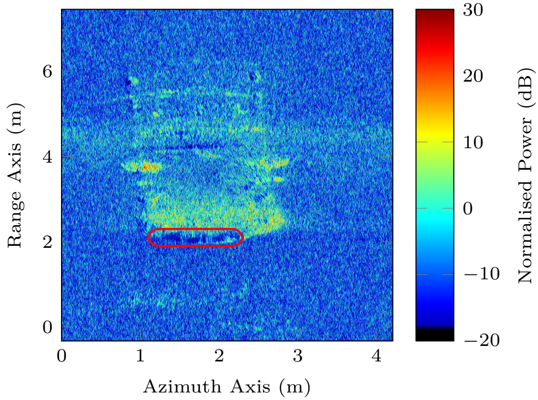

Fig. 7.14: Cross to co-polarised power ratio (PR_X) image of the front of the car without a bush. Image taken from [97].

7.3.2 Note on Orientation Estimation

It has been shown that using the cross-polarised SAR images, the contour of cars can easily be made out. This is especially true for images displaying the cross-polarised power ratio as the differences between the co and cross-polarised channels are magnified.

Once the contour of the car is available, it is possible to train an artificial intelligence based algorithm which can infer the orientation of the car. Indeed similar approaches have been reported in literature for imaging automotive radars [99–101]. Here deep and convolutional neural networks are trained to recognise targets from radar images.

Though the images used were not SAR images, they are very similar to SAR images and therefore it should be possible to train similar networks on the PolSAR images.

7.4 Concluding Remarks

Polarimetric synthetic aperture radar (PolSAR) as has been shown over the previous pages, has a lot to offer whether in the scope of driver assistance systems or autonomous driving. The task of first detecting stationary targets, then subsequently classify them and finally to arrive at the correct behaviour for the specific target is challenging for a radar. This task is made significantly easier with PolSAR, since the task of contour estimation is made simple.

The results presented in this chapter are best suited as inputs to a neural network for target classification which can also predict the orientation of the car based on its contour pattern delivered by PolSAR. These results can then be passed upto driving functions which are responsible for trajectory planning and decision making for autonomous platforms.

Additionally, PolSAR will make self-localisation for autonomous cars or cars with highly automated driving functions more meaningful since the amount of information that can be piped into an occupancy grid is much higher. The occupancy grids make unaided mobility for automated cars (robots) possible [102] [103].

8 Polarimetric Clutter Analysis for Automotive Applications

From the humble beginnings of radars less than a century ago [104–106], radars today have a plethora of applications and they are no longer used to only detect the presence of targets, rather also to estimate the structure, orientation and material properties of the targets [24]. In order to be able to carry out these tasks, modern radars exploit the properties of differently polarised waves to extract more information about targets. Polarimetric radars have available double the amount of channels when compared to mono or half polarimetric radars which naturally results in the latter type of radars delivering only half the ‘picture’ of a scenario.

It is exactly this other half of the information delivered by the fully polarimetric radar which is needed for an analysis of clutter relevant for automotive radar applications. As a background to this study, consider the accident statistics available, an excerpt of which are presented here: according to the U.S. Department of Transportation, more than 1,300 people are killed and at least 116,800 people are injured annually in traffic accidents in the U.S. on snowy and icy roads [107]. The corresponding figures for Germany are 41 deaths and 6,241 people injured in traffic accidents in icy winter driving conditions [108]. These figures underline the importance of an investigation into the effects of clutter and how they could be used to extract information about the driving surface.

Having studied the benefits available from a polarimetric radar for high resolution imaging of typical automotive scenarios in Chapter 7, the subsequent step is to build on the experience gained from polarimetry. The next task is to investigate whether a polarimetric radar can also deliver information about the ambient conditions by making use of clutter or backscatter provided by the driving surface. Before a thorough handling of clutter analysis can be undertaken, it is necessary to first consider what clutter refers to in this situation.

Afterwards, clutter and its defining characteristics will be dealt with. Finally, once the terminology and conventions have been clarified, the research into clutter for automotive radars can begin in earnest.

The basics of wave polarisation and how to deal with it were discussed in just enough detail for the scope of this work in Chapter 3. For further details, it is advisable to brush up on the concepts from the literature cited in Chapter 3.

8.1 Clutter in Context of Automotive Radar

The word clutter in radar terminology is used to refer to radar returns that result from objects not normally considered targets, as in, they are not of interest. Examples of clutter for an aircraft radar could be returns from the ground, sea, weather phenomena such as rain and snow or other fast moving objects which may not always be recognised as clutter [109, 110].

These clutter creating objects make the task of the radar operator difficult since they 'clutter' the radar display screen which serves to disguise the actual target among other objects which are not of interest. This also increases the noise level and in case of large clutter, the actual target may actually be masked by the large return from clutter.

For an automotive radar, even though the concept is similar, the objects usually considered as clutter are much different. In this case, radar returns from trees and other vegetation next to the road, falling rain and snow as well as reflections from the road surface being driven on itself. Depending on the application though, some of the objects described as clutter here may actually be targets of interest. So is the case here, in this chapter the radar returns from the road surface are analysed and presented. Hence, unless explicitly specified otherwise, throughout this chapter, the word clutter is used to denote radar returns from the **road surface**.

8.2 Why is Clutter Analysis Needed?

The objective of this study is to understand the behaviour of clutter from the road surface and with the help of this knowledge use the clutter information to gain more information about the structure of the driving surface. This information will enable the autonomous car or the driver to make much more accurate judgements with respect to the prevalent driving conditions. This is crucial information which can help in reducing driving accidents.

An extremely important advantage offered by the radar is that this information is available before the car reaches the point of danger, since the long range radar (LRR) looking in the driving direction would be used for this implementation.

8.2.1 Previous Research and Objectives

A study of clutter seen by automotive radar has been reported and analysed in driving conditions at different ego speeds [111]. The radar sensors used were short range radars (SRRs) which were positioned for blind spot detections and warning.

The theoretical basis for such applications has been provided [112], where the dielectric constant of asphalt has been measured and then models developed which can predict the behaviour of the differently polarised waves with snow and ice covered road surfaces at 94 GHz as a function of changing incidence angle. These models were also validated with measurements which were found to be in agreement with the models [112].

It has also been shown that it is possible to differentiate such road surfaces at 24 GHz based on their backscattering coefficients ($\frac{\sigma_{\mathrm{VV}}}{\sigma_{\mathrm{HH}}}$), since the change in the dielectric properties of the varying road surface affects the horizontally and vertically polarised waves differently [113–115].

All of these contributions, though very illuminating, are limited in scope for the foremost reason that they are not in the frequency band of interest: 77 GHz. The behaviour reported at 94 GHz though still relevant at 77GHz, is not sufficient to base future automotive radar applications on. Particularly because the reported measurements have not been carried out on normal public roads, rather on isolated test tracks. Additionally, the 24 GHz band has been made available only temporarily and will be phased out eventually [116].

Therefore the goals for the work presented here can be defined as,

1. to investigate under controlled conditions whether a wet asphalt behaves differently than a dry one, when different linearly polarised waves are incident upon it,

2. to find out if wet, snowy and dry asphalt can be discriminated against in realistic conditions on public roads
3. and to also ascertain whether different driving surfaces (asphalt and cobblestone) can be distinguished based on their backscattering properties

using solely a polarimetric radar sensor operating in the 77 GHz frequency range.

This chapter is divided into two broad parts, in the first part (Section 8.3) results from a measurement campaign using a linear rail unit are shown and discussed. This illustrates the initial phase of the research where a feasibility analysis was carried out to gauge whether it makes sense to investigate clutter from the road surface using polarimetry.

The second part (Section 8.4) builds on the knowledge gained from the previous part and takes clutter analysis further, where a polarimetric radar was fixed to a car and clutter measurements carried out in different weather conditions. The measurement setup is described in detail before the measurements results are presented and discussed.

8.3 Linear Rail Based Polarimetry Measurements

8.3.1 Sensor Details

In the first step towards gathering measurements results, a fully polarimetric radar sensor was placed on a linear rail unit which can be programmed to move precisely the desired distance with the help of a stepper motor as described in Section 6.2.1.

Tab. 8.1: Radar parameters

Parameter	**Quantity**
Centre frequency	76.5 GHz
Bandwidth	1 GHz
Sampling frequency	10 MHz
Ramp length	128 Samples

The parameters of the radar sensor used are summarised in Table 8.1. The used bandwidth of 1 GHz is not yet used by most automotive radars, however the frequency band has been made available for use and it is expected that radar sensors in the future will very well use the higher allowed bandwidth [117].

(a) Image of used polarimetric automotive radar sensor.

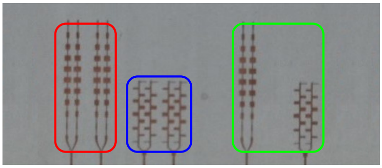

(b) Antennae layout. Red: two vertically polarised receive antennae,
blue: two horizontally polarised receive antennae,
green: two transmit antennae.

Fig. 8.1: The fully polarimetric radar sensor and its antennae layout, used for measurements.

Camera images of the used sensor and its antennae layout can be seen in Fig. 8.1. The sensor assembly and radome are displayed in Fig. 8.1a. Although this sensor is much too large to be used for commercial automotive applications, the antennae and housing set it apart from research prototypes normally seen in the universities. Thus for research purposes it is considered as relatively close to an automotive sensor.

The antennae layout is shown in Fig.8.1b, where the antennae encircled in red are the two vertically polarised receive antennae, blue encircled are the two horizontally polarised receive antennae and in green are the two transmit antennae, one of each linear polarisation. Thus the sensor offers eight channels effectively.

The measured azimuth antennae pattern are displayed in Fig. 8.2 while the elevation patterns are displayed in Fig. 8.3. Since the antennae do not have any tapering in the azimuth direction, the beam is quite broad. However, for the measurements carried out here, the wide beam is helpful, since the target is visible even at oblique angles. This will be discussed in the next sub-section.

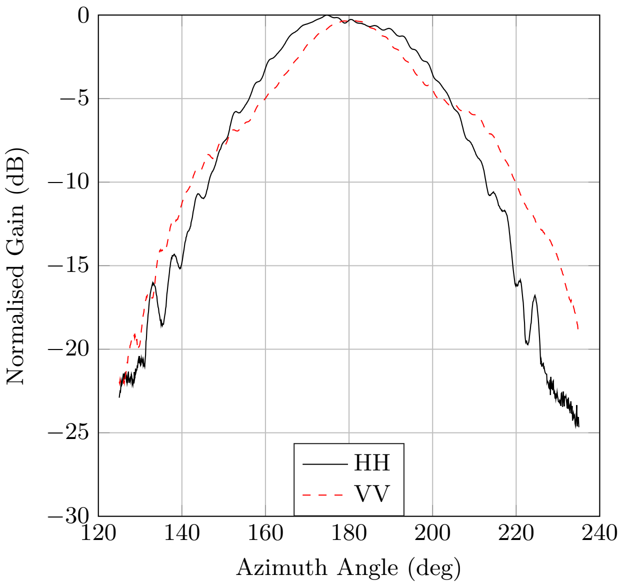

Fig. 8.2: Measured beam patterns of the radar sensor.

The relatively wide tapering of the antennae in the elevation direction ensures that the beam is narrow as seen in Fig. 8.3. This assures that the distance at which the beam touches the ground is sufficiently ahead of the sensor, when it is placed at a height typical of automotive scenarios. The elevation beam pattern for the VV channel is narrower than that of HH since the vertically polarised antennae in Fig. 8.1b have more pronounced tapering than the horizontally polarised antennae. The resulting small difference in the beam-widths is however not significant enough to spawn errors in the measurements and is therefore neglected.

8.3.2 Measurement Scenario

The schematic of the measurement setup is depicted in Fig. 8.4. The rail unit was placed slanted such that the ends of the rail unit are identified by **A** and

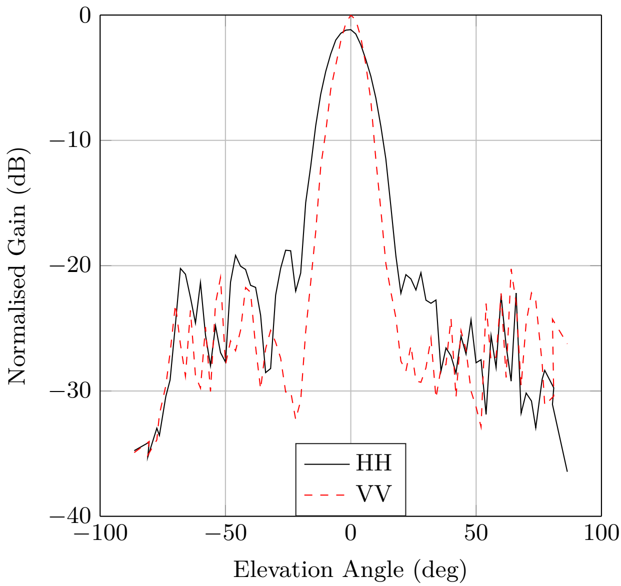

Fig. 8.3: Measured beam patterns of the radar sensor.

B. The length of the rail unit is identified as c. The target, a corner reflector, was placed at point **C**.

The radar start position was at **B** and with each step the radar moved along the side c towards point **A**. This is shown by the arrow and the dotted lines corresponding to the points $\mathbf{B}_1$, $\mathbf{B}_2$ and $\mathbf{B}_n$. The measurement set-up was designed such that, with each step the range, a_n, from the radar sensor to the target (corner reflector) decreased by approximately 3 cm. The script controlling the rail unit and the radar sensor was able to calculate, from the lengths a, b and c, the step size required to achieve a difference in range of 3 cm with each step.

The radar traversed along the length c until the dotted line corresponding to $\mathbf{B}_n$ made a right angle (90°) with side c. After this point the range to target, a_n, would increase with every subsequent step. Hence the measurement was

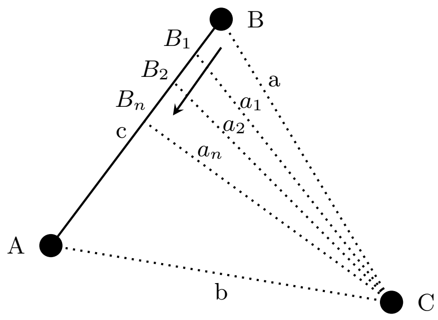

Fig. 8.4: Schematic explaining measurement setup.

stopped at this point. The advantage of having a wide beam-width antenna becomes clear here as the target at **C** was visible even when it was not at the bore-sight of the sensor, rather at an oblique angle.

Fig. 8.5: Set-up for multipath polarimetric measurements under dry and wet conditions.

The measurement set-up is illustrated in Fig. 8.5, where the rail unit with the sensor from Fig. 8.1a fixed on top as well as the corner reflector can be seen. The measurements were carried out on an asphalt surface close to the university where the rail unit could easily be deployed.

First, the measurements were carried out over dry asphalt before the surface was sprayed with water from a garden hose. The measurements were then repeated over wet asphalt. It is important to mention that the asphalt surface had to be completely submerged in water in order to affect a difference in the behaviour of the polarised incident waves.

8.3.3 Measurement Results

A representative result of the measurements carried out, as described in the previous sub-section, is displayed in Fig. 8.6. The received power level in Fig. 8.6 is considerably higher at short ranges and drops off at long ranges. This is signal fading through multi-path propagation, which is a well known effect in wireless communication [118]. Another aspect which can be plainly seen in the measurement are the troughs and peaks for both HH and VV. In Fig. 8.6 the received power of both co-polarised channels in certain places experiences sharp drops of up to 12 dB. The sharp peaks and troughs under wet conditions occur due to the fact that the asphalt surface is covered by a film of water which submerges the multi-faceted stones and rocks comprising the road surface. This converts the initially very rough surface to a much smoother one. The incident radiation is thus reflected (forwards mostly) instead of being scattered by the rough surface in random directions under dry conditions.

Upon taking a closer look at the plot of the received power in Fig. 8.6, one can notice that the peaks exhibited by HH are generally higher and the troughs lower than those of VV. This phenomenon can be confirmed by the differing coefficients of reflection for both VV and HH as shown in Fig 3.2. The sharp troughs exhibited by HH, are evidence that under wet conditions, the power reflected from the ground is greater which causes greater interference at the target. This effect can be described as mirroring by the wet ground.

Now that the multi-path effects have been examined in detail, in the next section, more time will be spent analysing the behaviour of clutter.

8.3.4 Clutter Analysis

To analyse the behaviour of clutter from the asphalt surface in the previous section, the data was processed again, this time with the intention of gaining insights into clutter.

Figure 8.7 depicts firstly what is meant by clutter and secondly how it is extracted from the data acquired from the measurement campaign described in Section 8.3.2. The figure shows a sensor transmitting two rays towards a

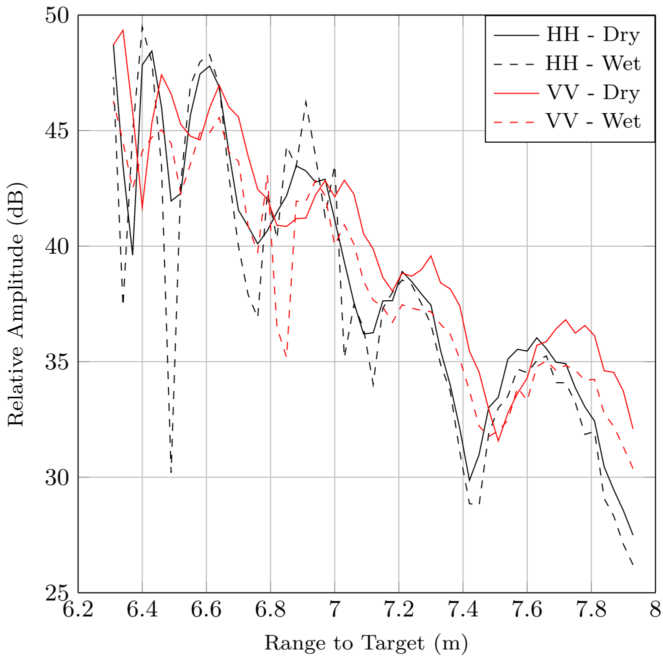

Fig. 8.6: Measured normalised receive power under multipath propagations on dry and wet asphalt.

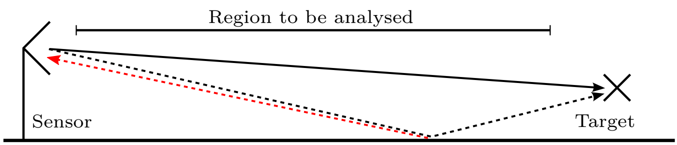

Fig. 8.7: Measurement schematic for clutter analysis with radar sensor on a linear rail.

target some distance away. One of the rays travels a direct path from the sensor to the target while the other ray reflects off the surface and is incident on the target. However, not all the energy represented by the ray interacting with the ground is reflected forward towards the target. A portion of the incident energy is reflected back towards the sensor. This is represented by the red dotted line.

This is the reflected energy which is referred to by clutter in the scope of this chapter. The energy thus reflected from the ground is a function of material, shape and size of the reflecting surface. Thus by examining the differences in clutter between the vertically and horizontally polarised channels, one can make inferences regarding the structure of the reflecting surface, that is the ground.

To proceed, the clutter specific data had to be isolated from the rest of the signal. At the start of the measurement, the range from the sensor to the target was recorded. Therefore, using this information coupled with the known step sizes of the rail unit platform, it is possible to ascertain coarsely the range to the target from every point. A CFAR (constant false alarm rate [119] [120]) peak detection algorithm was then used to accurately locate the peak corresponding to the target. This would then be cut out and everything contained in the signal before this target is clutter information from the ground surface.

As the elevation beam-pattern of the antennae are known, it is hence possible to calculate at which range the beam would first touch the ground surface. All the signal data starting from this point until the point in range where the target information was snipped out are essentially clutter returns from the ground surface. Hence, the extent of the region with clutter returns are thus known and the evaluation of clutter can therefore be carried out.

The complete results with the received power profile over range and clutter information is illustrated in Fig. 8.8 for the vertically polarised channel. The amplitude profile plotted on the top is the received power over the range as shown in Fig. 8.6. This serves to show the fluctuations in power due to fading as discussed in the previous section. The plot on the bottom shows the average clutter for both dry and wet conditions. The average clutter power differs in certain places, however, there is no significant difference evident, based on which it would be possible to recognise any trends portraying a pattern of clutter power under wet conditions.

The plot in the middle depicts the behaviour of 90^{th} percentile of the clutter power. The 90^{th} percentile is significant because clutter with higher amplitudes can offer some information which may be lost if only the average clutter

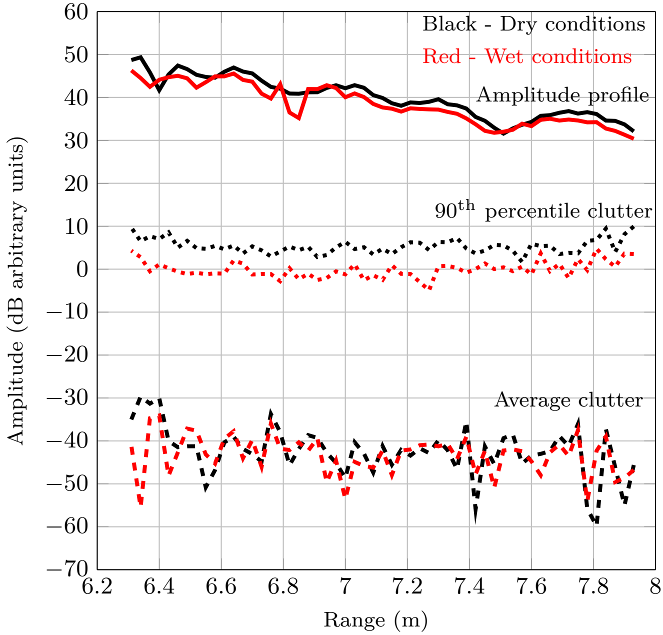

Fig. 8.8: Observed clutter in the VV channel on an asphalt surface under dry and wet conditions.

amplitudes are considered. Here, a clear pattern can be seen, in that the 90$^{\text{th}}$ percentile of clutter is consistently on average approximately 3 dB lower under wet conditions than dry conditions.

This behaviour is prevalent for the horizontally polarised waves too as can be deemed by considering Fig. 8.9. In essence, this behaviour implies that the average clutter power remains more or less constant, however the 90$^{\text{th}}$ percentile drops by a few decibels when the road surface is covered by water.

Considering Fig. 8.6 again, it was seen that under wet conditions the received power for both the horizontally and vertically polarised channels witnessed more frequent troughs and peaks. As discussed, this behaviour is due to the mirroring effect which occurs as the film of water on the asphalt surface serves

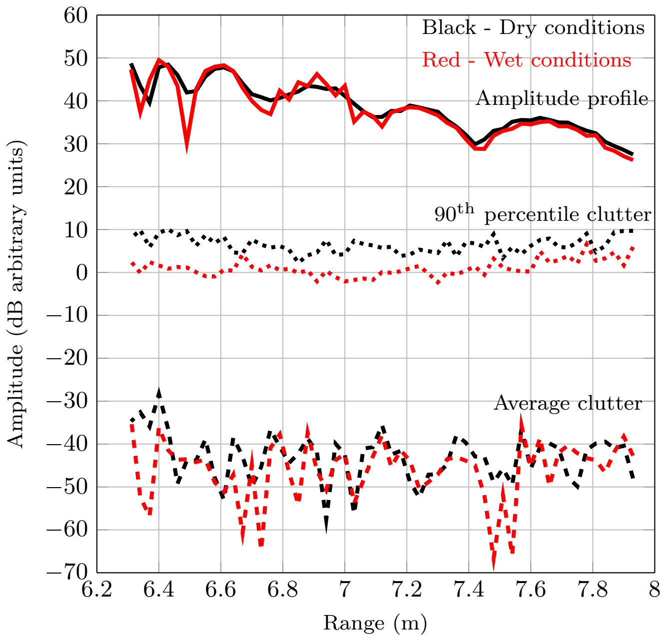

Fig. 8.9: Observed clutter in the HH channel on an asphalt surface under dry and wet conditions.

to make the rough surface smoother by covering up the facets on the ground. It stands to reason then that when the received power from the target experiences troughs and peaks under wet conditions, there must be more power being reflected from the ground and arriving at the target via the indirect path. This is precisely what the lower 90^{th} percentile value for wet asphalt demonstrates.

8.4 Polarimetric Clutter Measurements Using a Radar Test Vehicle

Now that it has been shown, on the previous pages (Section 8.3.4), using a rudimentary set-up that there is indeed new information to be gleaned from a polarimetric clutter analysis, it makes sense to design a measurement set-up that is robust enough to be used to acquire radar measurements in real and not simulated driving conditions.

The objective for this section is to examine the polarimetric clutter behaviour on normal public roads under varying driving conditions (wet and snowy) and compare the clutter to that under dry conditions. From this data, the goal is to be able to ascertain the condition of the road based solely on the polarimetric radar measurements. It was also desirable to be able to carry out measurements on roads under icy conditions, however it is exceedingly difficult to find such conditions near Ulm since the municipal services do their utmost best to minimise such conditions due to the obvious risk of traffic accidents.

An additional goal is to investigate the clutter for different road surfaces as well (cobblestone and asphalt).

8.4.1 Measurement Setup

Fig. 8.10: Designed lens to reduce azimuth beam-width.

The sensor used for these measurements was the same as described in Section 8.3.1. Table 8.2 lists the parameters pertinent to the measurements carried out in this section.

The first order of business was to consider the azimuth beam patterns of the sensor. The current azimuth half-power beam-width of 45° was much too broad. This would result in unwanted reflections from the kerbstone and other objects on the side of the street which would pollute the reflected signal, since the radar returns from these objects would be mixed with the returns from the street surface and it would be impossible to separate them.

Additionally, a broader beam would result in lower range since the transmitted power would be spread over a greater angular region. This would be counterproductive for the planned measurements since for this case, more power needs to be focussed onto the road surface in front of the car. Keeping these two reasons in mind, it was decided to design an integrated lens for the sensor which would focus the beam in the azimuth plane.

The biggest challenge for designing the lens was the requirement that the lens fit onto the sensor creating a waterproof seal which is important considering the measurement campaign that needs to be carried out. The thus designed lens is illustrated in Fig. 8.10. The two parallel vertical protruding bulges are the focussing surfaces (lenses). They are positioned directly above the two transmit antennae, one each for the vertically and horizontally polarised waves. It was not possible to place lenses over the receiving antennae, as there was not enough physical space to fit four lenses next to each other as can be seen from Fig. 8.1b.

The placement of the two lenses over the transmit antennae however was enough to reduce the beam-width as can be seen from Fig. 8.11. The half-power beam-width has been reduced to 25° thus ensuring that the beam is focused on the road surface in front of the car and therefore the clutter is mostly due to the backscatter from the road surface and not from formations or objects on the side of the road like a footpath or traffic signs.

Since in this measurement campaign the radar measurements need to be carried out while the car is moving, it was necessary to employ a chirp sequence. The chirps therefore had to be optimised in order that the minimum sampling requirements were met. The basics for this have been handled in Section 2.3.3. With the help of (2.13), the ramp parameters (Table 8.2) were selected such that a maximum unambiguous velocity of approximately 30 km/h was achieved.

The polarimetric radar sensor was fixed to the car such that it was centred

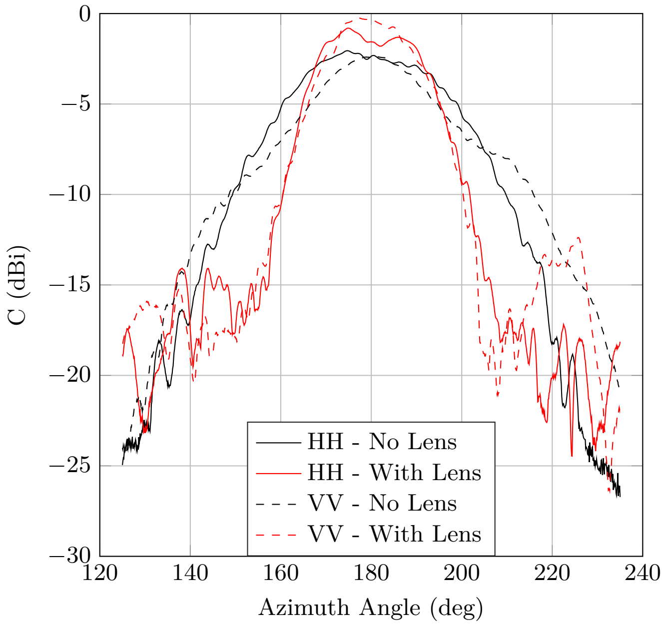

Fig. 8.11: Measured beam patterns of the polarimetric radar sensor.

with respect to the car's width, so the sensor's bore-sight direction was aligned with the centre of the car. There was no tilt angle given to the sensor, hence

Tab. 8.2: Radar parameters

Parameter	**Quantity**
Centre frequency	76.5 GHz
Bandwidth	500 MHz
Sampling frequency	10 MHz
Ramp length	128 Samples
No. of ramps	256
Ramp repetition interval	107 µs

the radar beam was pointed directly in front of the car and with the help of the antenna beam patterns, it was calculated that the beam should touch the ground at a range of approximately 4 m from the front grille of the car. This was also experimentally verified using point targets (corner reflectors) placed on the ground in front of the car and moving them until the extents of the beams were found. The radar test vehicle is shown in Fig. 8.12. The polarimetric radar sensor with its water proof housing is fixed to the roof of the car while the commercial sensor fixed behind the front grille of the car was blocked by an absorber and aluminium foil. Both of them have been encircled in red in Fig. 8.12.

Fig. 8.12: Set-up for investigation of polarimetric clutter.

8.4.2 Calibration of Measurement Setup

The next step was to remove the effects of the differing antennae gain through calibration with the help of a metal sphere. The ratio of the received and transmitted powers can be written as [24],

$$\rho_{\mathrm{ii/jj}} = \frac{P_{\mathrm{r,i/j}}}{P_{\mathrm{t,i/j}}} = \frac{{G^2}_{\mathrm{ii/jj}}\lambda^2}{(4\pi)^3\, R_{\mathrm{o}}^4}\sigma_{\mathrm{o}}, \tag{8.1}$$

where i and j represent the polarisations, $P_{\mathrm{r,i/j}}$ and $P_{\mathrm{t,i/j}}$ the received and transmitted power respectively for each polarisation, $G_{\mathrm{ii/jj}}$ the co-polarised antenna gain for the respective polarisation, R_{o} the distance to the sphere and

σ_o the radar cross-section of the sphere. The calibration value is then defined as,

$$\alpha_{\frac{jj}{ii}} = \frac{\rho_{jj}}{\rho_{ii}} = \frac{G_{jj}^2}{G_{ii}^2}, \tag{8.2}$$

which is defined as a ratio of the gains of the polarised antennae. This calibration value is then used to divide the jj polarised signal (ρ_{jj}) so that it is as if the signal has been received with an antenna of gain G_{ii}. The same procedure is carried out for the two cross-polarised signals as well.

Additionally, the electrical path lengths of the two co-polarised signals were calibrated as well such that the phase change remained the same for both, so that the coherent addition ($S_{HH} + S_{VV}$) could be carried out as well. S_{HH} and S_{VV} represent the horizontal and vertically polarised components of a scattering process which was covered in Section 3.1.

Calibration of Beam Footprint

Once the above mentioned calibration was done, the next step was to carry out a fine calibration of the antennae pattern and to select ranges for which the data should be processed. To this end, the measurement set-up was affixed to the car's roof and the car parked in an open area covered with asphalt and no objects in the line of sight of the radar except for the surface. In this calibration process, the maximum range from which the clutter from the road surface could be recognised was from 27 m. However, it is pertinent to mention that the return was very weak and would sometimes disappear depending on the local surface characteristics. For the purposes of the signal processing task at hand, the maximum range was selected to be 19 m. The starting range or the minimum range was selected to be 8 m. These ranges are from the perspective of the sensor and not of the car, that is they represent the slant range. These ranges were selected keeping in mind the height of the sensor and the elevation beam-widths. The utility of these start and stop ranges will become clear shortly once the discussion moves deeper into the signal processing steps. The calibration process was then carefully fine tuned where the car was kept stationary and with the help of a corner reflector, the extents of the HH and VV beam patterns were mapped out. The goal was to select the patch of road surface where the HH and VV exhibit approximately equally strong returns. The gain of the antennae had at this time already been calibrated (as mentioned earlier), hence the choice of the target did not skew the results. With the fine tuned calibration, it was also assured that any errors in the mechanical construction and assembly of the measurement set-up were calibrated out.

8.4.3 Signal Processing Chain

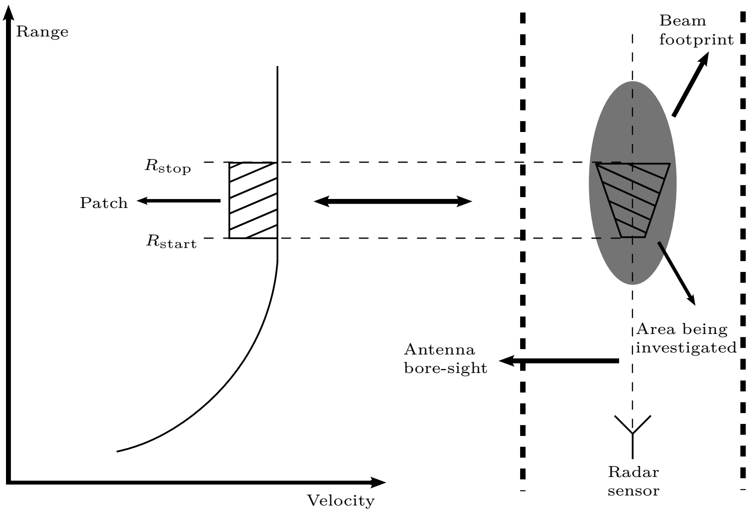

Fig. 8.13: Schematic of measurement geometry and clutter levels. On the left is the Range-Doppler (velocity) diagram and on the right is the physical interpretation of the diagram with respect to the measurement scenario.

The measurement scenario is shown in the right part of Fig. 8.13. The radar antennae were pointing in the direction of travel and thus it was receiving backscatter from the beam footprint, the extents of which were already mentioned in the previous section. The measurements were then processed to create a Range-Doppler [23] representation of the scenario. This represents the backscatter for each polarisation (HH, VV, VH and HV). The goal for the first signal processing block was to isolate the backscatter from the ground (clutter) from all other radar returns. This was done in range by setting an R_{start} and an R_{stop} point. The length of range between these two points represents the clutter values which were to be isolated and processed.

To isolate values in the velocity domain, it was decided to select clutter values from a section of the road surface whose width was 1 m either side of the antenna bore-sight. This would be enough to represent the path in front of the car. The width (Doppler/velocity) of the section of road was calculated using the fact that points lying on the bore-sight direction have the largest Doppler frequency and all points lying off bore-sight have a smaller Doppler frequency which is dependent on the offset of the said point from the bore-sight. The 1 m width of the section of road was calculated at the R_{stop} point. Hence, a patch of values were cropped out of the Range-Doppler representation as shown in Fig. 8.13 on the left side. The physical representation of this patch is shown on the right. The rectangular patch in Range-Doppler becomes a trapezium on the road since the point that is 1 m wide from the bore-sight at R_{stop} has a larger Doppler frequency than the point that is 1 m wide at R_{start}, as the offset of 1 m at R_{start} subtends a larger angle which leads to lower radial velocity and hence, lower Doppler frequency. This can be better understood by considering Fig. 8.14. Here the radar sensor is shown along with the beam cone angle. The point lying 1 m off the antenna bore-sight has a cone angle θ_{offset}. This point has a certain radial velocity which translates to a Doppler frequency which is lower than the point at R_{stop} on the bore-sight. Now the point off bore-sight at R_{start} which has the same Doppler frequency lies on the same angle, θ_{offset} but the separation from bore-sight is now lower. Hence the patch becomes a trapezium on the road surface.

Once the patches have been selected, the clutter analysis can begin. In a previous study [114], the small perturbation model ([35]) was used to study the backscatter at 24 GHz. However, this approach cannot be used at 77 GHz because the wavelength is shorter and hence the assumptions for the model, that the product of the root mean square surface roughness s, in (3.6) discussed in brief in Section 3.2.2, and the propagation constant k is small ($ks < 0.3$) do not hold [30].

Therefore, one has to rely on the parameters introduced in Section 3.3. The parameter M, from (3.11), is sensitive to the dielectric properties of the re-

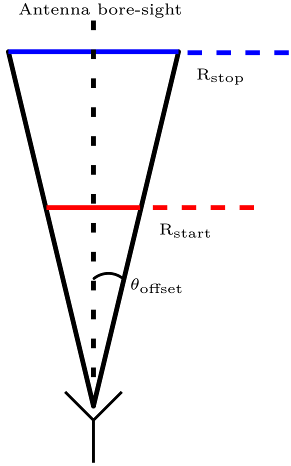

Fig. 8.14: Figure illustrating how a rectangular patch in Range-Doppler domain corresponds to a trapezium on the road surface in the physical world.

flecting material and can thus be used to detect when the driving surface may be covered with snow or water. Meanwhile, the parameter R, from (3.10), is influenced by the roughness of the reflecting surface, hence it can be used as an indicator of traction available on the surface which is an important piece of information for maintaining the stability of the car.

Recorded Roads and Conditions

Over the course of the measurement campaign for this research, well above fifty recordings were gathered for each condition over different stretches of public roads in and near the city of Ulm in Germany.

An overview of the recorded distances for each condition and surface type is given by Table 8.3. Dry asphalt has the largest amount of data as this was the condition which was the easiest to find.

Snowy conditions were not easy to predict. Though once found, it was quite easy to record large amount of data as the snow usually keeps laying on the road until it is cleared or it becomes warm and melts away. It was thus possible to drive around and acquire a lot of data in a relatively short amount of time. Here it was made sure that the amount of snow lying on the road was at least a couple of centimetres and the municipal services had not attempted to clear the roads of snow yet. Extra care was taken to record data from roads which were not very frequently driven on, as the snow lay largely untouched on such roads.

Tab. 8.3: Summary of recorded distances for each condition and surface type

Weather and Surface	**Distance Recorded (km**
Dry asphalt	23
Snowy asphalt	17
Wet asphalt	10
Dry cobblestone	11

Finding wet asphalt conditions was considerably more challenging, as a large volume of water needed to be on the road surface for there to be any significant change in the surface properties which could be detected. This was particularly challenging as thunderstorms with heavy rainfall are difficult to predict and are often short in duration. Thus the measurements were carried out during rainfall as otherwise the water would flow away. During heavy rainfall, water forms streams across or along the road where most of the water flows. It was attempted to capture as much as possible of such streams of flowing water. These conditions were difficult to satisfy most of the time, hence the amount of recorded data for wet asphalt is the least of all the categories.

The cobblestone surfaces were recorded in dry conditions in various places also in and near the city of Ulm. The reason for the relatively low number of recorded kilometres for cobblestone streets is that cobblestone is not used extensively and they are almost exclusively found in very busy city centres. Therefore recording data without the presence of other disturbing objects (pedestrians, cyclists and other cars) was a time consuming and slow process. Most of these recordings were carried out late at night or in the very early morning.

In the next section the results will be presented which have all been obtained from measurements carried out in conditions described above and summarised in Table 8.3. As the amount of recorded data for each condition varies strongly, the condition with the least number of data was chosen as the one which prescribes how many data points are taken into account for each condition. For example in comparing dry, snowy and wet asphalt, data amounting to approximately 10 km was selected from the available pool of dry and snowy conditions.

8.5 Measurement Results

To avoid confusion and misunderstandings, this Section is divided into two parts. In the first part the driving characteristics are investigated in different weather conditions while in the second, different driving surfaces are compared to asphalt. Both of the sections aim to present how the varying driving conditions can be recognised with the help of a polarimetric radar sensor. to accomplish this task, measurement data was gathered from public roads in and near Ulm. The targeted weather can be described as dry, snowy and rainy (wet asphalt) conditions.

8.5.1 Weather Influenced Surface Behaviour

In Fig. 8.15, a statistical representation of the clutter values for different conditions can be seen. Fig. 8.15 shows the trends in data for varying weather conditions. The numbers printed next to each box are median values for each condition and polarisation while the 1$^{\text{st}}$ and 99$^{\text{th}}$ percentile are given next to their respective outliers.

The data shown in the boxplot represents an unadulterated picture since no averaging has been done. Rather data from the patches corresponding to each polarisation for each condition are pooled together and plotted. It should be mentioned that the data displayed in the boxplot consist of at least one million individual FMCW chirps for each condition (dry, wet and snow).

In the initial stages of the measurement campaign, the polarimetric backscatter from different roads with asphalt surfaces were compared with each other to gauge if there are any characteristics which vary between different asphalt surfaces. The finding which was found, is that for the polarimetric sensor operating at 77 GHz, all asphalt surfaces are the same because their structure is overall very similar and compared to the wavelength of roughly 4 mm, the

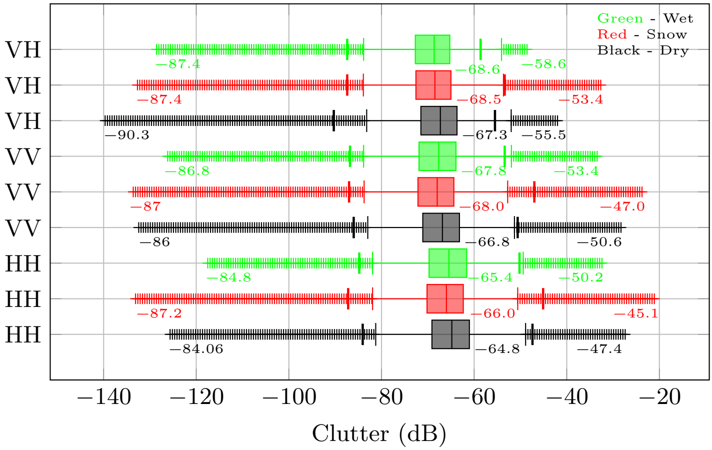

Fig. 8.15: Boxplot of clutter values from different road conditions. Median values printed next to each box and the values corresponding to the 1st and 99th percentile printed next to the respective outliers. The position of the percentiles are marked with a thick vertical line.

asphalt surface is very rough. This is in contrast to what we can see with our eyes, where different asphalt surfaces 'look' different. This key finding enables the direct comparison of different roads with dry asphalt surfaces with other roads which may be wet or covered with snow. The results are thus not limited geographically only to the roads where the test vehicle actually drove.

It can be noted from the boxplot in Fig. 8.15, that the individual medians of each polarisation channel and condition are very similar on the whole, except for HH, which is always stronger by a factor of two approximately. However, VV and VH are almost identical except for the wet case, where the cross-polarised component is weaker.

Another interesting aspect that can be seen from the plot is that the number of outliers for snowy conditions are significantly larger than those for dry conditions, while for wet conditions, they are much less than for the other two conditions. Meanwhile the medians for both snowy and wet conditions are lower than that for dry asphalt. This can be seen with the help of the 99th and

1st percentile values printed next to the respective outliers as well as the thick vertical line denoting the position of the respective high and low percentiles. As the number of outliers increases, the position of the respective percentiles moves further from the median as evident in Fig. 8.15. The increase in the quantity of outliers for snowy conditions can be explained by considering the structure of the surface. When dry, the asphalt surface has facets, whose sizes are in the order of the wavelength, hence it leads to significant depolarisation. When the surface is covered with snow, which even though it might have been disturbed by cars being driven over it, still covers the majority of the facets. This leads to a lower median since the surface is smoother and the majority of the incident waves would be reflected forward and not scattered. However dependent on the specific road conditions, the snow layer may have a structure such that has facets locally which occur sporadically, that is in certain areas the snowy surface may be rough while in most places, it may be smoother. So, while the median drops by a small margin due to the combination of the absorbing properties of snow (and snow-slush) as well as the smoother surface (due to the snow cover), the number of outliers increases due to the presence of facetted structures formed in snow by wind and the movement of other vehicles.

Similarly for wet conditions, when there is enough water on the road, it covers up the facetted structure of the road and provides a smoother surface for the incoming waves. Therefore, a greater proportion of the incident energy would be reflected forwards instead of backwards, which leads to a smaller median for wet conditions. The outliers for wet conditions, though do not increase as seen for snowy conditions since the water covers the facets of the asphalt and the water surface itself is smooth, hence there are no scattering effects from local facets.

Figure 8.16 shows the variation of M of the road surface when it is covered with snow and rainwater, while Fig. 8.17 illustrates the behaviour of R. Each data point in the figures has been calculated from clutter values acquired over approximately a 10 m section of the surface. The solid line represents the average values of the parameter for each condition. At first glance, it seems that the points corresponding to R and M for the three conditions are grouped together with a high variance, rendering discrimination between the three conditions difficult. However, having two parameters, the chances of a particular measurement of one condition being falsely recognised as that of another con-

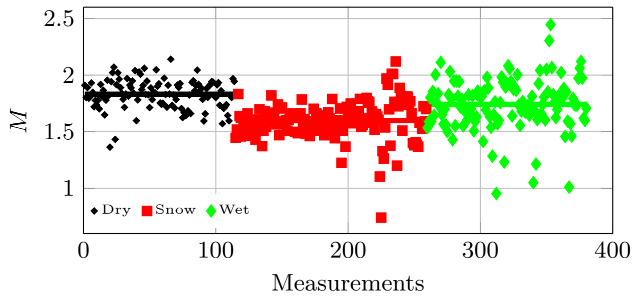

Fig. 8.16: Material (M) parameter, from (3.11), for roads under different weather conditions. Each plotted point represents clutter from a 10 m section of the surface.

dition are vastly lower when considering R and M together. This can be done by comparing the median value of each condition with the corresponding measurement point for both R and M simultaneously. This way the chances of a measurement being falsely identified are much lower.

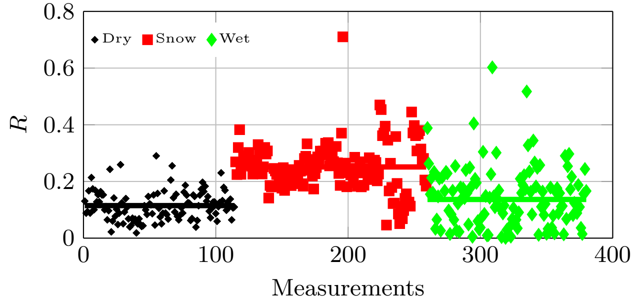

Fig. 8.17: Roughness (R) parameter, from (3.10), for roads under different weather conditions. Each plotted point represents clutter from a 10 m section of the surface.

It can be seen that there are marked differences between M for the three conditions, even though the variance for snowy and wet conditions is large.

This is due to the way the surface is covered. Water unfortunately does not lie still on the surface, rather depending on the local formations found on the road, the water might form a small stream on one side of the road while the rest of the road might be covered by much less water.

It is also important to keep in mind, that the snowy conditions do not remain constant, rather they change as the temperature during the day rises or falls and the more traffic that is prevalent on the roads. Therefore, the variance in the snow measurements will increase dramatically as the temperature increases and the snow cover gradually diminishes to lay bare the rough asphalt underneath.

Considering the fact that the clutter value from a particular resolution cell is the superposition of waves reflected from a large surface ($\approx 15\,\mathrm{cm}$ by $30\,\mathrm{cm}$), within which the road conditions might be different, the large variation in the M and R values can be understood. The variation of M and R is smaller for snowy conditions than for wet. Hence it can be deduced that a snowy road is smoother, while in wet conditions, the roughness varies strongly. However all three conditions can be recognised based on their backscatter properties, though the rate of correct prediction for wet conditions is lower.

It is important to keep in mind that, the presented signal processing algorithm is capable of detecting changes in the roughness (R) and the dielectric constant (M) of the driving surface. While the changes in the dielectric constant can give some clues with respect to snow or water covering, it is the roughness which directly affects the stability of the car and thereby the safety of the occupants of the car. Therefore, where a trained classification algorithm may fail to distinguish, for example between wet and dry asphalt, it can be argued that the degree of 'wetness' is not sufficient to cause the car to lose stability.

It was unfortunately not possible to train an artificial intelligence (AI) based detector to distinguish the conditions based on the measured clutter in the scope of this work. However, the M and R values are good inputs to such an AI detector which can be trained and then deployed for real-time in car inference of the driving conditions.

8.5.2 Effects of Different Driving Surfaces

In the second part of this work, the polarimetric backscattering properties from cobblestone roads was investigated. The measurements were carried out over cobblestone surfaces in dry conditions and compared with the received backscatter from dry asphalt surfaces. All the data thus collected are illustrated in Fig. 8.18. The numbers printed next to each box are median values for each condition and polarisation while the 1st and 99th percentile are given next to their respective outliers.

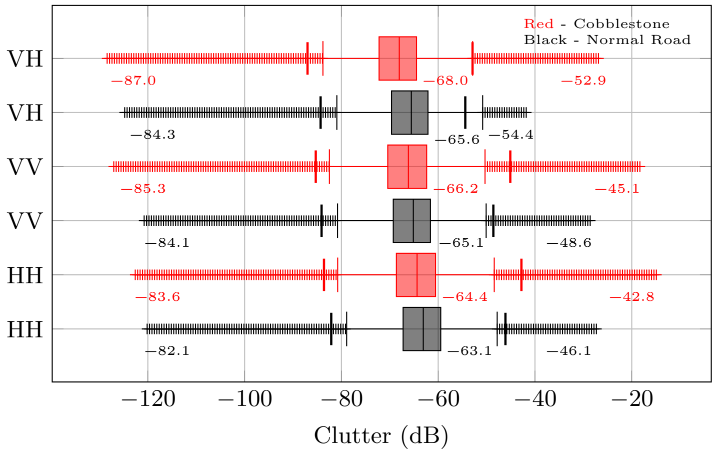

Fig. 8.18: Boxplot of clutter values from different driving surfaces. Median values printed next to each box and the values corresponding to the 1st and 99th percentile printed next to the respective outliers. The position of the percentiles are marked with a thick vertical line.

Here it can be seen that for the cobblestone road, the number of outliers increases sharply while the medians for the co-polarised channels decrease slightly and the median for the cross-polarised channel falls by roughly 3 dB. Again, the behaviour of the outliers can be identified with the help of the thick vertical lines identifying the positions of the 1st and 99th percentiles respectively. The data shown in Fig. 8.18 represents measurements obtained from more than a million individual FMCW ramps for each surface, as in the previous section.

To understand the behaviour represented in Fig. 8.18, it is necessary to consider the structure of a cobblestone surface. Cobblestones are smoother than asphalt, however they are not flat, rather they have smooth protruding curves which are in the order of or larger than the wavelength. Additionally, between the individual stones there is a small gap which forms a facet whose dimensions are also in the order of the wavelength. These features contribute to the large number of outliers. And the smoother surface results in a lower backscattered power since most of the incident power is reflected forwards, away from the radar sensor.

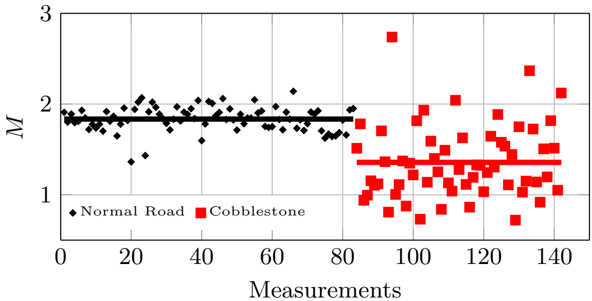

Fig. 8.19: Material (M) parameter, from (3.11), for asphalt and cobblestone roads.

Figure 8.19 displays the M parameter for the asphalt and cobblestone road surfaces, while Fig. 8.20 illustrates the parameter R. As stated in Section 8.5.1, each individual measurement point in the two figures represents the radar backscatter over a 10 m section of the respective surface. This is done to ensure that the different conditions and surfaces can be distinguished based on a short measurement history, instead of having to drive about a kilometre before the particular driving surface or condition could be classified. The effect of observing the measurements in patches of 10 m is a large rise in variance between the measurement points. Thus it is necessary to achieve discrimination of the surfaces despite the large variance.

The difference in M for the two surfaces is not very large, which could be due to the fact that both the surfaces are constructed using stones and thus the dielectric properties of both may not differ as much. However, the difference is still large enough to enable discrimination between the two surfaces.

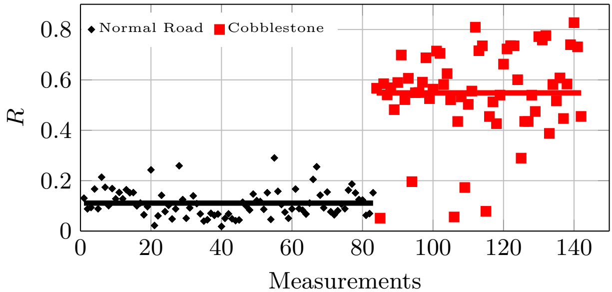

Fig. 8.20: Roughness (R) parameter, from (3.10), for asphalt and cobblestone roads.

On the other hand, the difference in R for the two surfaces is much larger and the cobblestone is decidedly much smoother than asphalt. The lower power in the cross-polarised component of the backscattered power from cobblestone in Fig. 8.18 is evidence of this. To distinguish between an asphalt surface and a cobblestone one is much easier since the change in the roughness parameter, R, is much larger than for snowy and wet conditions. Cobblestone roads are therefore much smoother than asphalt roads covered with snow or water. Since the R parameter corresponding to the two surfaces are sufficiently far apart enough, to enable easy discrimination, there was no need to carry out an analysis to determine the statistics for successful classification as done in Section 8.5.1 for dry, wet and snowy asphalt. It is thus possible to distinguish a cobblestone surface from asphalt based solely on the polarimetric backscatter as presented here.

8.6 Concluding Remarks

The data presented on the previous pages provides a good starting point for the implementation of an artificial intelligence based algorithm which can be trained to classify the surface conditions. Once this has been achieved, the relevant information about the prevalent conditions could be passed to the electronic control unit (ECU) overseeing the functioning of the electronic stability programme (ESP), so that the tire speeds could thus be adjusted and perhaps the threshold for a braking manoeuvre be lowered as well as informing the driver of the conditions.

Additionally, during the measurements phase no icy conditions were found therefore, an important improvement for the future would be to gather data from icy roads in parts of the world where such conditions can be easily found.

9 Conclusion

As it was discussed in some length in Chapter 1, the ever faster developing field of advanced driver assistance systems (ADAS) places more stress on finding novel solutions to problems which limit or dampen the functioning of ADAS and autonomous cars.

These problems were introduced and discussed in Section 1.1.1. In this chapter, a short recap of the developed solutions is given along with recommendations for possible improvements which could not be carried out in the scope of this dissertation. The importance of this body of work can be gauged from the accomplished tasks listed as follows:

- A study of the polarimetric radar cross-sections (RCS) of typical objects found in traffic scenarios everywhere. Additionally it was shown that a metal and guide post can be differentiated based on their RCS signatures.This is based solely on radar measurements and using these measurements for further signal processing.
- Adaptation of synthetic aperture radar (SAR) from satellite and aircraft based platforms to the automotive scenario to provide high resolution radar images of the automotive environment. When combined with polarimetric SAR, the outline and contours of parked cars are even easier to distinguish.
- Deployment of a polarimetric radar sensor for the analysis of road clutter and recognising different driving conditions in the presence of inclement situations and non-asphalt based driving surfaces.

Over the next few paragraphs, the above mentioned accomplishments are examined from a deeper perspective. Chapter 5 illustrates the results of the radar cross-section (RCS) measurements of various targets commonly found in traffic scenarios. The measurements were carried out with a polarimetric sensor, however it was seen that the extra polarisation channel offers little in the way of revealing hidden clues regarding RCS of traffic objects, since the horizontally and vertically polarised waves behave in a similar manner. This is likely due to the extremely large size of the objects when compared to the wavelengths of the incident waves of approximately 4 mm at 77 GHz. However, the results are nonetheless important for self localisation and compilation of grid-maps used for radar based localisation techniques.

High resolution radar images obtained through SAR are presented in Chapter 6. Here the SAR measurement schematic for automotive applications and the impetus for its deployment is introduced, before the results obtained from a linear rail unit are discussed. This represents an ideal world, where the steps are always precisely known and there are no uncertainties. It was used as a stepping stone to perfect the processing algorithms and to simulate non-ideal conditions. Finally a realistic measurement set-up is introduced in the form of a hand-pushed cart which suffers from the same pitfalls as a car, that of ubiquitous tiny accelerations as well as determining the position precisely of the radar at each instant of time when a FMCW ramp is transmitted. The high resolution radar images thus obtained were excellent for estimating the contours of parked cars.

Building on the results achieved in Chapter 6, Chapter 7 delves into polarimetric SAR. Here a polarimetry capable radar sensor is deployed to carry out measurements of the target scenarios which involved cars and other objects. Using polarimetric SAR, it has been shown in numerous literary works that the extra polarisation channels, both and co-polarised, deliver surplus information which is usually not available from a single incident wave polarisation. So too here, the use of polarimetric SAR in an automotive scenario is able to give more information which is usually locked away. This makes the task of contour estimation much simpler as well as enabling orientation estimation of parked cars. The cross-polarised channel is able to pinpoint the locations of the wheel wells as well as highlighting other places on cars which are normally not conspicuous in co-polarised channels. If one refers to Fig. 7.10b for example, it is possible to make out the sides of the car much easier than from the co-polarised SAR image illustrated in Fig. 7.10a. This is an immense advantage which, as mentioned earlier, enables orientation estimation of the car. The disadvantage of course is that the sensor becomes larger in size since double the number of antennae now need to be accommodated.

The results of the polarimetric clutter analysis are discussed in Chapter 8, where it is shown that with the use of a fully polarimetric radar, it is possible to distinguish between asphalt surfaces which offer reduced traction when influenced by precipitation and adverse weather conditions. It is also demonstrated that driving surfaces composed of cobblestone can also be recognised based on their clutter backscatter. This is helpful since such surfaces are smoother than asphalt and hence offer much less traction. The work summarised in that chapter is essential to reduce the number of traffic accidents and is absolutely necessary if autonomous driving platforms are to function in regions of the world where snowy and icy roads are a common occurrence. The results illustrated are in an ideal position to be fed into an AI algorithm which can optimise the process and lead to even higher correct categorisation rates.

Thereby to conclude this dissertation, the take away message is that SAR is a very viable signal processing technique which would invariably make the task of assisted and automated parking easier as the advantages offered by it over traditional signal processing techniques (ultrasound and classical radar imaging) are too important to be ignored. Polarimetric radar sensors on the other hand, too offer advantages, however with the additional costs of new and larger hardware. Currently driving surface condition recognition is not a priority for cars, this will gradually change though, as highly automated vehicles are introduced to the public roads [121]. This will drive the requirement for automated vehicles to be able to recognise conditions with low traction and react to them appropriately.

Appendix A Dielectric Constant of Water

To be able to investigate the effects which occur when automotive radars are deployed in adverse weather conditions, the dielectric properties of water at microwave frequencies need to be first understood. The dielectric constant, also known as the permittivity of a material, is a term which describes how and to what degree the charge distribution within the material can be influenced or 'polarised' when an electric field is applied to it.

Although there have been numerous experiments done to measure the dielectric constant of water, it was not possible to find such results directly at the frequency (77 GHz) of interest. However, a pair of equations from literature have been found, using which it is possible to estimate the dielectric constant of water at 77 GHz for various temperatures. The Cole-Cole equations for this purpose are shown below [122],

$$\varepsilon' = \varepsilon_\infty + \frac{(\varepsilon_s - \varepsilon_\infty)\left[1 + (\omega\tau)^{1-\alpha} \cdot \sin(\frac{\alpha\pi}{2})\right]}{1 + 2(\omega\tau)^{1-\alpha} \cdot \sin(\frac{\alpha\pi}{2}) + (\omega\tau)^{2(1-\alpha)}} \tag{A.1}$$

$$\varepsilon'' = \frac{(\varepsilon_s - \varepsilon_\infty)(\omega\tau)^{1-\alpha} \cdot \cos(\frac{\alpha\pi}{2})}{1 + 2(\omega\tau)^{1-\alpha} \cdot \sin(\frac{\alpha\pi}{2}) + (\omega\tau)^{2(1-\alpha)}} \tag{A.2}$$

Equation (A.1) can be used to calculate the dielectric permittivity (real part) of the dielectric constant while (A.2) can be used to calculate the dielectric loss (imaginary part). ε_s is the static dielectric constant of water at very low frequencies, ε_∞ is the dielectric constant of water at very high frequencies, τ is the macroscopic relaxation time, and α is the relaxation time spread parameter. These parameters have been estimated through nonlinear regression analysis for various temperatures of water [122]. A detailed handling of the relaxation times for water can be found in [123] [124].

In Fig. A.1, is shown the curve obtained from (A.1) and (A.2) for water at 20°C. Also marked are a few points corresponding to frequencies of interest. The curve starts at the point ε_s below approximately 10 MHz before increasing

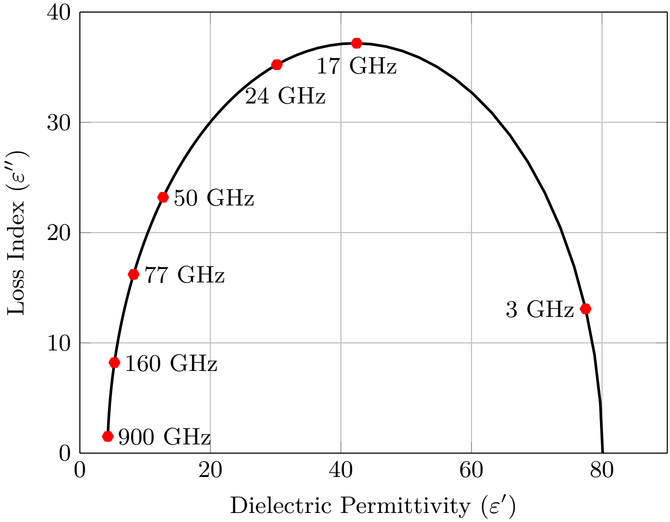

Fig. A.1: Dielectric properties of water at 20°.

sharply with frequency to reach a high point at 17 GHz. The attenuation due to water should be highest at this frequency. With ever increasing frequency, the curve decreases approaching ε_∞. The dielectric constant corresponding to 77 GHz is calculated to be, $\varepsilon_r = 8.24 - j16.21$. The calculated values from the Cole-Cole equations have been shown to agree with the measured dielectric constants at other frequencies [122].

Appendix B Measurement Control Software for the SAR Demonstrator

This chapter presents the measurement control software for the SAR demonstrator introduced in Section 6.2.2. For the measurements presented in this work, the maximum allowed sample spacing, Δx as defined by (6.13), was calculated to be 1.5 mm. In essence, this translates to getting one FMCW ramp (one range profile, or radar measurement) every 1.5 mm. This is a requirement to satisfy the Nyquist criterion, the fulfilment of which requires efficient time and resource management, so that the radar measurement data as well as the odometry data from the respective interface devices (see Fig. 6.11) can be fetched and saved for processing at a later stage. It is also of the utmost importance that the time being maintained by the microcontroller (odometry time with respect to the rotary encoder) and the measurement computer (radar time) be of the same length.

To control the measurement hardware and to ensure that no data is lost due to memory overflows and that time is efficiently utilised to maximise the number of radar measurements, the controlling software was designed using three threads, one thread was used to trigger the radar and ask it to pause when needed. The second thread's job was to fetch data from the first-in first-out (FIFO) memory structure present in the radar backend and save it to RAM in the measurement computer. The last thread was charged with interfacing of the microcontroller. These state machine implementation of these three threads is illustrated in Fig. B.1.

On the left is the radar control thread, which triggers the radar and polls a signal from the radar backend which indicates if the FIFO is more than half-full. As soon as this signal is high, the radar is paused and the second thread (the thread in the middle in Fig. B.1) starts to fetch the radar measurement data over a USB 2.0 connection. As soon as the data has been fetched, the second thread raises the *clear FIFO* flag. This is a message to the first thread that it

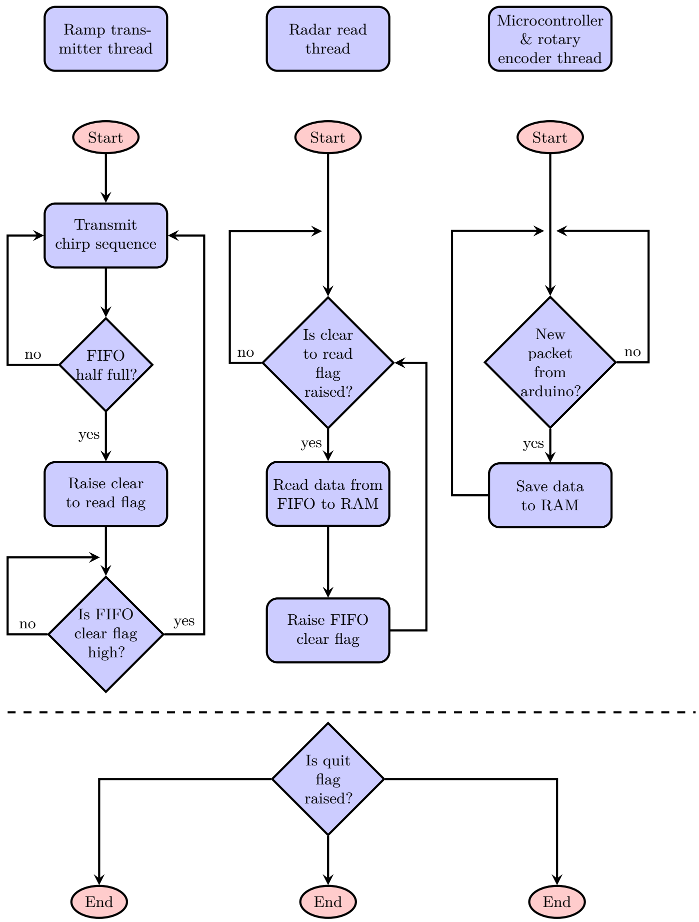

Fig. B.1: Threads flow diagram for the control software.

can trigger the radar again, while the second thread polls the *clear to read* flag. The third thread polls for new messages from the microcontroller and saves the content to RAM when a new message arrives.

The software was programmed to run for as long as a pre-defined keyboard key hit was not detected. Upon detection of the pre-defined *quit* key, a flag is raised which indicates to all three threads that they need to tidy up and terminate as soon as possible in a clean fashion without loss of any data.

Bibliography

[1] *Taxonomy and Definitions for Terms Related to On-Road Motor Vehicle Automated Driving Systems*, SAE MOBILUS Open Platform Std., Jan 2014. [Online]. Available: https://saemobilus.sae.org/content/j3016_201401

[2] A. Taeihagh and H. S. M. Lim, "Governing autonomous vehicles: emerging responses for safety, liability, privacy, cybersecurity, and industry risks," *Transport Reviews*, vol. 39, no. 1, pp. 103–128, 2019.

[3] "Waymo safety report on the road to fully self-driving," 2018. [Online]. Available: https://storage.googleapis.com/sdc-prod/v1/safety-report/Safety%20Report%202018.pdf

[4] K. Korosec, "Watch a waymo self-driving car test its sensors in a haboob," Aug 2019. [Online]. Available: https://techcrunch.com/2019/08/23/watch-a-waymo-self-driving-car-test-its-sensors-in-a-haboob/

[5] J. Fingas, "Waymo shows how its self-driving cars navigate snow," Aug 2018. [Online]. Available: https://www.engadget.com/2018/05/08/waymo-snow-navigation

[6] "The European New Car Assessment Programme." [Online]. Available: https://www.euroncap.com/en/about-euro-ncap/

[7] "Automotive lidar: Lidar for self-driving cars comes in many competing forms," Dec 2018. [Online]. Available: https://www.laserfocusworld.com/test-measurement/test-measurement/article/16555290/automotive-lidar-lidar-for-selfdriving-cars-comes-in-many-competing-forms

[8] J. Hecht, "Lasers for lidar: Fmcw lidar: An alternative for self-driving cars," May 2019. [Online].

Available: https://www.laserfocusworld.com/home/article/16556322/lasers-for-lidar-fmcw-lidar-an-alternative-for-selfdriving-cars

[9] K. Werber, J. Klappstein, J. Dickmann, and C. Waldschmidt, "Interesting areas in radar gridmaps for vehicle self-localization," in *IEEE MTT-S International Conference on Microwaves for Intelligent Mobility (ICMIM)*, May 2016, pp. 1–4.

[10] ARS540. Continental A.G. [Online]. Available: https://www.continental-automotive.com/en-gl/Passenger-Cars/Autonomous-Mobility/Enablers/Radars/Long-Range-Radar/ARS540

[11] S. Parker, *McGraw-Hill Dictionary of Scientific and Technical Terms.* McGraw-Hill Education, 2003.

[12] H. H. Meinel, "Evolving Automotive Radar - from the very beginnings into the future," in *The 8th European Conference on Antennas and Propagation (EuCAP 2014)*, April 2014, pp. 3107–3114.

[13] J. Gamba, *Radar Signal Processing for Autonomous Driving.* Springer Singapore, 2019.

[14] G. L. Charvat, *Small and Short-Range Radar Systems.* CRC Press, 2014.

[15] D. Lancaster, ""Chirp" A New Radar Technique," *Electronics World*, Jan 1965.

[16] H. Urkowitz, C. A. Hauer, and J. F. Koval, "Generalized Resolution in Radar Systems," *Proceedings of the IRE*, 1962.

[17] J. Scheer and J. Kurtz, *Coherent Radar Performance Estimation.* Artech House, 1993.

[18] A. Townley, P. Swirhun, D. Titz, A. Bisognin, F. Gianesello, R. Pilard, C. Luxey, and A. M. Niknejad, "A 94-GHz 4TX-4RX Phased-Array FMCW Radar Transceiver With Antenna-in-Package," *IEEE Journal of Solid-State Circuits*, vol. 52, no. 5, pp. 1245–1259, 2017.

[19] E. K. Smith and S. Weintraub, "The Constants in the Equation for Atmospheric Refractive Index at Radio Frequencies," *Proceedings of the IRE*, vol. 41, no. 8, pp. 1035–1037, 1953.

[20] P. E. Ciddor, "Refractive index of air: new equations for the visible and near infrared," *Appl. Opt. OSA*, vol. 35, no. 9, pp. 1566–1573, Mar 1996.

[21] U. of Illinois at Urbana-Champaign, "Locating a target," 2010. [Online]. Available: http://ww2010.atmos.uiuc.edu/(Gh)/guides/rs/rad/basics/angl.rxml

[22] G. W. Stimson, *Introduction to Airborne Radar*. Scitech Publishing Inc., 1998.

[23] V. Winkler, "Range Doppler Detection for Automotive FMCW Radars," in *2007 European Radar Conference*, Oct 2007, pp. 166–169.

[24] M. I. Skolnik, *Radar Handbook*, 3rd ed., M. I. Skolnik, Ed. McGraw-Hill Education, 2008.

[25] H.-J. Li and Y.-W. Kiang, "10 - Radar and Inverse Scattering," in *The Electrical Engineering Handbook*. Academic Press, 2005, pp. 671–690.

[26] E. Fuhs, Allen, "Radar Cross Section Lectures." [Online]. Available: https://calhoun.nps.edu/handle/10945/37502

[27] E. F. Knott, J. F. Shaeffer, and M. T. Tuley, *Radar Cross Section*, ser. Radar, Sonar; Navigation. Institution of Engineering and Technology, 2004.

[28] S. Yin. (2018, April) The Crystals That May Have Helped Vikings Navigate Northern Seas. The New York Times. [Online]. Available: https://www.nytimes.com/2018/04/06/science/vikings-navigation-sunstones.html

[29] A. Moreira et al., "A Tutorial on Synthetic Aperture Radar," *IEEE Geoscience and Remote Sensing Magazine*, vol. 1, no. 1, pp. 6–43, March 2013.

[30] S. Cloude, *Polarisation: Applications in Remote Sensing.* OUP Oxford, 2009.

[31] H. Mott, *Antennas for Radar and Communications: A Polarimetric Approach*, ser. Wiley Series in Microwave and Optical Engineering. Wiley, 1992.

[32] I. H. Woodhouse, *Introduction to Microwave Remote Sensing.* CRC Press, 2006.

[33] K. E. Oughstun and C. L. Palombini, "Fresnel Reflection and Transmission Coefficients for Complex Media," in 32^{nd} *General Assembly and Scientific Symposium of the International Union of Radio Science (URSI GASS)*, 2017, pp. 1–2.

[34] D. Brewster, *Philosophical Transactions of the Royal Society of London.* W. Bowyer and J. Nichols for Lockyer Davis, printer to the Royal Society, 1815, ch. On the laws which regulate the polarisation of light by reflexion from transparent bodies, pp. 125–159. [Online]. Available: https://books.google.ca/books?id=U-U_AAAAYAAJ&pg=PA125&redir_esc=y#v=onepage&q&f=false

[35] F. T. Ulaby, R. K. Moore, and A. K. Fung, *Microwave Remote Sensing: Active and Passive, Volume 3.* Artech House, 1981.

[36] F. Mattia, T. L. Toan, J. C. Souyris, C. D. Carolis, N. Floury, F. Posa, and N. G. Pasquariello, "The Effect of Surface Roughness on Multifrequency Polarimetric SAR Data," *IEEE Transactions on Geoscience and Remote Sensing*, vol. 35, no. 4, pp. 954–966, Jul 1997.

[37] S. R. Cloude and D. G. Corr, "A New Parameter for Soil Moisture Estimation," in *IEEE International Geoscience and Remote Sensing Symposium*, 2002.

[38] Jong-Sen Lee and Eric Pottier, *Polarimetric Radar Imaging: From Basics to Applications.* CRC Press, 2009.

[39] W.-M. Boerner. (2008) Basic Cconcepts in RADAR Polarimetry. European Space Agency (ESA). [Online]. Available: https://earth.esa.int/landtraining07/polsar_basic_concepts.pdf

[40] C. López-Martínez and E. Pottier. (2015, Jan) Polarimetric Scattering Decomposition Theorems. European Space Agency (ESA). [Online]. Available: https://earth.esa.int/documents/653194/656796/Polarimetric_Decompositions.pdf

[41] A. Love, "In Memory of Carl A. Wiley," *IEEE Antennas and Propagation Society Newsletter*, vol. 27, no. 3, pp. 17–18, June 1985.

[42] H. Wu, "Motion Compensation for Near-Range Synthetic Aperture Radar Applications," Ph.D. dissertation, Karlsruhe Institute of Technology, 2012. [Online]. Available: http://dx.doi.org/10.5445/KSP/1000029383

[43] M. Soumekh, *Synthetic Aperture Radar Signal Processing with MATLAB Algorithms*. Wiley, 1999.

[44] Jibran. (2012, March) YELLOW CAR - TOP VIEW CLIP ART. [Online]. Available: http://www.clker.com/clipart-yellow-car-top-view.html

[45] I. G. Cumming and F. H. Wong, *Digital Processing of Synthetic Aperture Radar Data*. Artech House, 2005.

[46] D. F. Paul. (1999, Feb.) Theory of synthetic aperture radar. Department of Geography, University of Zurich. [Online]. Available: http://www.geo.uzh.ch/~fpaul/sar_theory.html

[47] D. Castelletti and G. Farquharson. (2020, Jun.) Sar imagery and quality metrics. Capella Space. [Online]. Available: https://www.geospatialworld.net/article/sar-imagery-and-quality-metrics/

[48] W. G. Carrara, R. S. Goodman, and R. M. Majewski, *Spotlight Synthetic Aperture Radar: Signal Processing Algorithms*. Artech House, 1995.

[49] (2014, July) Range-Doppler. European Space Agency (ESA). [Online]. Available: http://envisat.esa.int/handbooks/asar/CNTR2-6-1-2-3.html

[50] C. Cafforio, C. Prati, and F. Rocca, "SAR Data Focusing Using Seismic Migration Techniques," *IEEE Transactions on Aerospace and Electronic Systems*, vol. 27, no. 2, pp. 194–207, March 1991.

[51] M. Z. Khan, "Investigation of Range Migration Algorithm for Automotive Synthetic Aperture Radar (SAR)," Master's thesis, Ulm University, Nov. 2015.

[52] Evan C. Zaugg and David G. Long, "Generalized Frequency Scaling and Backprojection for LFM-CW SAR Processing," *IEEE Transactions on Geoscience and Remote Sensing*, vol. 53, no. 7, pp. 3600–3614, July 2015.

[53] M. Albuquerque, P. Prats, and R. Scheiber, "Applications of Time-Domain Back-Projection SAR Processing in the Airborne Case," in *7th European Conference on Synthetic Aperture Radar*, June 2008, pp. 1–4.

[54] A. Sommer, M. P. Nguyen, and J. Ostermann, "Comparison of Omega-K and Backprojection Regarding Spatial Resolution for Squinted Spotlight SAR with Motion Errors," in *IEEE 5th Asia-Pacific Conference on Synthetic Aperture Radar (APSAR)*, Sept. 2015, pp. 143–147.

[55] A. Ribalta, "Time-Domain Reconstruction Algorithms for FMCW-SAR," *IEEE Geoscience and Remote Sensing Letters*, vol. 8, no. 3, pp. 396–400, Nov 2010.

[56] A. Yegulalp, "Fast Backprojection Algorithm for Synthetic Aperture Radar," in *Proceedings of the IEEE Radar Conference*, 1999, pp. 60–65.

[57] A. Ribalta, "High Resolution SAR Image Reconstruction: The Generalized Backprojection Algorithm," in *IEEE International Geoscience and Remote Sensing Symposium*, July 2011, pp. 363–365.

[58] R. Searcy, "Machine Learning Takes Automotive Radar Further," Aptiv, Tech. Rep., Oct. 2020. [Online]. Available: https://www.aptiv.com/docs/default-source/white-papers/2020_aptiv_whitepaper_machinelearning_radar.pdf?sfvrsn=dd3a9a3e_6

[59] A. Schwind, R. Stephan, and M. A. H. Thuringian, "Simulations and Measurements of the Bistatic Radar Cross Section of Vulnerable Road Users

between 2 GHz and 6 GHz," in *IEEE MTT-S International Conference on Microwaves for Intelligent Mobility (ICMIM)*, 2018.

[60] S. Lee, S. Kang, S. Kim, and J. Lee, "Radar Cross Section Measurement with 77 GHz Automotive FMCW Radar," in *IEEE 27th Annual International Symposium on Personal, Indoor, and Mobile Radio Communications (PIMRC)*, 2016.

[61] S. J. Myint, C. Schneider, M. Röding, G. D. Galdo, and R. S. Thomä, "Statistical Analysis and Modeling of Vehicular Radar Cross Section," in *13th European Conference on Antennas and Propagation (EuCAP)*, 2019.

[62] K. Geary, J. S. Colburn, A. Bekaryan, S. Zeng, B. Litkouhi, and M. Murad, "Automotive Radar Target Characterization from 22 to 29 GHz and 76 to 81 GHz," in *IEEE Radar Conference (RadarCon13)*, 2013.

[63] S. B. Jayapal Gowdu, A. Schwind, R. Stephan, and M. A. Hein, "Monostatic RCS Measurements of a Passenger Car Mock-up at 77 GHz Frequency in Virtual Environment," in *49th European Microwave Conference (EuMC)*, 2019.

[64] H. Iqbal, F. Bögelsack, and C. Waldschmidt, "Polarimetric RCS Analysis of Traffic Objects," in *EURAD*, 2017, pp. 49–52.

[65] P. Hügler, M. Geiger, and C. Waldschmidt, "RCS Measurements of a Human Hand for Radar-Based Gesture Recognition at E-band," in *2016 German Microwave Conference (GeMiC)*, March 2016, pp. 259–262.

[66] K. Werber, M. Barjenbruch, J. Klappstein, J. Dickmann, and C. Waldschmidt, "How do Traffic Signs look like in Radar?" in *44th European Microwave Conference*, Oct. 2014, pp. 135–138.

[67] P. Pouliguen and L. Desclos, "A Physical Optics Approach to Near Field RCS Computations," *Annals of Telecommunications*, vol. 51, no. 5, pp. 219–226, 1996.

[68] R. Deban, H. Boutayeb, J. Conan, and K. Wu, "Numerical and Experimental Analysis of Metallic Plate Near-Field RCS at Oblique Incidence

and Applications to Radar Systems," in *Loughborough Antennas Propagation Conference*, Nov. 2009, pp. 441–444.

[69] C. Fang, Q. Liu, F. Ding, X. Zhao, and J. Xiao, "The Near-field Measurement and Near-Far Field Transformation of Microwave Scattering of a Plate at Different Distances," in *Proceedings of the 3rd Asia-Pacific Conference on Antennas and Propagation*, 2014.

[70] D. Giuli, "Polarization Diversity in Radars," *Proceedings of the IEEE*, vol. 74, no. 2, pp. 245–269, Feb. 1986.

[71] PRE-SAFE®: Anticipatory occupant protection system reduces the forces exerted on the occupants during accidents by up 40 percent. Daimler. [Online]. Available: https://media.daimler.com/marsMediaSite/ko/en/9361558

[72] M. Andres, K. Ishak, W. Menzel, and H.-L. Bloecher, "Extraction of Micro-Doppler Signatures using Automotive Radar Sensors," *Frequenz Journal of RF-Engineering and Telecommunications*, vol. 66, pp. 371–377, December 2012.

[73] K. Werber, M. Rapp, J. Klappstein, M. Hahn, J. Dickmann, K. Dietmayer, and C. Waldschmidt, "Automotive Radar Gridmap Representations," in *IEEE MTT-S International Conference on Microwaves for Intelligent Mobility (ICMIM)*, 2015, pp. 1–4.

[74] H. Wu and T. Zwick, "Automotive SAR for Parking Lot Detection," in *German Microwave Conference*, March 2009, pp. 1–8.

[75] H. Wu, L. Zwirello, X. Li, L. Reichardt, and T. Zwick, "Motion Compensation with One-axis Gyroscope and Two-axis Accelerometer for Automotive SAR," in *German Microwave Conference (GeMIC)*, March 2011, pp. 1–4.

[76] R. Feger, A. Haderer, and A. Stelzer, "Experimental Verification of a 77-GHz Synthetic Aperture Radar System for Automotive Applications," in *IEEE MTT-S International Conference on Microwaves for Intelligent Mobility (ICMIM)*, Mar 2017, pp. 111–114.

[77] T. Gisder, F. Harrer, and E. Biebl, "Application Of A Stream-Based SAR-Backprojection Approach For Automotive Environment Perception," in *19th International Radar Symposium (IRS)*, June 2018, pp. 1–10.

[78] F. Harrer, F. Pfeiffer, and A. L. et al., "Synthetic Aperture Radar Algorithm for a Global Amplitude Map," in *14th Workshop on Positioning, Navigation and Communications (WPNC)*, Oct. 2017, pp. 1–6.

[79] A. Laribi, M. Hahn, J. Dickmann, and C. Waldschmidt, "Performance Investigation of Automotive SAR Imaging," in *IEEE MTT-S International Conference on Microwaves for Intelligent Mobility (ICMIM)*, 2018, pp. 1–4.

[80] T. Gisder, M. Meinecke, and E. Biebl, "Synthetic Aperture Radar Towards Automotive Applications," in *20th International Radar Symposium (IRS)*, June 2019, pp. 1–10.

[81] H. Iqbal, B. Sajjad, M. Mueller, and C. Waldschmidt, "SAR Imaging in an Automotive Scenario," in *IEEE 15th MMS*, 2015, pp. 1–4.

[82] H. Iqbal, M. Schartel, F. Roos, J. Urban, and C. Waldschmidt, "Implementation of a SAR Demonstrator for Automotive Imaging," in *18th Mediterranean Microwave Symposium (MMS)*, Oct. 2018, pp. 240–243.

[83] D. Duncan and D. Long. (2003, April) Motion compensation of Synthetic Aperture Radar. Microwave Earth Remote Sensing Laboratory, Brigbam Young University. [Online]. Available: https://digitalcommons.usu.edu/cgi/viewcontent.cgi?article=1237&context=spacegrant

[84] E. Favey, A. Somieski, C. Hollenstein, M. Ammann, and C. Fenger, "u-blox' Dead Reckoning for Automotive Applications: Intelligent solutions for modern urban navigation," u-blox, Tech. Rep., 2010. [Online]. Available: https://www.u-blox.com/sites/default/files/products/documents/u-blox-ADR_WhitePaper_%28UBX-adr%29.pdf

[85] D. L. Donoho, "Compressed Sensing," *IEEE Transactions on Information Theory*, vol. 52, no. 4, pp. 1289–1306, April 2006.

[86] J. Ender, "A Brief Review of Compressive Sensing Applied to Radar," in *14th International Radar Symposium (IRS)*, June 2013, pp. 3–16.

[87] V. M. Patel, G. R. Easley, D. M. Healy, and R. Chellappa, "Compressed Sensing for Synthetic Aperture Radar Imaging," in *16th IEEE International Conference on Image Processing (ICIP)*, Nov 2009, pp. 2141–2144.

[88] F. Marvasti, A. Amini, F. Haddadi, M. Soltanolkotabi, B. H. Khalaj, A. Aldroubi, S. Holm, S. Sanei, and J. Chambers, "A Unified Approach to Sparse Signal Processing," 2009. [Online]. Available: https://arxiv.org/abs/0902.1853

[89] F. Roos, P. Hügler, C. Knill, N. Appenrodt, J. Dickmann, and C. Waldschmidt, "Data Rate Reduction for Chirp-Sequence Based Automotive Radars using Compressed Sensing," in *11th German Microwave Conference (GeMiC)*, March 2018, pp. 347–350.

[90] N. Carey. (2005, May) Establishing pedestrian walking speeds. Portland State Univeristy. [Online]. Available: https://www.westernite.org/datacollectionfund/2005/psu_ped_summary.pdf

[91] M. C. Dobson and F. T. Ulaby and L. E. Pierce and T. L. Sharik and K. M. Bergen and J. Kellndorfer and J. R. Kendra and E. Li and Y. C. Lin and A. Nashashibi and K. Sarabandi and P. Siqueira, "Estimation of Forest Biophysical Characteristics in Northern Michigan with SIR-C/X-SAR," *IEEE Transactions on Geoscience and Remote Sensing*, vol. 33, no. 4, pp. 877–895, July 1995.

[92] Kathleen M. Bergen and M. Craig Dobson and Leland E. Pierce and Fawwaz T. Ulaby, "Characterizing Carbon in a Northern Forest by Using SIR-C/X-SAR Imagery," *Remote Sensing of Environment*, vol. 63, no. 1, pp. 24–39, January 1998.

[93] S. R. Cloude, *Direct and Inverse Methods in Radar Polarimetry*. Springer, Dordrecht, 1992, ch. Uniqueness of Target Decomposition Theorems in Radar Polarimetry, pp. 267–296.

[94] R. P. Feynman, *The Feynman Lectures on Physics, Volume II*. Addison-Wesley Pub. Co., 1965, vol. 2.

[95] (2015, Nov.) Radar polarimetry. Canadian Centre for Remote Sensing. [Online]. Available: https://www.nrcan.gc.ca/maps-tools-publications/satellite-imagery-air-photos/remote-sensing-tutorials/microwave-remote-sensing/radar-polarimetry/9275

[96] J. Yang, Y. Yamaguchi, J.-S. Lee, R. Touzi, and W.-M. Boerner, "Applications of Polarimetric SAR," *Journal of Sensors*, July 2015.

[97] H. Iqbal, C. Knill, M. Z. Khan, T. Chaloun, and C. Waldschmidt, "Polarimetric SAR for Automotive Applications," in *15th European Radar Conference (EuRAD)*, 2018, pp. 30–33.

[98] (2019) Interpreting imaging radar. Humboldt State University. [Online]. Available: http://gis.humboldt.edu/OLM/Courses/GSP_216_Online/lesson7-2/interpreting-radar.html

[99] A. Stroescu, M. Cherniakov, and M. Gashinova, "Classification of High Resolution Automotive Radar Imagery for Autonomous Driving Based on Deep Neural Networks," in *20th International Radar Symposium (IRS)*, June 2019, pp. 1–10.

[100] A. Stroescu, L. Daniel, and M. Gashinova, "Combined Object Detection and Tracking on High Resolution Radar Imagery for Autonomous Driving Using Deep Neural Networks and Particle Filters," in *IEEE Radar Conference (RadarConf20)*, 2020.

[101] A. Stroescu, L. Daniel, D. Phippen, M. Cherniakov, and M. Gashinova, "Object Detection on Radar Imagery for Autonomous Driving Using Deep Neural Networks," in *2020 17th European Radar Conference (EuRAD)*, Jan. 2021, pp. 120–123.

[102] A. Elfes, "Using Occupancy Grids for Mobile Robot Perception and Navigation," *Computer*, vol. 22, no. 6, pp. 46–57, June 1989.

[103] D. Pagac, E. M. Nebot, and H. Durrant-Whyte, "An Evidential Approach to Map-Building for Autonomous Vehicles," *IEEE Transactions on Robotics and Automation*, vol. 14, no. 4, pp. 623–629, Aug 1998.

[104] (2019) History Of Radar. Encyclopedia Britannica. [Online]. Available: https://www.britannica.com/technology/radar/History-of-radar#targetText=Early%20experiments,Hertz%20during%20the%20late%201880s.

[105] H. Bendel. (2019) History of Radar. Fraunhofer-Gesellschaft. [Online]. Available: https://www.blackvalue.de/en/radarbasics/radar-history.html

[106] SCR-270 Early Warning Radar at Pearl Harbor. World War 2 Headquarters. [Online]. Available: http://worldwar2headquarters.com/HTML/PearlHarbor/PearlHarborAirFields/radar.html

[107] (2017) Snow and Ice. U.S. Department of Transportation Federal Highway Administration. [Online]. Available: https://ops.fhwa.dot.gov/weather/weather_events/snow_ice.htm

[108] "Verkehrsunfälle," Statistisches Bundesamt (DESTATIS), Tech. Rep. Fachserie 8 Reihe 7, July 2019. [Online]. Available: https://www.destatis.de/DE/Themen/Gesellschaft-Umwelt/Verkehrsunfaelle/Publikationen/Downloads-Verkehrsunfaelle/verkehrsunfaelle-jahr-2080700187004.pdf?__blob=publicationFile

[109] Haykin, S. and Stehwien, W. and Deng, C. and Weber, P. and Mann, R., "Classification of Radar Clutter in an Air Traffic Control Environment," *Proceedings of the IEEE*, vol. 79, no. 6, pp. 742–772, Jun. 1991.

[110] D. Richardson, *F-16 Fighting Falcon*, ser. Modern Fighting Aircraft. Arco Publishing Company, 1983, no. 2.

[111] Y.-Z. Ma, C. Cui, B.-S. Kim, J.-M. Joo, S. H. Jeon, and S. Nam, "Road Clutter Spectrum of BSD FMCW Automotive Radar," in *European Radar Conference (EuRAD)*, Sept. 2015, pp. 109–112.

[112] K. Sarabandi, E. S. Li, and A. Nashashibi, "Modeling and Measurements of Scattering from Road Surfaces at Millimeter-Wave Frequencies," *IEEE Transactions on Antennas and Propagation*, vol. 45, no. 11, pp. 1679–1688, Nov 1997.

[113] V. Viikari, T. Varpula, and M. Kantanen, "Automotive Radar Technology for Detecting Road Conditions. Backscattering Properties of Dry, Wet, and Icy Asphalt," in *European Radar Conference (EuRAD)*, Oct. 2008, pp. 276–279.

[114] V. V. Viikari, T. Varpula, and M. Kantanen, "Road-Condition Recognition Using 24-GHz Automotive Radar," *IEEE Transactions on Intelligent Transportation Systems*, vol. 10, no. 4, pp. 639–648, Dec 2009.

[115] J. Häkli, J. Säily, P. Koivisto, I. Huhtinen, T. Dufva, A. Rautiainen, H. Toivanen, and K. Nummila, "Road Surface Condition Detection Using 24 GHz Automotive Radar Technology," in *14th International Radar Symposium (IRS)*, vol. 2, June 2013, pp. 702–707.

[116] K. Ramasubramanian, K. Ramaiah, and A. Aginskiy. (2017) Moving from legacy 24 GHz to state-of-the-art 77 GHz radar. open access. Texas Instruments. Texas Instruments, Post Office Box 655303, Dallas, Texas 75265. [Online]. Available: http://www.ti.com/lit/wp/spry312/spry312.pdf

[117] *Harmonised European Standard Short Range Devices; Transport and Traffic Telematics (TTT); Radar equipment operating in the 76 GHz to 77 GHz range; Harmonised Standard covering the essential requirements of article 3.2 of Directive 2014/53/EU; Part 1: Ground based vehicular radar*, European Telecommunications Standards Institute (ETSI) Std. [Online]. Available: https://www.etsi.org/deliver/etsi_en/301000_301099/30109101/02.01.01_30/en_30109101v020101v.pdf

[118] D. Tse and P. Viswanath, *Fundamentals of Wireless Communication*. Cambridge University Press, 2005.

[119] D. D. Dimitrijevic, M. M. Petrovic, M. G. Hrasovec, and B. V. Damnjanovic, "Implementation of radar cfar-based target detection algorithm in a real-time multiprocessor environment," in *5th International Conference on Telecommunications in Modern Satellite, Cable and Broadcasting Service. TELSIKS. Proceedings of Papers (Cat. No.01EX517)*, vol. 2, Sept. 2001, pp. 749–752.

[120] G.Minkler and J.Minkler, *CFAR: The Principles of Automatic Radar Detection in Clutter*. Magellan Book Co, April 1990.

[121] J. Ewing, "How Germany Hopes to Get the Edge in Driverless Technology," July 2021. [Online]. Available: https://www.nytimes.com/2021/07/14/business/germany-autonomous-driving-new-law.html

[122] J. B. Hasted, *Aqueous Dielectrics*, ser. Studies in Chemical Physics. Chapman and Hall (Distributed in the U.S.A. by Halsted Press, a division of J. Wiley & Sons, New York), 1973.

[123] J. Hasted, S. K. Husain, F. A. M. Frescura, and J. R. Birch, "The Temperature Variation of the Near Millimetre Wavelength Optical Constants of Water," *Infrared Physics*, vol. 27, no. 1, pp. 11–15, 1987.

[124] V. I. Arkhipov and N. Agmon, "Relation between Macroscopic and Microscopic Dielectric Relaxation Times in Water Dynamics," *Israel Journal of Chemistry*, vol. 43, pp. 363–371, 2003.

Herausgeber:
Prof. Dr.-Ing. Christian Waldschmidt

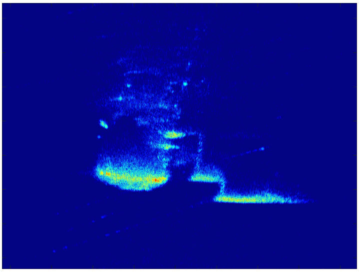

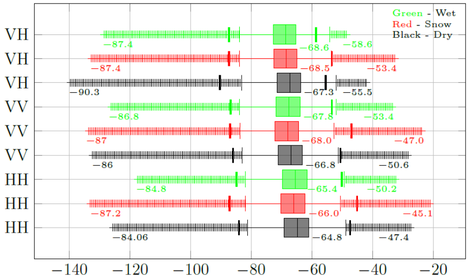

The objective of the work contained in this dissertation is to investigate and present algorithms which can be used to derive more information out of an automotive radar than is possible with current techniques. The synthetic aperture radar (SAR) has been used for reconnaissance and remote sensing for more than half a century and is now finding application in the automotive scenario. The motion of the ego-vehicle can be used to accumulate a large number of radar measurements of the surroundings perpendicular to the egotrajectory. These measurements can then be integrated together to form a high-resolution radar map of the surroundings.

The use of polarimetry capable radar sensors can enable a multitude of solutions which would make automated driving easier: self-localisation using polarimetric radar cross-section measurements (RCS), polarimetric SAR to win more information of ubiquitous traffic objects and clutter analysis to recognise driving surfaces and loss of traction in adverse weather conditions.

ISBN: 978-3-948303-36-5 ISBN: 978-3-948303-37-2 (E-Book)